

UNIVERSITÀ DEGLI STUDI DI MILANO

Facoltà di scienze matematiche, fisiche e naturali

CORSO DI LAUREA IN FISICA

Anno accademico 2001-2002

Propagazione di fluttuazioni
termiche nei Reference Load
dello strumento PLANCK/LFI

Tesi di laurea di

MAURIZIO TOMASI

Matricola n. 562383

CODICE PACS 95.85.Bh

Relatore interno: MARCO BERSANELLI

Relatore esterno: ANIELLO MENNELLA

UNIVERSITÀ DEGLI STUDI DI MILANO

Facoltà di scienze matematiche, fisiche e naturali

CORSO DI LAUREA IN FISICA

Anno accademico 2001-2002

Propagation of Thermal
Fluctuations in the Reference
Loads of the PLANCK/LFI
Instrument

Tesi di laurea di

MAURIZIO TOMASI

Matricola n. 562383

CODICE PACS 95.85.Bh

Relatore interno: MARCO BERSANELLI

Relatore esterno: ANIELLO MENNELLA

Typeset with L^AT_EX.

This thesis is available in electronic format (Adobe Portable Document Format, PDF) at http://www.geocities.com/zio_tom78/.

Contents

1	The Cosmic Microwave Background	1
1.1	Hot Big Bang Cosmology	1
1.1.1	Expansion of the Universe	2
1.1.2	The CMB Frequency Spectrum	3
1.1.3	CMB Anisotropies	5
1.1.4	The Inflationary Model	7
1.2	Importance of the CMB for Cosmology	8
1.3	Observation of the CMB	9
1.4	Overview of the Planck Mission	11
2	The Low Frequency Instrument	17
2.1	Overview	17
2.2	Radiometers	18
2.3	Reference Loads	21
2.4	The Planck 20 K and 4 K Coolers	22
2.5	Sources and Control of Systematic Errors	25
2.6	General Thermal Stability Requirements	26
2.7	Requirements on Reference Load Thermal Stability	26
3	The Heat Equation and its Application to LFI	29
3.1	Derivation of the Equation	29
3.2	General Properties of the Equation	30
3.2.1	Canonical Solution	31
3.2.2	Boundary Conditions and Heat Sources	33
3.2.3	Damping of Periodic Fluctuations	35
3.3	Analytical Solutions using the Eigenfunction Expansion (EE) Method	37
3.3.1	The One-Dimensional Solution	38
3.3.2	The Two-Dimensional Solution	42
3.4	Numerical Solutions	48
3.4.1	The Finite Difference Method	48
3.4.2	Matrix Formulation of the Finite Difference Formulae	49
3.4.3	Implementation of a Simple FDM Solver	50

4	Analysis of Heat Conduction: Propagation of Thermal Fluctuations	51
4.1	Propagation of a Boundary Temperature Step Change	51
4.1.1	The One-Dimensional Solution	52
4.1.2	The Two-Dimensional Solution	52
4.1.3	Dependence of the Temperature Distribution from Physical Parameters	54
4.2	Propagation of Boundary Temperature Periodic Fluctuations	55
4.2.1	The One-Dimensional Solution	55
4.2.2	The Two-Dimensional Solution	57
4.2.3	Dependence of the Solution on Physical Parameters .	58
4.3	Propagation of Boundary Heat Flux Periodic Fluctuations . .	59
4.3.1	The Analytical Solution	59
4.4	Combination of Temperature Fluctuations and Heat Flux Fluctuations	60
5	Results and Discussion	62
5.1	Propagation of a Boundary Temperature Step Change	62
5.1.1	One-Dimensional Analysis	62
5.1.2	Two-Dimensional Analysis	65
5.1.3	Sensitivity of the Temperature Distribution from Physical Parameters	67
5.2	Propagation of Boundary Temperature Periodic Fluctuations	69
5.2.1	The One-Dimensional Model	69
5.2.2	The Two-Dimensional Model	73
5.2.3	Dependence of the Solution on Physical Parameters .	73
5.2.4	Example of the application of 1-D models to a temperature fluctuation with complex shape	77
5.3	Propagation of Boundary Heat Flux Periodic Fluctuations . .	84
5.4	Combined Effect of Temperature and Heat Flux Periodic Fluctuations	87
6	Other Applications of the EE Method	88
6.1	Damping Improvements using Thermal Breaks	88
6.1.1	Steady-state case	88
6.1.2	Temperature Fluctuation in the Thermal Mass	90
6.1.3	Possible Choices for the Insulator Material	90
6.2	Laboratory Measurements of Thermal Constants	91
6.2.1	The Apparatus	92
6.2.2	Experimental Details	93
6.2.3	Data Analysis of a Set of Measures	93
6.2.4	An Analytical Model	94

7	Conclusions and Future Work	102
7.1	Conclusions	102
7.2	Other Possible Cases of Study	103
7.2.1	Dependence of Diffusivity on the Temperature	103
7.2.2	Presence of a Contact Resistance	105
7.3	Numerical 3-D Model with SINDA	106
A	Completeness of the cosine set	108
B	Solution of the Heat Equation Using Green's Functions	111
C	Evolution Operators and Semigroups	114
C.1	The Problem	114
C.2	Contraction Semigroups	115
C.3	Well-posed Problems	118
C.3.1	The Definition	118
C.3.2	Well-posedness of the Heat Equation	119
C.4	Boundary Conditions	120
C.4.1	Exponential Operators	120
C.4.2	The Diffusion Operator	123
C.5	The Inhomogeneous Case	123
D	Scripts used with the Heat Program	125
E	Numerical Meshes with FElt	131
E.1	The 2-D Model	131
	Mathematical Symbols	134
	Acronyms used in the text	135
	Bibliography	136

Summary

PLANCK is a European Space Agency (ESA) mission to measure the Cosmic Microwave Background (CMB) anisotropies. These measures will provide a confirmation for the current evolutive models of the Universe and allow to better understand the very first phases of its expansion. According to the Standard Model, the Universe was originated from a singularity and formed at first a very hot and dense plasma ($T \sim 10^{15}$ K, $\rho \sim 10^{25}$ g/cm³ after 10^{-8} s) where radiation and matter were coupled by Thomson scattering. After $\sim 3 \times 10^5$ years, the expansion of the Universe cooled off the plasma to 3000 K, allowing for the synthesis of neutral atoms and letting the radiation propagate freely. Today this radiation is detectable as a faint signal ($T \sim 3$ K) with anisotropies $\Delta T/T \sim 10^{-5}$ on angular scales $\gtrsim 0.1^\circ$. These anisotropies were generated in the first 3×10^5 years by gravitational fluctuations and acoustic oscillations in the primordial plasma. The first measurement of these anisotropies was made by COBE in 1992, with an angular resolution of $\sim 7^\circ$ and a sensitivity of $\sim 35 \mu\text{K}$. These measures were confirmed by many other experiments, both ground-based and balloon-based.

PLANCK will be launched in 2007 and will measure the anisotropies on the whole sky with a wide frequency coverage (30, \div 887 GHz), high sensitivity ($\Delta T/T \sim 10^{-6}$) and unprecedented angular resolution ($5' \div 33'$). Within these performances, it is required to accurately control systematic errors and reduce them down to $3 \mu\text{K}$.

On the PLANCK spacecraft two different instruments will be mounted: the High Frequency Instrument (HFI) and the Low Frequency Instrument (LFI), which will observe the sky through a common telescope. HFI is a 48-bolometers array cooled to 0.1 K which measures the sky temperature at six frequencies in the band 100 \div 887 GHz. LFI is an array of 48 pseudo-correlation differential receivers based on HEMT (High Electron Mobility Transistor) technology cooled to ~ 20 K. The instrument measures the sky signal at four frequencies in the range 30 \div 100 GHz. Each radiometer measures the difference between the sky temperature (~ 2.73 K) and the temperature of a internal high-emissivity reference load (RL), cooled to ~ 4 K by means of a thermal contact with the HFI external shield. The frequency of the antenna measuring the reference signal drives the design of the RLs

both in its size and shape: these are chosen in order to optimize the radiative coupling between the two bodies.

A possible source of systematic effects is given by thermal instabilities in the RLs. Their temperature fluctuations must be below the $\sim 5\mu\text{K}$ level. This thesis was done at the “Istituto di Astrofisica Spaziale e Fisica cosmica” (IASF) of the CNR (Milano, Italy) and presents a study about the propagation of temperature fluctuations through the RL by means of heat conduction (radiative heat fluxes are considered to be boundary conditions).

I have developed a 1-D model and a 2-D model for the RL which is as representative as possible of its effective shape, and within these approximations I analytically solved the heat conduction equation. I verified the results with numerical models, and the agreement is very good. Then, I developed a preliminary 3-D numerical model using the thermal analysis software SINDA; this model implements the full geometry of the RL.

I studied four different problems about the propagation of thermal fluctuations:

1. I derived an estimate for the characteristic time τ which describes the propagation speed of thermal fluctuations. To achieve this, I considered an instantaneous temperature variation at one side of the RL and studied its propagation through the body.
2. I studied the propagation of a periodic temperature fluctuation coming from the HFI external shield. My results show that the RL damp high-frequency fluctuations quite well: more than 50% if $\nu \gtrsim 0.05$ Hz. This “critical frequency” is an important parameter when estimating the impact of systematic errors on the measures.
3. Then, I studied the thermal fluctuations induced on the RL by a radiative heat flux coming from the LFI radiometers. It can be shown that the amplitude of these fluctuations (~ 10 nK) is ~ 100 times smaller than the previous case.
4. I studied the damping of temperature fluctuations when a thermal insulator between the RL and the HFI shield is present. This leads to some requirements on the thermal properties of the insulating material.

I also applied my models to the analysis of laboratory measures on the RL material. This work aims to characterize the thermal diffusivity value D at 4 K. These experiments were done at the IASF-CNR in Bologna during July 2002 by the team led by Dr. Luca Valenziano.

Further developments of this work include: (i) extensive study of a complete 3-D numerical model where conductive and radiative effects are coupled, (ii) integration of the thermal model results in the electromagnetic model of the RL, currently developed at the IASF in Bologna, (iii) calibration of analytical and numerical models with further experimental measures,

(iv) estimates on the impact of RL thermal fluctuations on systematic errors in the measured signal, and analysis of the impact on the science.

CHAPTER 1

The Cosmic Microwave Background

§ 1.1 Hot Big Bang Cosmology

The *Hot Big Bang* theory is considered the most reliable model of the Universe evolution. The theory was originally introduced by Gamow (1946) and his collaborators Halper and Hermann in order to explain the observed relative abundances of nuclei in the Universe.

After Gamow's article the model was further refined to account for new discoveries and measures, and today it is strongly consistent with cosmological observations. The basic features of the standard scenario are as follows:

1. About 1.5×10^{10} years ago the Universe began to expand into a hot and dense plasma ($T \sim 10^2 \text{ GeV} \sim 10^{15} \text{ K}$ after about 10^{-8} s) which cooled down as a consequence of the expansion itself. This event is called the *Big Bang*.
2. Nucleosynthesis started at a cosmic time $\sim 1 \text{ s}$, when the mean kinetic energy (with $T \sim 10^{11} \text{ K}$) was sufficiently low to produce ^2H , although at a very low rate. After $\sim 200 \text{ s}$ the temperature was less than 10^9 K , allowing for the formation of ^3He and ^4He from ^2H . The predictions of this model are remarkably consistent with the observed abundances of hydrogen ($\sim 76\%$) and helium ($\sim 24\%$) and other light nuclei.
3. In the first 3×10^5 years after the Big Bang, thermodynamic equilibrium between matter and radiation was maintained by Thomson scattering between free electrons and photons; after this period the temperature was low enough ($\sim 3000 \text{ K}$) to allow for the combination of electrons and protons into neutral hydrogen: the reduced density of free electrons made the matter transparent to radiation, which started to propagate freely.
4. The propagation of this radiation still continues, but the expansion of the universe has cooled it off still maintaining its original black-

body spectrum. At the present time this radiation is in the microwave range ($T \sim 3\text{ K}$, $\lambda_{\text{max}} \sim 2\text{ mm}$), and it is known as Cosmic Microwave Background (CMB).

1.1.1. Expansion of the Universe. The evolution of the Universe has been driven by a cosmic expansion which is still acting at present times. This phenomenon is in line with the findings of Aleksander A. Friedmann in 1922, when he calculated a non-stationary homogeneous solution of the field equations of General Relativity proposed by Alfred Einstein in 1917 (see Weinberg 1977).

The key element of the model is the “space dilation” effect. Given two points A and B in the Universe, their distance r changes from time t_0 to time t according to

$$r(t) = r_0 \frac{R(t)}{R(t_0)}, \quad (1.1.1)$$

where r_0 is the distance between A and B at time t_0 and $R(t)$ (the “scale factor”) is given by the Friedmann equations. The exact shape of $R(t)$ depends on the actual density of the Universe and the so-called *critical density* ρ_{crit} :

1. If $\rho > \rho_{\text{crit}}$ then the Universe will begin to collapse after a time $t_{\text{crit}} > t_{\text{now}}$, because of the gravitational force: $R(t)$ is a function with a maximum in t_{crit} . In this case the universe is said to be “closed”: the space has a spherical curvature and the geometry is non-Euclidean.
2. If $\rho < \rho_{\text{crit}}$ the expansion is slowed down by the gravitational force but never interrupted: $R(t)$ is a monotonically increasing function (“open universe”). In this case the universe is said to be “open”: the space has an hyperbolic curvature and the geometry is non-Euclidean.
3. If $\rho = \rho_{\text{crit}}$ the expansion will not be interrupted by the gravitational force, but $R'(t) \rightarrow 0$ asymptotically (“flat universe”). In this case the universe is said to be “flat” and the postulates of the Euclidean geometry are valid.

A key parameter is therefore the ratio between the actual density and the critical density, defined by:

$$\Omega_0 = \frac{\rho}{\rho_{\text{crit}}}. \quad (1.1.2)$$

Since the Universe is still expanding it can be deduced that $R(t)$ is a monotonic increasing function at least for $0 < t < t_{\text{now}}$. The expansion causes a decrease in the frequency of traveling wave signals which is quantitatively described by the redshift parameter z :

$$z = \frac{\Delta\nu_{\text{obs}}}{\nu_{\text{emit}}} = \frac{\nu_{\text{obs}} - \nu_{\text{emit}}}{\nu_{\text{emit}}} = \frac{R(t_{\text{obs}})}{R(t_{\text{emit}})}, \quad (1.1.3)$$

where ν_{obs} is the observed frequency at time t_{obs} , and ν_{emit} is the frequency at time of emission t_{emit} . From the fact that $R(t)$ is bijective (because it is monotonically increasing), then z is bijective too and can be used instead of time t : for example, $z \sim 1000$ indicates the decoupling epoch ($t = 3 \times 10^5$ y)

The first experimental evidence of the expansion of the Universe was deduced by Edwin Hubble in 1929 from the analysis of the absorption line spectra of distant galaxies. Hubble discovered that galaxies farther than¹ $\sim 10^5$ Kpc are moving away from our galaxy with speed v proportional to their distance r :

$$v = H r, \quad (1.1.4)$$

where H is a proportionality constant; according to the hypotheses of the Standard Model, H must be a time-dependent quantity, since from $v = dr/dt$ follows that

$$H(t) = \frac{1}{R(t)} \frac{dR}{dt}(t). \quad (1.1.5)$$

The value of H at t_{now} is called the *Hubble constant*:

$$H_0 := H(t_{\text{now}}) \sim 50 \div 100 \text{ Km/s/Mpc}. \quad (1.1.6)$$

The importance of the Hubble relation in deducing the expansion of the Universe comes from the Cosmological Principle (see Rowan-Robinson 1996): the universe as seen by fundamental observers is homogeneous and isotropic. If the Universe is homogeneous and the Hubble law is valid, then any observer will see the other galaxies going away from him: this clearly supports the view of an expanding universe.

1.1.2. The CMB Frequency Spectrum. The expansion of the Universe produces a decrease in its temperature. If we suppose that immediately after the Big Bang radiation energy was greater than the matter rest energy (the so-called “radiation-dominated era”): since the energy of a single photon is $\propto 1/\lambda \propto 1/R(t)$, the energy density ρ_R was

$$\rho_R = \frac{\text{energy}}{\text{volume}} \propto \frac{1/R(t)}{1/R^3(t)} = \frac{1}{R^4(t)}, \quad (1.1.7)$$

and thus it decreased with increasing times. By using the energy density formula for a blackbody $u(T) = \sigma T^4$ ($\sigma \approx 5.67 \times 10^{-5}$ erg/s/cm²/K⁴ is the Stefan-Boltzmann constant) then from the Friedmann equations the temperature is

$$T_{[\text{K}]} \approx \frac{1.5 \times 10^{10}}{t_{[\text{s}]}^{1/2}} \propto t^{-1/2} \quad (1.1.8)$$

in a radiation-dominated era.

¹Nearer galaxies do not obey the Hubble relation because of local gravitational effects.

Because of this cooling, about 3×10^5 y ($z \sim 1000$) after the Big Bang the plasma temperature reached ~ 3000 K and the mean kinetic energy became low enough (~ 30 eV) to allow electrons to combine with protons into neutral hydrogen and other light elements (^3He , ^4He and ^7Li). The Thomson scattering between photons and free electrons was the most important process which maintained the equilibrium between matter and radiation: at $z < 1000$ this process was no longer efficient and matter became transparent to radiation which was free to propagate. This crucial event is called the *last scattering epoch* (or “decoupling epoch”).

Today this primordial radiation is at a temperature of ~ 3 K, with a density of ~ 400 phot/cm³; it is called Cosmic Microwave Background (CMB) because the maximum in its spectrum is at 0.29 cm wavelength (~ 100 GHz). According to the Hot Big Bang Model, at the decoupling epoch the Cosmic Microwave Background (CMB) had a planckian blackbody spectrum:

$$R_T(\lambda) d\lambda = \frac{2\pi hc^2}{\lambda^5} \frac{d\lambda}{\exp(hc/\lambda KT) - 1}, \text{ with } [R_T(\lambda) d\lambda] = \text{erg/s/cm}^2, \quad (1.1.9)$$

where the *spectral radiance* R_T is the power emitted from a unit surface in the wavelength range $[\lambda, \lambda + d\lambda]$. The blackbody spectrum in the primordial plasma is maintained by three fundamental processes which were particularly efficient at high redshift:

1. Compton effect: $\gamma + e^- \rightarrow \gamma + e^-$.
2. Radiative Compton effect: $\gamma + e^- \rightarrow \gamma + 2e^-$.
3. Thermal bremsstrahlung: $Z^+ + e^- \rightarrow Z^+ + e^- + \gamma$, where Z^+ is a nucleus with Z protons.

The combination of these processes forced the spectrum to be planckian at $z = 10^6 \div 10^7$; before this era, any energy released was not able to force permanent changes in the spectrum: it is therefore not possible to extract informations about the older epochs of the Universe by studying the CMB.

The expansion of the Universe after $z = 10^6$ has not modified the shape of the CMB spectrum. In fact, in the hypothesis of the Universe expanding adiabatically, we have that $P_1 V_1^\gamma = P_2 V_2^\gamma$ where $\gamma = 4/3$ (photon gas), and

$$T \propto V^{1-\gamma} = \frac{1}{V^{1/3}} \propto \frac{1}{R(t)} \propto \frac{1}{1+z}. \quad (1.1.10)$$

Because of the redshift, the wavelength scales as $1+z$, so λT is a constant value during the expansion. Since in equation (1.1.9) the shape of the curve is given by

$$\exp \frac{h\nu}{KT} = \exp \frac{hc}{K\lambda T}, \quad (1.1.11)$$

then the spectrum shape has not changed with time and it is still planckian. The only effect of the expansion is a wavelength-shift of the spectrum due to the presence of the $\lambda^{-5} \propto (1+z)^{-5}$ term in equation (1.1.9).

1.1.3. CMB Anisotropies. After the Gamow’s article (see Hu et al. 1997; Scott et al. 1995, for a review) it was proposed that this highly isotropic signal should contain small anisotropies (today known to have an amplitude $\Delta T/T \sim 10^{-5}$) due to density fluctuations in the last scattering epoch which could explain the inhomogeneity of the present Universe.

The properties of this anisotropy field can be studied by expanding it into a linear combination of spherical harmonics:

$$\frac{\Delta T}{T}(\theta, \varphi) = \sum_{l,m} a_{lm} Y_{lm}(\theta, \varphi), \quad (1.1.12)$$

with $l \sim \pi/\theta$ being inversely proportional to the angular scale θ . The a_{lm} coefficients are called *multipole moments* and according to current models they must have zero mean ($\langle a_{lm} \rangle = 0$ if the average is done for any observer in the Universe) and non-zero variance:

$$C_l \equiv \langle |a_{lm}|^2 \rangle, \quad (1.1.13)$$

where C_l is independent of m assuming the absence of a preferred direction. The set of C_l is known as the angular power spectrum and is the key theoretical prediction for any given model.

CMB anisotropies are said to be primary or secondary if they were originated before or after the decoupling epoch ($t = 3 \times 10^5$ y) respectively. There are three important effects leading to primary anisotropies:

Gravitational perturbations: Photons coming from high-density regions undergo a relativistic redshift due to the greater gravitational mass; this phenomenon is called “Sachs-Wolfe effect” (SW). The anisotropies have angular scales larger than the horizon at the last scattering ($\theta \gtrsim 2^\circ$), and are responsible for the features of the CMB spectrum for $l \lesssim 90$. If $\Delta\Phi$ is the gravitational potential, then the global effect of these anisotropies is

$$\frac{\Delta T}{T} = -\frac{\Delta\Phi}{3}. \quad (1.1.14)$$

Since this effect leads to $C_l \sim 1/(l(l+1))$, by plotting $l(l+1)C_l$ it is possible to recognize the plateau at small l due to the SW effect and directly link it to the initial spectral index.

Acoustic oscillations: In high-density regions radiation is compressed by the higher pressure and produces oscillations. Since recombination is a nearly instantaneous process, modes of acoustic oscillations with different wavelengths are “frozen” at different phases of oscillation. The

first peak in the CMB angular power spectrum (the so-called “Doppler peak”) is therefore due to a wave that as a density maximum just at the time of last scattering; the secondary peaks at higher l -s are high harmonics of the principal oscillations and have oscillated more than once. The effect is directly proportional to the density fluctuation $\Delta\rho$:

$$\frac{\Delta T}{T} \propto \frac{\Delta\rho}{\rho} \quad (1.1.15)$$

Doppler effects: The frequency of photons can be modified by the Doppler effect if the plasma has a non-zero speed at the last scattering epoch. The effect on the anisotropy is

$$\frac{\Delta T}{T} = \frac{\Delta v r}{c}, \quad (1.1.16)$$

where r is the distance and Δv the speed of the plasma relative to the observer.

In the short but finite time taken for the Universe to recombine, photons can diffuse a certain distance. Anisotropies on scales smaller than this mean free path will be erased by diffusion, leading to the quasi-exponential damping seen in the spectrum at large l -s. This is called “Silk damping”, and becomes quite effective at $l \gtrsim 1000$, corresponding to angular scales $\theta \lesssim 10'$. According to the current cosmological models, little contribution from primary CMB anisotropies is therefore expected at smaller scales.

Secondary anisotropies are due to scattering and other phenomena that take place in the path from the last scattering surface to the observer. Among these effects there are gravitational lensing (altering the direction of propagation of the CMB), the Sunyaev-Zel'dovic (SZ) effect (Compton scattering of the CMB photons with non-relativistic electron gas within clusters of galaxies) and other gravitational effects due to the time variation of the gravitational potential between the last scattering surface and us.

Figure 1.1 shows a sketch of a typical power spectrum.

The relative motion of our local frame with respect to the rest frame of the CMB leads to an anisotropy with $\Delta T/T \sim 10^{-5}$ mK which is called “dipole anisotropy” ($l = 1$). It was the first detected CMB anisotropy, in 1977 (see Smoot et al. 1977), and its signal can be written in the following form:

$$T_{\text{obs}} = T_0 \left(1 + \frac{v}{c} \cos \theta + \frac{1}{2} \left(\frac{v}{c} \right)^2 \cos 2\theta + O(v/c)^3 \right), \quad (1.1.17)$$

where θ is the angle between the line of sight and the direction of motion, and v is the velocity. The dynamic quadrupole (third term) is rather small ($\sim 1\%$ of the dipole), and it is quite below the intrinsic CMB cosmic quadrupole.

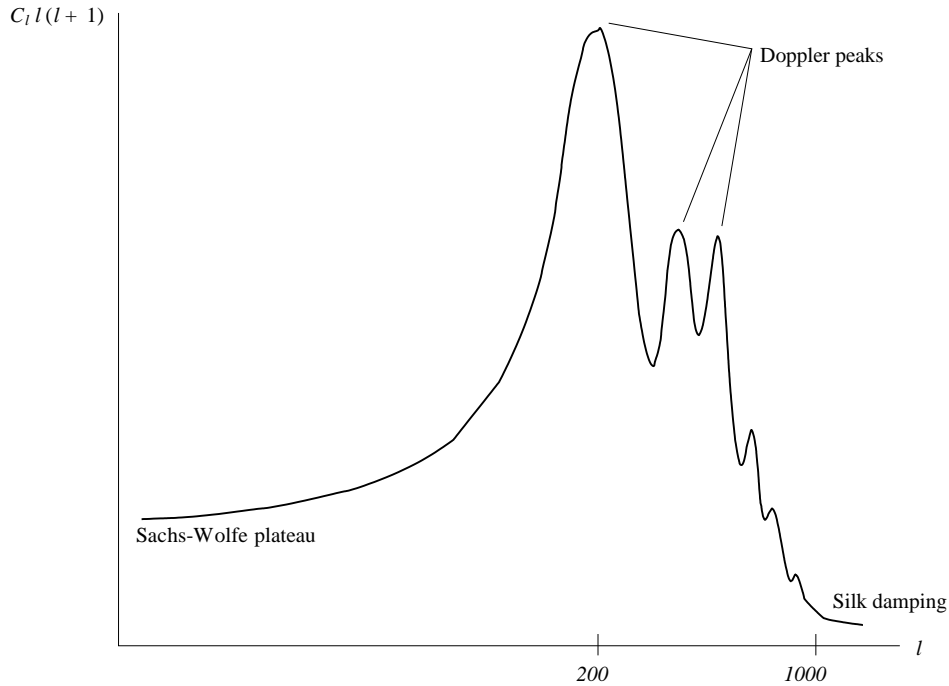


Figure 1.1: A typical power spectrum.

1.1.4. The Inflationary Model. Although the Hot Big Bang Model is successful, it leaves many open issues which have to be addressed. In the 1980s the “Inflationary Theory” was proposed in order to explain some of these problems (see Bucher and Spergel 1999, for a general introduction), most notably:

1. The measured value for ρ differs from ρ_{crit} for less than 10%: why is the density so close to the critical value? This is known as the “flatness problem”.
2. Since nothing cannot travel faster than light (3×10^{10} cm/s), any signal emitted in the first 3×10^5 years after the Big Bang could not travel more than $\sim 10^{16}$ cm; this distance is equivalent to an angle $\theta = ct_{\text{dec}} \sim 1^\circ$ on the last scattering surface. This apparently contradicts the evidence that the CMB shows an high uniformity even on larger angular scales.

The Inflationary Model solves these problems by supposing a quasi-exponential, superluminal dilation of the space immediately after the Big Bang ($t \lesssim 10^{-34}$ s) which can be modeled within the framework of General Relativity. Before this exponential expansion the observable Universe was small enough to become uniform: this explains the uniformity of the CMB

on large angular scales. Because inflation influences the curvature of the Universe, it has an effect on the critical density parameter Ω_0 too: according to the Inflationary Theory predictions and to the observed uniformity of the Universe, the critical density parameter should be $\Omega_0 = 1.00000 \pm 0.00001$ (note that according to current estimates $\Omega_0 = 1.0 \pm 0.1$).

§ 1.2 Importance of the CMB for Cosmology

A large number of processes can contribute to the generation of the CMB anisotropies. Theoretical works have established precise correlations between the CMB power spectrum and the value of the cosmological parameters used in the Hot Big Bang Model. The following is a short summary of the relations between these parameters and the CMB power spectrum features, taken from Bersanelli, Maino, and Mennella (2002):

Total density Ω_0 : The angular scale of the first peak is related to the value of Ω_0 by the relation $l \approx 200 \sqrt{\Omega_0}$.

Baryon density Ω_B : a large value of Ω_B increases the average height of the peaks, especially for the odd ones.

Hubble constant H_0 : small values of this parameter boost the peaks and slightly change their location in l -space.

Cosmological constant Λ : increasing this constant will also lead to a change in the peak height and in their position.

Spectral index n_S : a large value of this parameter will increase the peaks at large l -s with respect to the low l -s.

Reionization: if the intergalactic medium was re-ionized when $z \ll 1000$, then the power spectrum for $l > 100$ would be exponentially suppressed.

Nature of dark matter: if the critical density is provided by a mixture of cold ($\Omega_{\text{CDM}} > 0.7$) and hot ($\Omega_\nu < 0.3$) dark matter, as suggested by present observations, the angular power spectrum is expected to show systematic differences (at the level of $\sim 10\%$) compared with the $\Omega_{\text{CDM}} = 1$ case.

Gravitational wave background: gravitational waves generate additional CMB anisotropies, but only at large angular scales.

The study of CMB polarisation is another main goal of observational cosmology. As well as for the CMB temperature, polarisation anisotropies give a good test for the Hot Big Bang model. Their presence is predicted by theoretical calculations (see Hu and Dodelson 2002): they result from primordial

gravity waves and Thomson scattering between electrons and a radiation field with a local quadrupole moment. The ability to measure polarisation anisotropies offer the chance to triple the number of observed physical quantities, thus enhancing the constraints on cosmological parameters.

§ 1.3 Observation of the CMB

The first detection of the CMB signal was made by Penzias and Wilson (1965), which detected an excess of antenna temperature of about 3 K at 4 GHz while they were trying to measure the radio emission of our Galaxy (see Weinberg 1977). After having recognized its cosmic origin, the first experiments aimed to verify the isotropy and its planckian shape (“first generation experiments”). They provided a good frequency coverage (see for instance Bersanelli et al. 1994, for references about measurements in the $0.6 \div 90$ GHz range) and the blackbody planckian shape of the spectrum was definitively confirmed, with a temperature of ~ 2.73 K.

A new phase was opened by the COBE mission in the early '90, which was the first *second generation experiment*. The satellite carried three instruments (see The COBE Homepage, in the bibliography):

1. The Far Infrared Absolute Spectrometer (FIRAS) was a polarizing Michelson interferometer for analyzing the spectrum distribution of the CMB in the $0.1 \div 10$ mm wavelength range by comparing the sky signal with the reference signal of a blackbody at an angular resolution of $\sim 7^\circ$.
2. The Differential Microwave Radiometer (DMR) was an array of 6 differential radiometers which measured temperature anisotropies in the $31.5 \div 90$ GHz frequency range. Each differential radiometer measured the difference in power received from two directions in the sky separated by 60° , using a pair of horn antennas. Each antenna had a 7° (FWHM) beam.
3. The Diffuse Infrared Background Experiment (DIRBE) searched evidence of the cosmic infrared background (between $140 \mu\text{m}$ and $240 \mu\text{m}$).

COBE achieved two important results:

1. The COBE FIRAS experiment established that the CMB spectrum is planckian within a limit of 0.03% in the frequency range $60 \div 600$ GHz and a temperature of 2.728 ± 0.004 K (see Fixsen et al. 1996). This seems to be the best approximation of a blackbody ever found: see **figure 1.2** on the following page.
2. The COBE DMR found evidences of anisotropies on large angular scales ($36.5 \pm 5 \mu\text{K}$ at 7° , or $\Delta T/T \sim 10^{-5}$; see Bennett et al. 1996; Fixsen

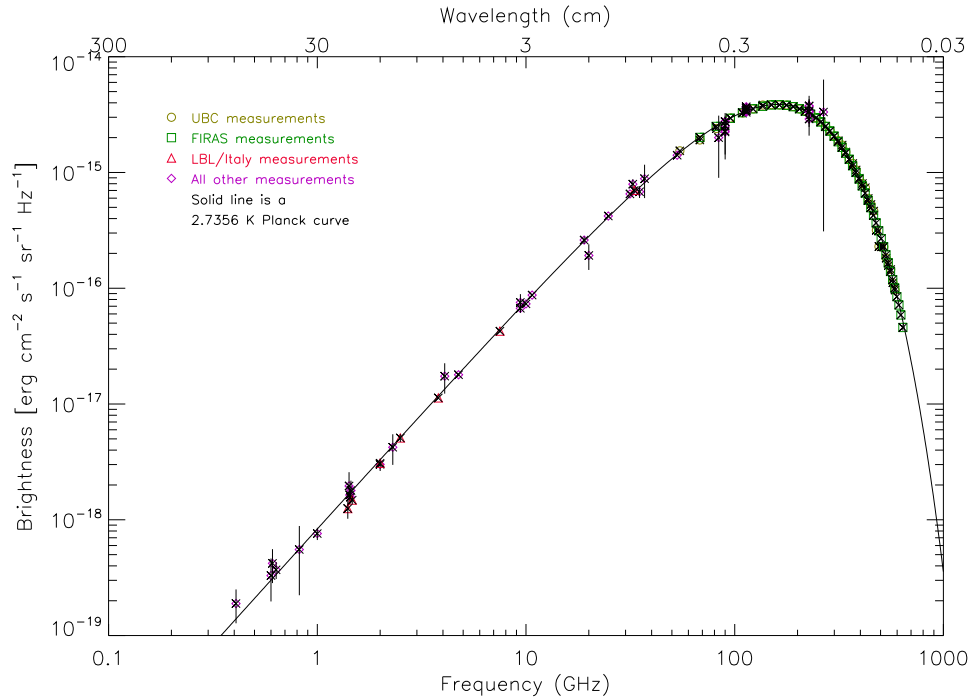


Figure 1.2: The CMB spectrum. The agreement between theory and observations is excellent.

et al. 1996). The anisotropies observed by the DMR are shown in **figure 1.3** on page 12.

After COBE, ground based and balloon borne experiments inevitably aimed at improving DMR measurements, which were limited by low angular resolution ($\sim 7^\circ$). In 1999 the BOOMERANG experiment provided a measurement of CMB anisotropies up to $l \sim 1000$, with a strong evidence of a first peak at $l \sim 200$ (see de Bernardis et al. 1999). BOOMERANG is a stratospheric balloon-based experiment which measures the CMB signal on a relatively wide region of the sky ($45^\circ \times 25^\circ$) at $90 \div 400$ GHz with a resolution of $\sim 10'$ by means of an array of bolometric detectors cooled at cryogenic temperatures and coupled to a parabolic mirror. The angular sensitivity of the instrument is about 12 arcmin.

After BOOMERANG other experiments showed consistent measurements of the angular power spectrum. Quite remarkable results have been produced by (see Bersanelli, Maino, and Mennella 2002, for a review): MAXIMA, a balloon-borne array of 16 cryogenic bolometers sensitive to multipoles $80 < l < 800$ in the $150 \div 240$ GHz range; DASI (Degree Angular Scale Interferometer) a ground-based interferometer sensitive to multipoles $100 < l < 900$ based on HEMT (High Electron Mobility Transistor) amplifiers in the spectral window $26 \div 36$ GHz; CBI (Cosmic Background Imager),

a ground-based array of 13 detectors based on HEMT amplifiers operating in the $26 \div 36$ GHz band with an angular resolution of $5' \div 1^\circ$ ($300 < l < 3000$). Furthermore very recently the DASI team reported the first detection of polarisation anisotropies which give strong validation to the theoretical framework of the Hot Big Bang Model (see Halverson et al. 2002).

The analysis of these experiments provides strong evidence for the cosmological interpretation of the CMB anisotropies. **Figure 1.4** on page 13 is a plot which combines the results obtained by the most important experiments on the observation of CMB anisotropies, and clearly reveals the presence of the first peak at $l \sim 200$; from this value it is possible to estimate Ω_0 to be 1.0 ± 0.1 .

Although good results can be achieved by ground-based and balloon-borne experiments (CBI reached an angular resolution of $\sim 5'$), full-sky measurements are impossible. In addition, emissions from the ground and the atmosphere impose severe limitations on the performances of these experiments (for example, antennas must have sidelobes reduced to ~ -110 dB in order to detect anisotropies with an amplitude of $\sim 30 \mu\text{K}$). For this reason two space missions have been conceived after COBE to fully extract the wealth of informations coded in the CMB.

MAP is a NASA space mission which will provide the first improved full sky maps of the CMB after COBE (see The MAP Homepage, in the bibliography). The satellite performs a measurements of the CMB with an angular resolution of $\sim 0.3^\circ$, with sensitivity of $\sim 35 \mu\text{K}$ per 0.3° squared pixel, and systematics artifacts limited to $5 \mu\text{K}$ per pixel. It is expected to reconstruct the power spectrum up to $l \sim 1000$. The observation is performed by means of two identical telescopes (pointing at two directions separated by $\sim 140^\circ$) and an array of passively cooled differential radiometers at five frequency bands from 22 up to 90 GHz.

The ultimate measurement of the CMB temperature anisotropy will be provided by the PLANCK mission, scheduled for 2007. It aims to provide a “definitive” measure of CMB temperature anisotropies, as well as the first full-sky measurement of polarisation anisotropies at high accuracy.

§ 1.4 Overview of the Planck Mission

PLANCK (see **figure 1.5** on page 15) is the mission currently developed by the European Space Agency (ESA), and is a *third generation mission*. Its purpose is to fully extract the cosmological information contained in the CMB temperature anisotropies from the whole sky with angular resolution ($5' \div 33'$), spectral coverage ($30 \div 887$ GHz) and sensitivity ($\Delta T/T \sim 10^{-6}$) such that the power spectrum reconstruction will be possible up to $l \sim 2500 \div 3000$ and limited by unavoidable cosmic variance and astrophysical foregrounds only.

To achieve this precision, two different instruments will be mounted on

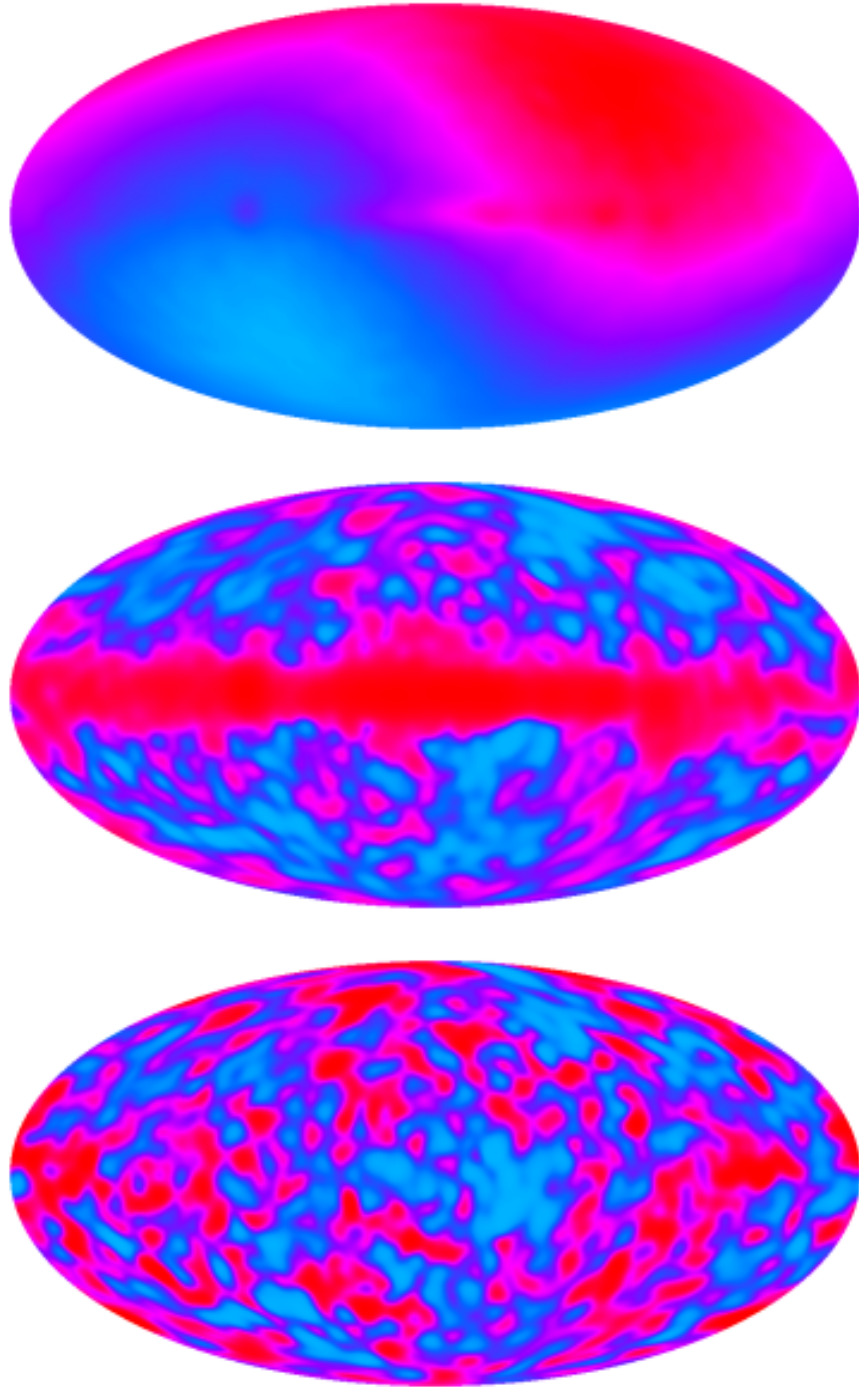


Figure 1.3: Maps generated with the COBE/DMR data. The raw samples are dominated by the 3 mK dipole (top); after a subtraction, the galactic emission is dominant (middle). By carefully removing them, the $30 \mu\text{K}$ CMB anisotropies become evident (bottom).

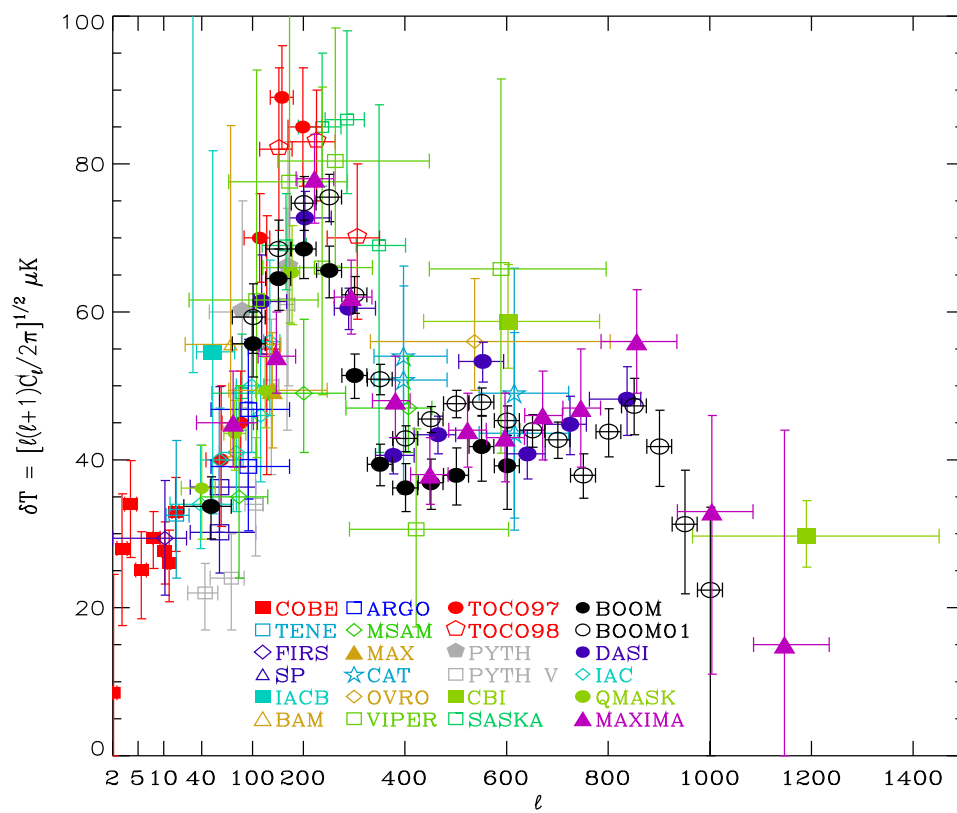


Figure 1.4: Current status of the CMB power spectrum measurements (from Bersanelli, Maino, and Mennella 2002).

PLANCK: the High Frequency Instrument (HFI) is an array of 48 bolometers cooled to 0.1 K for detecting radiation with $\nu \geq 100$ MHz, while the Low Frequency Instrument (LFI) is an array of 48 pseudo-correlation differential receivers based on HEMT (High Electron Mobility Transistor) technology cooled to ~ 20 K for detecting radiation with $\nu \leq 100$ MHz. Both the Low Frequency Instrument (LFI) radiometers and the High Frequency Instrument (HFI) bolometers are placed on the focal plane of an off-axis shaped aplanatic telescope with a primary of physical size 1.9×1.5 m. Because systematic effects would in general produce different responses in the two instruments, their frequency overlap at 100 GHz, near the minimum of foreground contamination and with similar angular resolution $\sim 10'$, is a valid tool to ensure that the systematic errors in the final maps are constrained under the required level ($\sim 3 \mu\text{K}$).

PLANCK will use a Lissajous orbit around L_2 (the Sun-Earth Lagrange point), this way the Earth and Sun will be always aligned in the same direction with respect to the satellite throughout the mission, which results in a high degree of thermal stability and low straylight levels. The scanning strategy is shown in figure **figure 1.6** on page 16: the spacecraft will spin around the Sun-PLANCK direction with a speed of ~ 1 rpm and will be repointed by $2.5'$ each hour: thus each circle will be scanned 60 times. The satellite is expected to perform two full scans of the sky, which means that the mission will last about 14 months.

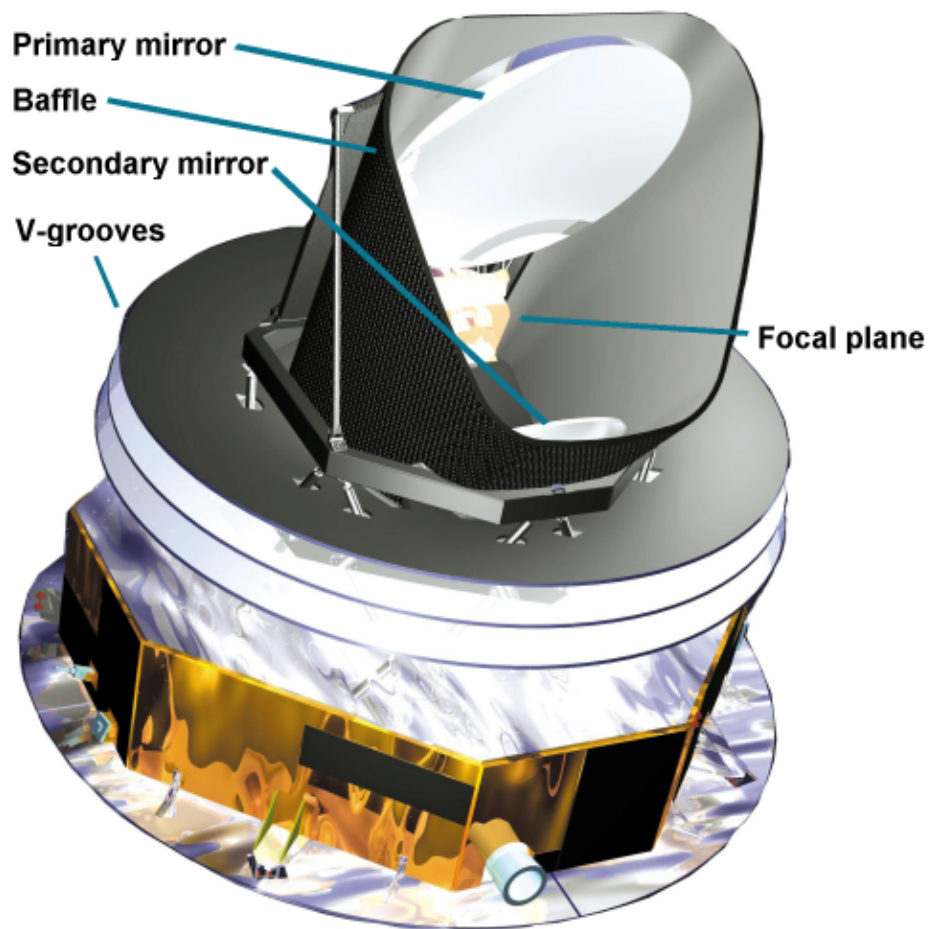


Figure 1.5: Overview of the Planck satellite, showing the primary reflector, the three thermal shields (“V-grooves”) used to thermally decouple the cold (~ 50 K) telescope enclosure from the warm (~ 300 K) service module, and the “baffle”, a shield which prevents straylight from reaching the focal plane (where HFI and LFI are placed).

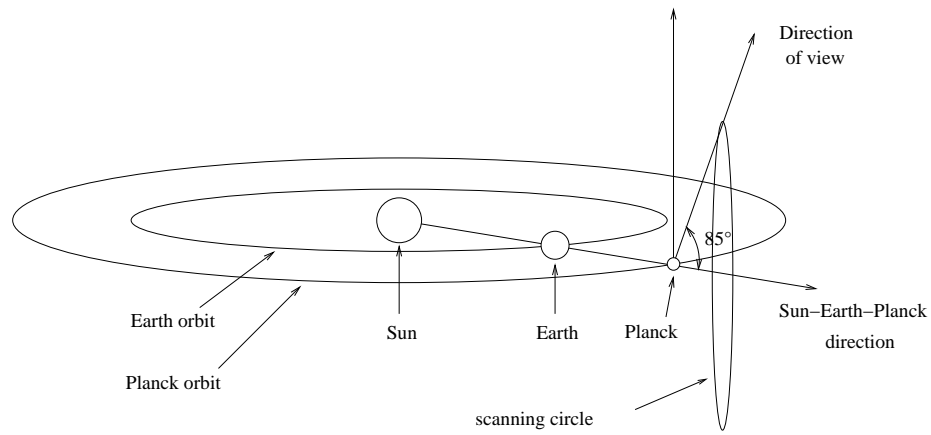


Figure 1.6: Sketch of the Planck scanning strategy (not in scale). Planck will use a Lissajous orbit around the L_2 point of the Sun-Earth system, and will scan the sky by spinning around the Sun-Earth-Planck direction with an angle of $\sim 85^\circ$. The sky temperature in each pixel will be measured 60 times for each scanning circle in about one hour; after this period, the spinning axis will be tilted by $\sim 2.5'$ and aligned to a new position.

CHAPTER 2

The Low Frequency Instrument

§ 2.1 Overview

The Low Frequency Instrument (LFI) represents the third generation of millimeter-wave radiometers designed for space observation of CMB anisotropies, following the COBE Differential Microwave Radiometer (DMR) and the Microwave Anisotropy Probe (MAP). It is an array of 48 differential, coherent radiometers based on InP HEMT amplifiers operating at ~ 20 K. The radiometer design uses a pseudo-correlation scheme in order to reduce non-white noise generated in the radiometers themselves: each of them measures the difference in temperature between the sky and a stable cryogenic reference load which is cooled at ~ 4 K by means of a thermal contact with the HFI external shield.

Because of the high sensitivity of the radiometers, careful control of systematic errors (that must be maintained at a level of $\leq 3 \mu\text{K}$) is required. These are mainly originated by $1/f$ fluctuations in amplifier gain and noise temperature, thermal and electrical effects, fluctuations in the reference signal, straylight, main beam imperfections and pointing errors. In particular, a high level of $1/f$ noise reduces the radiometer sensitivity and produces a “striping” effect in the final maps (see **figure 2.1**).

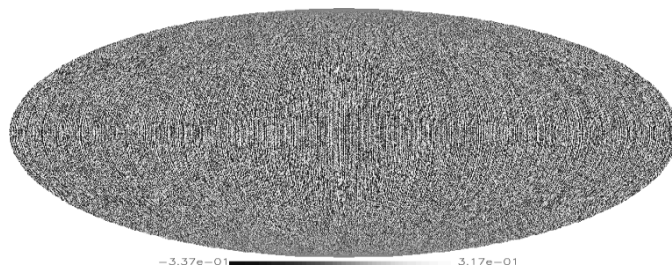


Figure 2.1: Simulated map (without foreground nor background sources). Temperature at each point is white and $1/f$ noise (from Maino et al. 1999).

The LFI radiometer design has good performances in reducing the $1/f$ noise of the amplifiers: the estimated knee frequency in the radiometer output is $\nu_{\text{knee}} \sim 0.1$ Hz (this means that $1/f$ noise is prevalent over white noise only if $\nu < \nu_{\text{knee}}$) and is mainly due to amplifier noise temperature fluctuations. To obtain these results, LFI will use a pseudo-correlation receiver concept: we shall explain this topic with greater detail in the next sections.

The overall structure of the instrument is shown in **figure 2.2**. It is divided into two parts: a cold front-end unit and a warm back-end unit. The feed horns are placed in the *front-end unit* (~ 20 K), in the focal plane of the telescope. The front-end electronics pre-amplifies and the sky and reference signals which propagate through a set of waveguides into the *back-end unit* (~ 300 K). Here the signal is further amplified and digitized. In the following paragraphs we shall provide a more detailed description of the radiometers.

§ 2.2 Radiometers

The structure of a LFI radiometer is shown in **figure 2.3** on page 20. In the front-end part (see top part of **figure 2.4**) the radiation entering the feed-horn is separated by an OrthoMode Transducer (OMT) into two perpendicular linearly polarized components that propagate independently through two parallel radiometers. In each radiometer the sky signal is coupled to a stable reference load at 4 K by a 180° hybrid and then amplified by low-noise High Electron Mobility Transistor (HEMT) amplifiers. One of the two signals then runs through a switch that applies a phase shift which oscillates between 0 and π with a frequency of 4096 Hz. A second phase switch is present for symmetry on the second radiometer leg; this switch will introduce no phase shifts in the propagating signal. The signals are then recombined by a second 180° hybrid coupler, so that the output is a sequence of signals alternating at twice the phase switch frequency.

In the back-end of each radiometer (see bottom part of **figure 2.4** on page 20) the signals are further amplified, filtered by a low-pass filter and then detected. After detection the sky and reference load signals are integrated, digitized and then differenced after multiplication of the reference load signal by a so-called *gain modulation factor* r , which makes the sky-load difference as close as possible to zero.

According to this architecture each radiometer will produce two independent streams of sky-load differences; the final measurement is provided by a further average of these differenced data samples between the two radiometer legs.

The LFI pseudo-correlation design offers two main advantages: the first is that the radiometer sensitivity does not depend (at first order) on the level of the reference signal (see Seiffert et al. 2002); the second is provided by the fast switching that reduces the impact of $1/f$ fluctuations of back-end amplifiers. In fact, if the gain modulation parameter is correctly set,

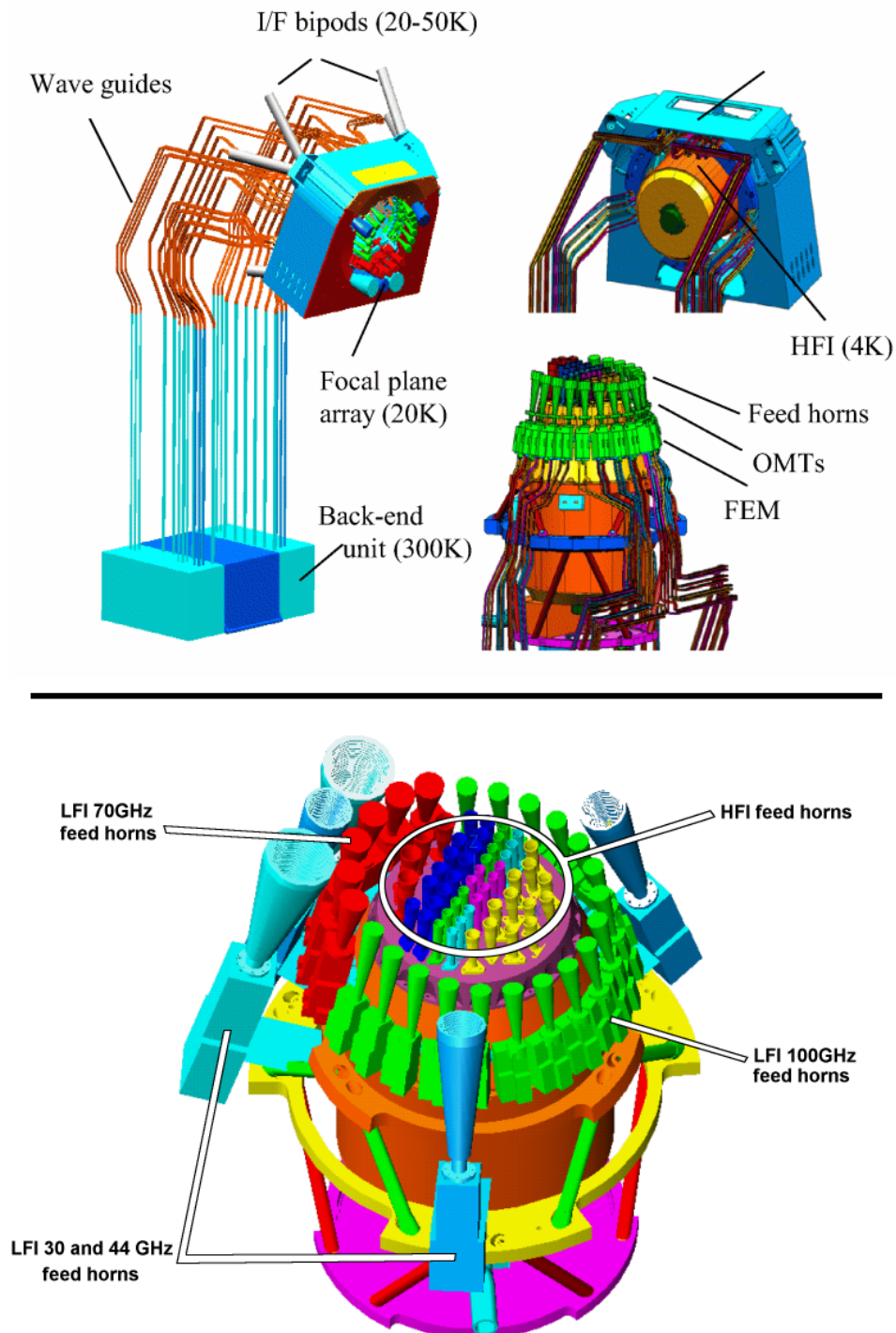


Figure 2.2: Top drawing: the LFI radiometer array assembly (left) with details of the front-end main frame (upper right) and of the front-end feed array (lower right). Bottom drawing: the Planck focal plane with the LFI and HFI antennae.

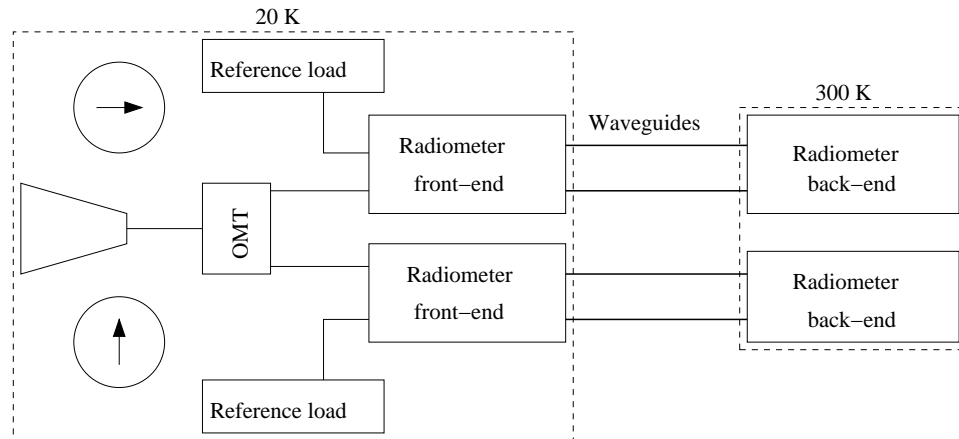


Figure 2.3: Overview of a LFI radiometer. The sky signal is split into the two polarisation components, and both are compared with the signal coming from a reference blackbody at ~ 4 K.

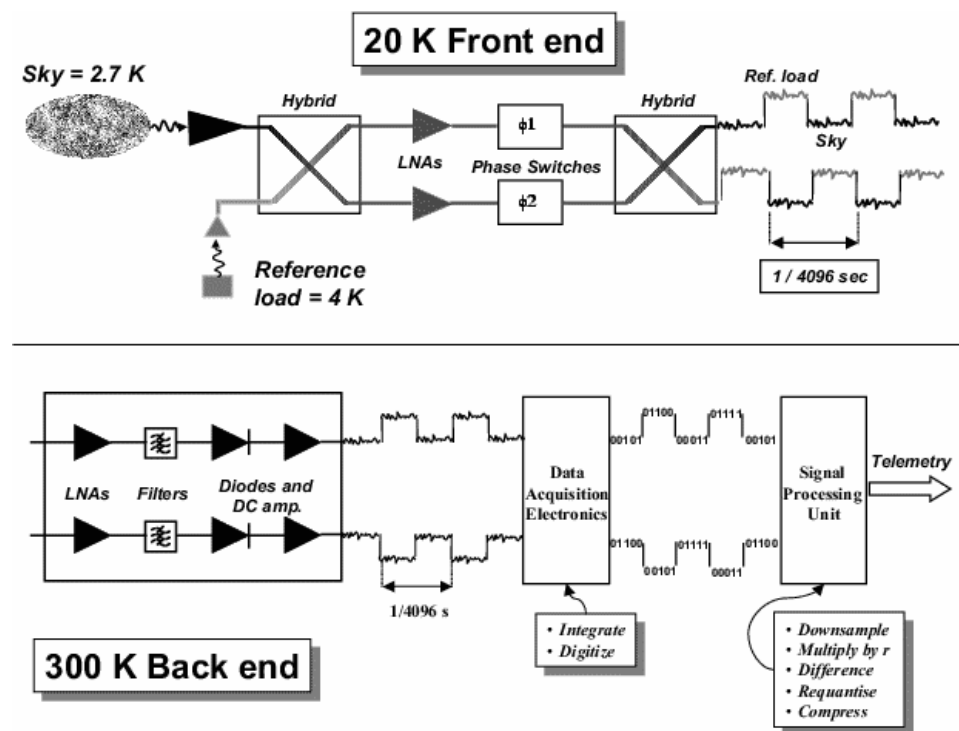


Figure 2.4: Detailed outline of a LFI radiometer front-end (top) and back-end (bottom). The front-end output signal is transmitted through actively-cooled waveguides and becomes the input signal for the back-end part of the radiometer. For the full explanation, see the text.

the dominant source of $1/f$ noise in the radiometer output is the amplifier noise temperature fluctuations with a knee frequency of $\sim 50 \div 100$ mHz. Imbalances in the two legs are not relevant at the first order.

§ 2.3 Reference Loads

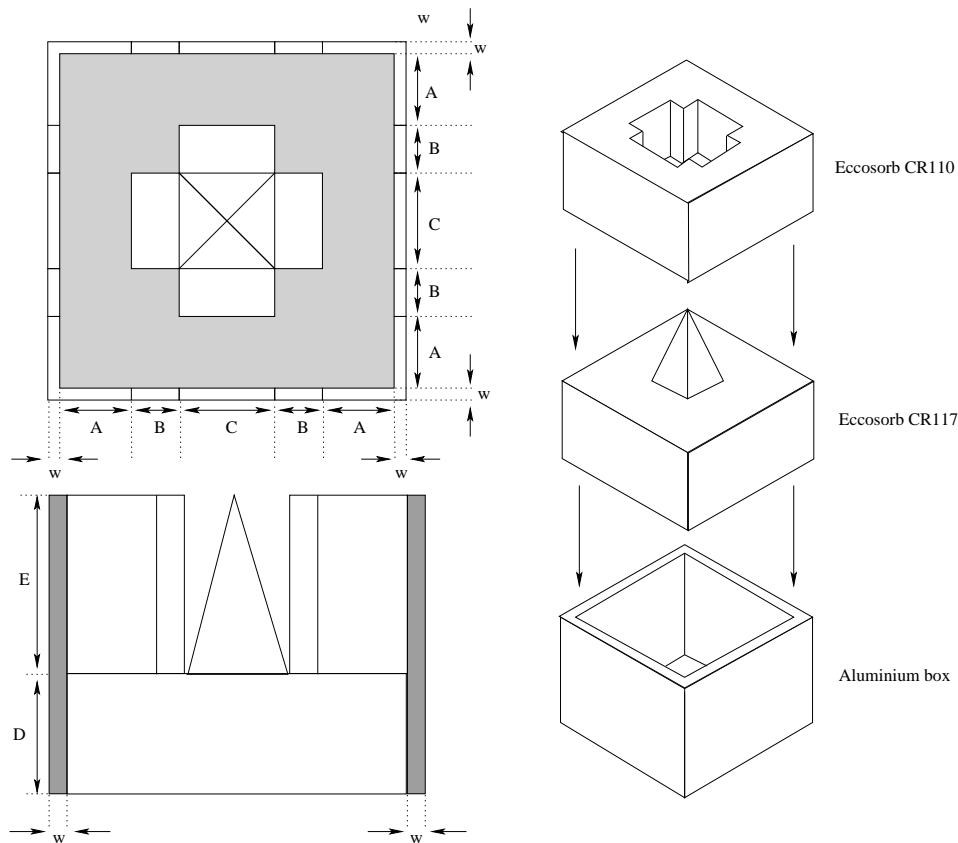


Figure 2.5: Representation of a Reference Load. It is made by two pieces of Eccosorb (CR110 and CR117), a material with high emissivity. They are placed into a metallic box which is placed on the external shield of HFI with a thickness equal to w (the exact value has not been defined yet; it will be $\sim 0.1 \div 1.0$ mm).

Reference Load (RL)s are small boxes made of Eccosorb, a high-emissivity material, which are used as reference blackbodies for the LFI radiometers. They are cooled by means of a thermal contact with the HFI external shield, which is actively cooled to ~ 4 K in order to be used as a pre-cooling stage for the 0.1 K HFI bolometers.

The Reference Load (RL)s are designed in order to minimize electromagnetic reflections and provide an optimized coupling with the LFI reference antenna (see **figure 2.5**). Typical sizes for RLs are reported in **table 2.1** on the following page:

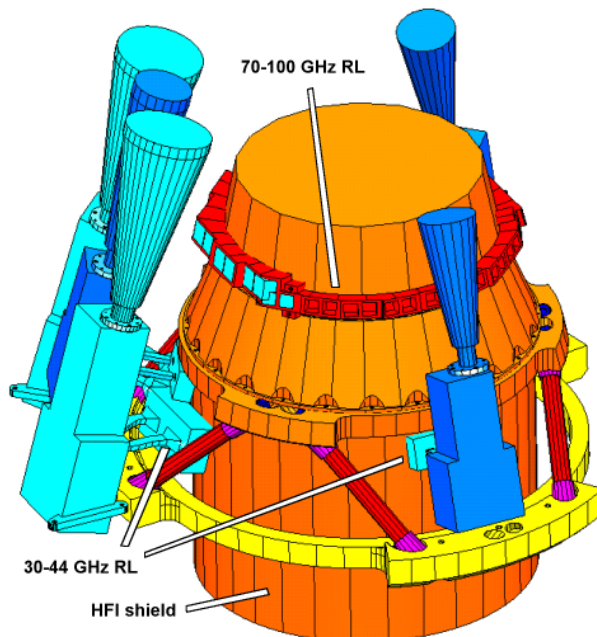


Figure 2.6: Placement of the reference loads on the HFI external shield. The 70 GHz and 100 GHz are placed on a metallic belt which is thermally linked to HFI while the 30 GHz and 44 GHz (in the figure they are partially hidden by their reference feed horns) are in direct thermal contact with the HFI shield.

Frequency (GHz)	<i>A</i>	<i>B</i>	<i>C</i>	<i>D</i>	<i>E</i>
30	0.587	0.540	1.079	0.500	1.467
44	0.400	0.369	0.736	0.500	1.000
70	0.251	0.232	0.463	0.500	0.629
100	0.176	0.162	0.324	0.500	0.440

Table 2.1: Sizes for the RL as indicated in figure 2.5. Every length is measured in centimeters.

§ 2.4 The Planck 20 K and 4 K Coolers

Several cryogenic stages will be present on-board the PLANCK satellite which will be provided by a chain of three dedicated cryo-coolers. A key role in this chain is played by the PLANCK Sorption Cooler (SC), a vibrationless hydrogen cooler in which hydrogen is pumped by inducing pressure changes through a chemical sorption process. This cooler will provide ~ 1 W of cooling power at 20 K to cool the LFI radiometers and pre-cool the HFI 4K helium cooler.

A schematic of the SC is shown in **figure 2.8** on page 24. The compressor assembly will be mounted in the warm PLANCK Service Module (SVM) (in figure 1.5 it is the bottom part of the satellite, under the three v-grooves) and is composed by six cylinders containing a hydride material able to absorb

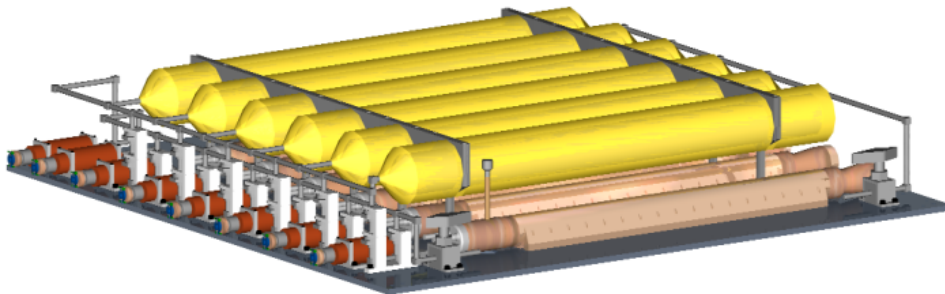


Figure 2.7: The Planck sorption cooler, with the six compressor beds and their check valves.

and release hydrogen depending on temperature. Hydrogen is compressed in each of the six beds (see figure 2.7), which are connected to the high and low pressure sides of the system through check valves (whose direction of flow is indicated by white arrows in the figure), and cools down to 20 K by means of a J-T expander after three pre-cooling stages to 140 K, 80 K and 50 K (the V-grooves shown in figure figure 1.5 on page 15). After the J-T cooler there are three heat exchangers (LR, from “Liquid Reservoir”), indicated with LR#1, LR#2 and LR#3. LR#2 is directly connected to the LFI structure, while LR#1 provides a pre-cooling stage for the HFI 4 K cooler; temperature at this point must therefore be very stable (the peak-to-peak temperature fluctuation amplitude is required to be < 100 mK).

The cooler compressors are periodically cycled between heating and cooling phases, so that the whole assembly produces a stationary flow of high pressure gas. In such a system there is a basic clock time period over which each step of the process is conducted: for each compressor the duration of each phase is 667 s, so that the six compressor elements are cycled successively through the steps in the process with one complete cycle taking as baseline $667 \text{ s} \times 6 \approx 4000 \text{ s}$.

In the PLANCK cryogenic chain the 4 K cooler has two purposes: (1) to cool the focal plane unit to 4 K, and (2) to provide a pre-cooling stage for the HFI 100 mK dilution cooler, used to cool the HFI bolometers (see Bradshaw 1999). The 4 K cooler system is composed by a mechanical compressor which provide an high pressure stream of helium (~ 10 bar) and a Joule-Thomson expander which forces the high pressure gas to cool off and condense by passing through a throttle.

The stability of the temperature at the HFI/RL interface depends on intrinsic fluctuations of both the 4 L cooler and 20 K cooler, as well as the thermal-mechanical properties of the two instruments.

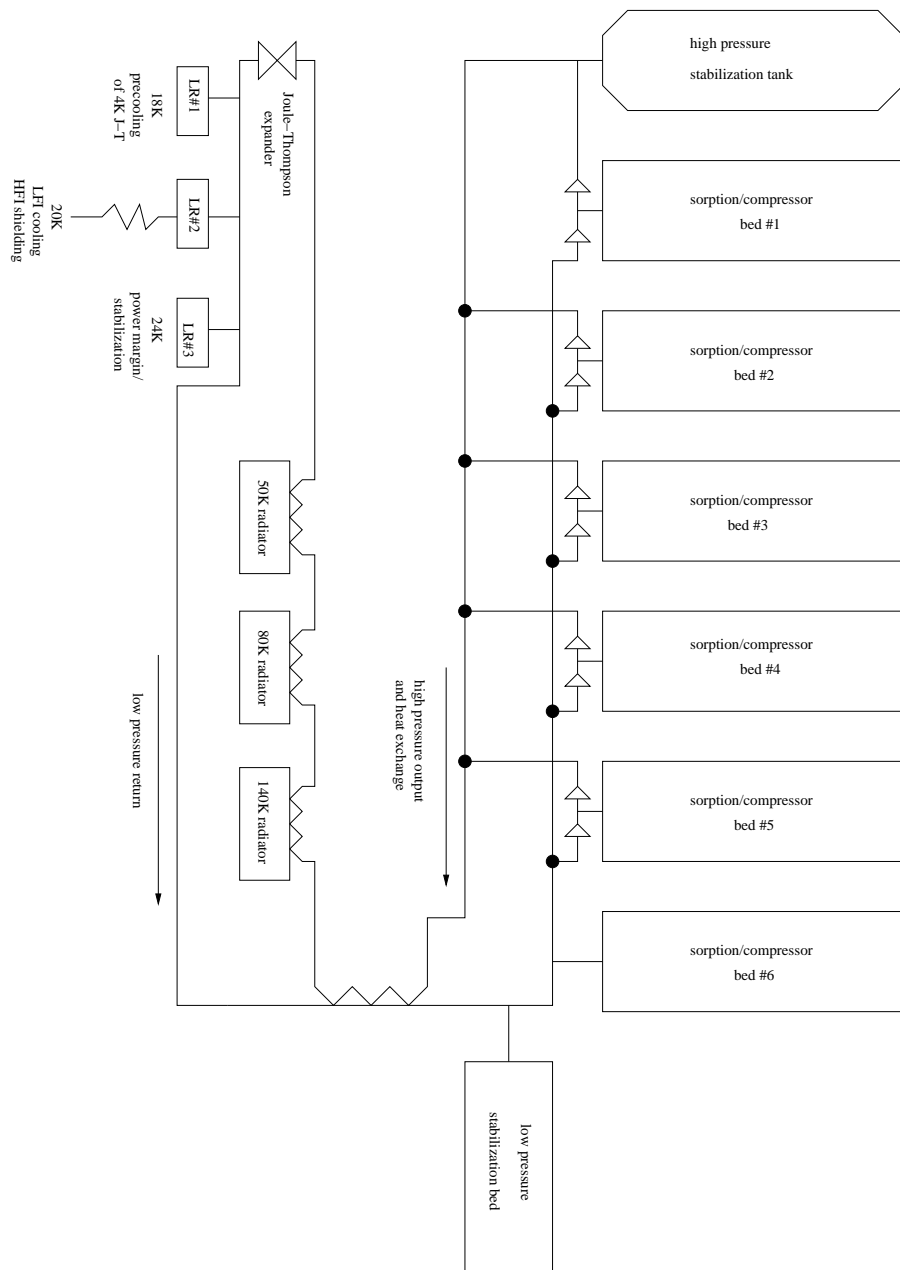


Figure 2.8: Schematic of the sorption cooler system used on the Planck spacecraft. For details see the text.

§ 2.5 Sources and Control of Systematic Errors

The strict requirements on PLANCK instruments are motivated by the science of interest: CMB anisotropies give a small signal ($\Delta T/T \sim 10^{-5}$) to be detected with high signal-to-noise ratio by the instruments, and a key factor for the success of the mission is a strict control of systematic effects at the μK level in the final maps.

Systematic errors can be of celestial and instrumental origin, leading to wrong measurements of the CMB signal (see Mennella et al. 2002). The following are the most important sources of systematics:

Celestial Sources. The solar radiation that reaches the PLANCK spacecraft varies in time, thus leading to possible systematic errors. These effects are reduced by the scanning strategy of the spacecraft: with the relatively tight spacecraft orbit around L_2 Sun and Earth are aligned along the spin axis throughout the mission, thus avoiding direct illumination of the instruments. Furthermore telemetry and command antennas can be pointed away from the payload thereby minimizing the potential effects of radio frequency interference.

Stray Radiation. Tightly linked to the previous topic is the reduction of stray radiation. This is the radiation coming into the feed horn that comes from directions not along the axis of the antenna. The Sun, the Earth and the Moon are the primary celestial possible sources of stray radiation, but the various components of the spacecraft (baffle, V-grooves) may also contribute. To reduce the effect from stray radiation it is necessary that the optical system (telescope, feeds, baffle) is designed to have a high sidelobe rejection ($\sim 80 \div 100$ dB) and emitting surfaces must be characterised by a high degree of thermal stability.

$1/f$ Noise and Striping. Unlike white noise, $1/f$ noise produces a correlated effect on the output and therefore leads to artifacts on the final CMB maps (see figure 2.1). The LFI radiometer architecture is able to reduce this noise to a good extent (the knee frequency of the noise in the radiometer output signal is ~ 0.05 Hz), but $1/f$ fluctuations cannot be completely removed. Numerical methods for removing this effect from the measured data have been developed (see Mennella et al. 2002, for more informations). These have provided to be very effective for knee frequencies up to ~ 0.2 Hz.

Thermal Effects. Last but not least, thermal effects have a great importance for microwave experiments at cryogenic temperatures, like PLANCK. They are such a critical issue that thermal design is one of the primary mission design driver.

Unlike the back-end module, which will work at ~ 300 K, the front-end module will be cooled to an average temperature of ~ 50 K, in order

to reduce instrumental thermal noise. Thermal insulators between the two modules are implemented in order to keep insulation and to avoid dangerous shorts; large radiating surfaces are placed on the payload in order to dissipate heat.

From the point of view of the LFI, particular care has to be taken for the thermal stability of the amplifiers and the reference loads (the latter is the topic of this thesis).

§ 2.6 General Thermal Stability Requirements

In general we can identify three different types of thermal fluctuations for which different requirements must be formulated.

Random noise fluctuations. This is the well-known “white noise”: its spectrum is essentially flat. This kind of noise is uncorrelated and it does not produce systematic errors but causes a sensitivity reduction that can be compensated (in principle) by increasing the number of measurements N (the error is $\delta \sim N^{-1/2}$).

Periodic spin-synchronous fluctuations. Periodic fluctuations with a frequency ν such that $\nu = \nu_{\text{spin}}/k$ with $k \in \mathbb{N}$ are called “spin-synchronous” fluctuations (ν_{spin} is the PLANCK spin frequency, $\sim 1/60$ Hz). This kind of noise can have a strong impact on the final maps because it cannot be damped by the measurement redundancy (unlike white-noise).

Periodic non-spin-synchronous fluctuations. These fluctuations can be damped by the measurement redundancy, since the signal coming from each resolution element in the sky will be measured approximately 60 times during a scan (the time interval between two consecutive measurements is ~ 60 s).

More detailed discussion about systematic effects induced by thermal noise in PLANCK can be found in Seiffert et al. (2002); Mennella et al. (2001, 2002).

§ 2.7 Requirements on Reference Load Thermal Stability

Reference loads give the reference signal for the LFI radiometer chains, and are therefore expected to give a stable signal: the requirements are shown in **table 2.2**.

Random noise fluctuations	$< 10^{-5} \text{ K}/\sqrt{\text{Hz}}$
Spin-synchronous fluctuations	$1 \mu\text{K}$
Non spin-synchronous fluctuations	$\sim 0.5 \text{ mK}$

Table 2.2: Stability requirements for RL temperature variations.

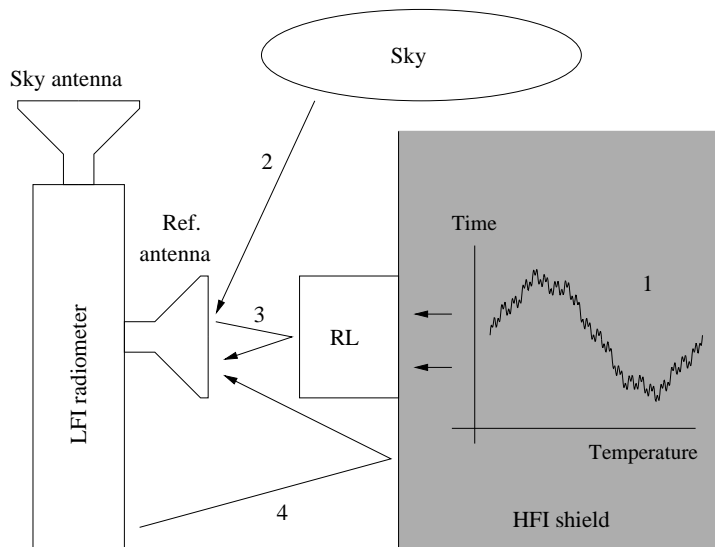


Figure 2.9: Possible sources of systematic errors in the reference signal: (1) temperature fluctuations in the HFI shield, (2) straylight from the sky (spin-synchronous effect), (3) reference antenna radiation reflected back by the reference load, (4) reflected radiation from the LFI radiometers.

Possible sources of systematic errors in the reference signal are (see **figure 2.9**):

1. RLs are cooled by means of a thermal contact with the HFI shield, so HFI thermal stability directly influences RLs performances. There are few details about the HFI shield temperature stability, but we can infer that, since the HFI cooling system uses the LFI LR#2 as a pre-cooling stage, any fluctuation in the HFI temperature will show a relatively strong spectral component around the 4000 s and 667 s periods.
2. Straylight coming from the sky can be reflected in the reference antenna.
3. Reflection of the electromagnetic radiation¹ coming from the reference antenna produces an effect that is correlated with temperature fluctuations in the antenna itself.
4. Radiation coming from other components of both LFI and HFI can be confused with the reference signal.

In order to address these issues, a thermal model of the RLs has to be developed and then integrated into a complete radiative model. This work presents a conductive thermal model for the RLs which provide a good

¹The RL is not a perfect blackbody and its reflectivity is therefore not zero

starting point to address some of the previous issues. Topics covered in the following chapters are:

- propagation of temperature fluctuations coming from HFI in the RLs;
- propagation of temperature fluctuations induced by the radiative heat flux coming from LFI in the RLs;
- implementation of a thermal insulators between the reference load and the HFI shield in order to damp temperature fluctuations coming from HFI.

CHAPTER 3

The Heat Equation and its Application to LFI

To study the conductive properties of the reference loads in the PLANCK LFI instrument, one needs to know how heat propagates in a solid body. The heat equation (also known as the *diffusion equation*, since it can describe diffusion of particles in free space as well as the conduction of heat in a solid body) will be our most useful tool.

§ 3.1 Derivation of the Equation

We are going to use thermodynamics and the Fourier equation to deduce the heat equation. This equation describes how temperature in a solid body changes in time in terms of three physical constants: mass density, heat capacity and heat conductivity. We shall use this equation extensively to study the LFI reference load thermal properties.

The solid body under study is assumed not to change its size under temperature variations. This is without doubt the case of the LFI reference loads. The First Principle of Thermodynamics becomes

$$dU = dQ, \quad (3.1.1)$$

where U is the internal energy, and dQ is the exchanged heat (we neglect the work done by the system dW because the body does not change its size). In a small volume dV , the variation in internal energy is

$$dU = Mc dT = \rho c dV dT, \quad (3.1.2)$$

where M is the body mass and c the specific heat ($[c] = \text{erg g}^{-1} \text{K}^{-1}$). The exchanged heat is given by the sum of two terms:

$$dQ = dQ_{\text{int}} + dQ_{\text{sc}}. \quad (3.1.3)$$

The first factor on the right side is due to the heat generated by the body itself (caused by nuclear or chemical processes, like the Johnson effect in an electrical conductor). The second factor is the conductive term: it takes care of any heat flowing into or out from the volume.

We can rewrite dQ_{int} as

$$dQ_{\text{int}} = \dot{q}_g dV d\tau, \quad (3.1.4)$$

where $d\tau$ is a small time interval, \dot{q}_g is the heat power density generated by the body ($[\dot{q}_g] = \text{erg/s/cm}^3$).

The conductive heat can be written in the following way:

$$dQ_{\text{sc}} = -d\tau \int_{dS} \mathbf{j}_q \cdot \mathbf{n} dS, \quad (3.1.5)$$

where \mathbf{j}_q (the heat flux, $[j_q] = \text{J cm}^{-2} \text{ s}^{-1}$) is positive if it enters into the surface dS , negative otherwise; vector \mathbf{n} is the surface normal (which points outside). By using the Gauss theorem and the Fourier equation

$$\mathbf{j}_q = -k \nabla T \quad (3.1.6)$$

which relates temperature with the heat flux and the *thermal conductivity* k ($[k] = \text{erg/s/m/K}$), we can write this term as

$$dQ_{\text{sc}} = \nabla \cdot (k \nabla T) dV d\tau. \quad (3.1.7)$$

Thermal conductivity can be assumed independent from \mathbf{x} in a homogeneous medium; in this case we can write:

$$\nabla \cdot (k \nabla T) = k \nabla^2 T \quad (3.1.8)$$

By substituting into equation (3.1.1) the new quantities given by equation equations (3.1.2), (3.1.4) and (3.1.7) and then dividing by $d\tau$, we obtain the heat conduction equation:

$$k \nabla^2 T(\mathbf{x}, t) + \dot{q}_g(\mathbf{x}, t) = c\rho \frac{\partial T}{\partial t}(\mathbf{x}, t). \quad (3.1.9)$$

§ 3.2 General Properties of the Equation

Equation (3.1.9) is the most important tool we shall use in this work. Being a Partial Differential Equation (PDE), in order to get a unique solution of the problem we must specify proper boundary conditions (the so-called *Cauchy conditions*) and an initial condition. But some of the features of equation (3.1.9) can be obtained even without stating precise boundary/initial conditions. In this section we derive some properties satisfied by the solutions of this equation.

3.2.1. Canonical Solution. In the next paragraphs we shall find a general solution of equation (3.1.9) on the preceding page using the theory of generalized functions to get a solution of (3.1.9); this solution will not consider boundary conditions nor initial conditions. Although this is not the solution we shall use in next chapters, it is possible to understand what kind of solutions we shall obtain when solving real-world problems.

We start from the equation in n dimensions by considering an impulsive point source of heat:

$$T_t(\mathbf{x}, t) - D \nabla^2 T(\mathbf{x}, t) = \chi \delta^n(\mathbf{x}) \delta(t), \quad (3.2.1)$$

where χ is a parameter which is related to the source “strength” ($[\chi] = \text{K cm}^n \text{ s}^2$, with n being the number of dimensions). Equation (3.2.1) describes how a system reacts to a point impulse at $\mathbf{x} = 0, t = 0$. As initial condition, we can let $T(\mathbf{x}, t) = 0$ if $t < 0$ (this means that before the impulse the body temperature is equal to absolute zero).

Deriving the solution of this equation is simpler if we use the Fourier transform¹ to the x variable:

$$\hat{T}_t(\mathbf{k}, t) + D \|\mathbf{k}\|^2 \hat{T}(\mathbf{k}, t) = \frac{\chi}{(2\pi)^{n/2}} \delta(t). \quad (3.2.2)$$

Since the Fourier transform is a linear operator, if $T(\mathbf{x}, t) = 0$ for $t < 0$ then $\hat{T}(\mathbf{k}, t) = 0$ if $t < 0$ too. The solution is

$$\hat{T}(\mathbf{k}, t) = \frac{D\chi}{(2\pi)^{n/2}} \theta(t) \exp(-D\|\mathbf{x}\|^2 t), \quad (3.2.3)$$

where $\theta(x)$ is the characteristic function of \mathbb{R}^+ :

$$\theta(x) = \begin{cases} 1 & \text{if } x \in \mathbb{R}^+, \\ 0 & \text{if } x \in \mathbb{R}_0^-. \end{cases} \quad (3.2.4)$$

Because $\hat{T}(\mathbf{k}, t)$ is a gaussian in the x variable, then if we transform it back to $T(\mathbf{x}, t)$, the result is a gaussian as well, usually indicated with F in the literature:

$$F(\mathbf{x}, t) = \frac{a\chi}{(4\pi t)^{n/2}} \theta(t) \exp\left(-\frac{\|\mathbf{x}\|^2}{Dt}\right) \quad (3.2.5)$$

A plot of this function (using $n = 1$) is shown in figure 3.1 on the next page.

¹Our conventions about the Fourier transform and its inverse are given here:

$$\begin{aligned} \hat{f}(\mathbf{k}) &\equiv \left(\frac{1}{2\pi}\right)^{n/2} \int_{\mathbb{R}^n} f(\mathbf{x}) e^{-i\mathbf{k}\cdot\mathbf{x}} d\mathbf{x}, \\ f(\mathbf{x}) &\equiv \left(\frac{1}{2\pi}\right)^{n/2} \int_{\mathbb{R}^n} \hat{f}(\mathbf{k}) e^{+i\mathbf{k}\cdot\mathbf{x}} d\mathbf{k}. \end{aligned}$$

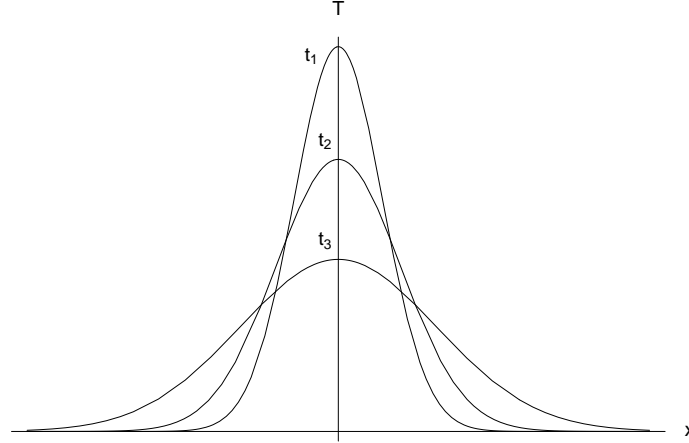


Figure 3.1: Evolution of temperature in a conductive body after a point impulse of heat $\chi \delta(x) \delta(t)$. The temperature profile is shown in three consecutive times $t_1 < t_2 < t_3$. Note how the peak is more and more smoothed for increasing times.

Let us now generalize this solution by considering heat sources of any kind, i.e.

$$\frac{1}{D} T_t(\mathbf{x}, t) - \nabla^2 T(\mathbf{x}, t) = \frac{p(\mathbf{x}, t)}{k}, \quad (3.2.6)$$

where p is the heat flux coming from the heat source ($[p(\mathbf{x}, t)] = \text{erg/s/cm}^2$).

The solution can be obtained by a linear combination of the “point source” equation (3.2.5):

$$T(\mathbf{x}, t) = \iint_{\mathbb{R}^{n+1}} F(\mathbf{x} - \boldsymbol{\xi}, t - \tau) \frac{p(\boldsymbol{\xi}, \tau)}{k} d\boldsymbol{\xi} d\tau. \quad (3.2.7)$$

To prove this is the solution of the heat equation, we substitute equation (3.2.7) into equation (3.2.6)

$$\begin{aligned} \frac{1}{D} T_t(\mathbf{x}, t) - \nabla^2 T(\mathbf{x}, t) &= \\ &= \iint_{\mathbb{R}^2} \left(\frac{1}{D} F_t(\mathbf{x} - \boldsymbol{\xi}, t - \tau) - \nabla^2 F(\mathbf{x} - \boldsymbol{\xi}, t - \tau) \right) \frac{p(\boldsymbol{\xi}, \tau)}{k} d\boldsymbol{\xi} d\tau = \\ &= \iint_{\mathbb{R}^2} \delta(\mathbf{x} - \boldsymbol{\xi}) \delta(t - \tau) \frac{p(\boldsymbol{\xi}, \tau)}{k} d\boldsymbol{\xi} d\tau = \frac{p(\mathbf{x}, t)}{k}. \end{aligned}$$

Let us enumerate some properties of equation (3.2.7):

1. It can be written as

$$T(\mathbf{x}, t) = \frac{1}{k} (F * p)(\mathbf{x}, t). \quad (3.2.8)$$

If $T(\mathbf{x}, t)$ is given by a convolution, then its Fourier transform $\hat{T}(\mathbf{k}, \omega)$ is expressed by a product:

$$\hat{T}(\mathbf{k}, \omega) \propto \hat{F}(\mathbf{k}, \omega) \hat{p}(\mathbf{k}, \omega) \quad (3.2.9)$$

(neglecting any conversion factor). Note that $\hat{F}(\mathbf{k}, \omega)$ is different from equation (3.2.3), since here we applied the Fourier transform not only in space, but in time too.

This result is very important, although it can be underrated. The formula states that the value of \hat{T} at a given frequency ω depends only on the value of \hat{p} at that frequency²: the value of \hat{T} at ω depends on p evaluated at ω only. From this we can infer that if p is of the form

$$p(\mathbf{x}, t) = \sum_{n=0}^N \psi_n(x) \cos(\omega_n t), \quad (3.2.10)$$

then \hat{p} will be equal to the sum of N Dirac's deltas:

$$\hat{p}(\mathbf{k}, \omega) = \sum_{n=0}^N w_n \hat{\psi}(x) \delta(\omega - \omega_n) \quad (3.2.11)$$

(where w_n are the constants introduced by transforming \cos into δ), and the solution will be

$$\hat{T}(\mathbf{k}, \omega) = \begin{cases} \frac{1}{k} \hat{F}(\mathbf{k}, \omega) \hat{\psi}(x) & \text{if } \omega = \omega_n \text{ for some } \omega_n, \\ 0 & \text{otherwise.} \end{cases} \quad (3.2.12)$$

This means that the system is *linear*, i.e. temperature at any given point has the same frequency components that are present in the heat source.

2. It follows from the linearity of the heat equation that any function

$$\tilde{T}(\mathbf{x}, t) = (\mathbf{A}\mathbf{x} + \mathbf{b}) T_0 + T(\mathbf{x}, t), \quad (3.2.13)$$

with \mathbf{A} (matrix) and \mathbf{b} (vector) being arbitrary quantities independent from \mathbf{x} and t , is a solution of equation (3.2.6) on the preceding page.

3.2.2. Boundary Conditions and Heat Sources. We have studied the heat conduction equation without boundary conditions. In this paragraph we show that any boundary condition problem can be reformulated as a problem with virtual heat sources and zero b.c. See Strikwerda (1989) for more details.

²This follows from the linearity properties of equation (3.1.9) on page 30

Let us consider the following problem:

$$\begin{cases} \partial_t T(\mathbf{x}, t) - D \nabla^2 T(\mathbf{x}, t) = 0, \\ T|_{\partial\Omega} = f(\mathbf{x}, t), \end{cases} \quad (3.2.14)$$

where $f(\mathbf{x}, t)$ is an arbitrary function. We solve this problem by expressing the solution via the stationary solution T_{st} , given by the following problem:

$$\begin{cases} \nabla^2 T_{\text{st}}(\mathbf{x}, t_0) = 0, \\ T_{\text{st}}|_{\partial\Omega} = f(\mathbf{x}, t_0), \end{cases} \quad (3.2.15)$$

where t_0 is arbitrary. This problem describes a configuration where the boundary condition at $\partial\Omega$ has been “frozen” at time t_0 and the system has had enough time to reach a stationary condition. Although T_{st} is a stationary solution, it obviously depends on the “freezing time” t_0 and we can consider it time-dependent: $T_{\text{st}}(\mathbf{x}, t) = T_{\text{st}}(\mathbf{x}, f(t))$.

We write the unknown solution $T(\mathbf{x}, t)$ of equation (3.2.14) as

$$T(\mathbf{x}, t) = T_{\text{st}}(\mathbf{x}, f(t)) + \theta(\mathbf{x}, t), \quad (3.2.16)$$

that is the sum of the stationary solution and of another function $\theta(\mathbf{x}, t)$ to be determined. Since $T|_{\partial\Omega} = f(\mathbf{x}, t)$ and $T_{\text{st}}|_{\partial\Omega} = f(\mathbf{x}, t)$, then $\theta|_{\partial\Omega} = 0$ everywhere. By replacing $T(\mathbf{x}, t)$ into equation (3.2.14), we get

$$\begin{cases} \partial_t \theta(\mathbf{x}, t) - D \nabla^2 \theta(\mathbf{x}, t) = -\partial_t T_{\text{st}}(\mathbf{x}, f(t)), \\ \theta|_{\partial\Omega} = 0. \end{cases} \quad (3.2.17)$$

Equation (3.2.17) describes a heat conduction problem with a “virtual” heat source expressed by the following equation:

$$\dot{q}_{\text{virt}}(\mathbf{x}, t) = -c\rho \partial_t T_{\text{st}}(\mathbf{x}, f(t)), \quad [\dot{q}_{\text{virt}}] = \text{erg/s/cm}^3. \quad (3.2.18)$$

From the “chained rule” it follows that

$$\partial_t T_{\text{st}}(\mathbf{x}, f(t)) = \partial_f T_{\text{st}}(\mathbf{x}, f(t)) f'(t). \quad (3.2.19)$$

Thus, $\dot{q}_{\text{virt}} \propto f'(t)$. This gives some hints about the nature of $\theta(\mathbf{x}, t)$: it considers the fact that the boundary condition $f(t)$ is not “frozen” at $t = t_0$ as we supposed when we derived T_{st} .

What we said in this section can easily be applied when using a boundary condition of the second kind as well, namely

$$T'|_{\partial\Omega} = g(\mathbf{x}, t) \quad (3.2.20)$$

or even a mixed boundary condition

$$T|_{\partial\Omega_1} = f(\mathbf{x}, t), \quad T'|_{\partial\Omega_2} = g(\mathbf{x}, t), \quad (3.2.21)$$

where $\partial\Omega_1 \cup \partial\Omega_2 = \partial\Omega$. This simplification will be widely used in next chapters.

3.2.3. Damping of Periodic Fluctuations. A problem of particular interest for our case, and in space applications in general, is the propagation of temperature oscillations through a body of given mass, thermal capacity and thermal conductivity. In PLANCK, for example, it is important to know how temperature fluctuations propagate through the satellite and instrument structures, so that the temperature variation at the detectors and the resulting systematic error can be predicted.

Fluctuation damping is a simple conductive phenomenon which can be derived mathematically from equation (3.1.9). The order of magnitude of the results reported here is the same of the results derived by more refined analytical models, as we shall see in next chapters.

For the sake of simplicity, we shall study equation (3.1.9) in the one-dimensional case. We choose to neglect \dot{q}_g , supposing the body is thermally passive. The Cauchy problem we are going to study is the following:

$$D \partial_{xx}^2 T = \partial_t T, \quad (3.2.22a)$$

$$T(0, t) = \sum_{n=-\infty}^{+\infty} g_n e^{2\pi i \nu n t}, \quad (3.2.22b)$$

with $[D] = \text{cm}^2/\text{s}$. The D term is called *thermal diffusivity coefficient*, and it is given by

$$D = \frac{k}{\rho c}, \quad (3.2.23)$$

where k is the thermal conductivity ($[k] = \text{erg/s/K/cm}$), c the specific heat ($[c] = \text{erg/K/g}$) and ρ the mass density ($[\rho] = \text{g/cm}^3$) of the body. Equation (3.2.22a) is the heat conduction equation, while equation (3.2.22b) is a boundary condition expanded in Fourier series. Expressing the temperature as a sum of oscillating terms is justified from the fact that fluctuation damping is a frequency-dependent phenomenon. Note that g_n can be a complex number ($|g_n|$ is the magnitude of the n -th fluctuation and $\arg g_n$ the phase shift).

Since the problem is a second order differential equation, an initial condition and two boundary conditions need to be given in order to get an unique solution. We provided only one b.c.; for the second one, it is common in literature to provide a condition on $\partial_x T(0, t)$ (heat flux near the thermal contact between two bodies) or $T(a, t)$ (temperature at the opposite end of the body), with $a \in R$ being the body length. In this case it is better not to specify this second b.c.; the free parameters will be removed later from the solution by using a physical argument.

We can write the unknown solution using Fourier series again:

$$T(x, t) = \sum_{n=-\infty}^{+\infty} \varphi_n(x) e^{2\pi i \nu n t}. \quad (3.2.24)$$

If we substitute equation (3.2.24) into (3.2.22a), we get

$$\sum_{n=-\infty}^{+\infty} \left(\varphi_n''(x) - \frac{2\pi i \nu n}{D} \varphi_n(x) \right) e^{2\pi i \nu n t} = 0. \quad (3.2.25)$$

This means that for $n = -\infty \cdots +\infty$ the following relations must be satisfied (with $g_n \in \mathbb{C}$):

$$\varphi_n''(x) = \frac{2\pi i \nu n}{D} \varphi_n(x), \quad (3.2.26a)$$

$$\varphi_n(0) = g_n. \quad (3.2.26b)$$

Because equation (3.2.26a) is of the form $f''(x) = \alpha f(x)$, then the solution will be a sinusoid or an exponential.

Let us write equation (3.2.26a) in the form

$$\varphi''(x) = i\gamma \varphi(x), \quad \gamma \in \mathbb{R}, \quad (3.2.27)$$

and look for solutions $\varphi(x) \propto \exp(\alpha + i\beta)$ with $\alpha, \beta \in \mathbb{R}$ to be determined. Under this hypothesis, the Cauchy problem is equivalent to the following algebraic system:

$$\begin{cases} \alpha^2 = \beta^2 \\ 2\alpha\beta = \gamma, \end{cases} \quad (3.2.28)$$

that is satisfied by the following solutions:

$$\begin{cases} \alpha = \beta = \pm \sqrt{\frac{\gamma}{2}} & \text{if } \gamma > 0, \\ \alpha = -\beta = \pm \sqrt{\frac{-\gamma}{2}} & \text{if } \gamma < 0, \end{cases} \quad (3.2.29)$$

which implies that equation (3.2.26a) is satisfied by

$$\varphi_n(x) = Ae^{z_n x} + Be^{-z_n x}, \quad (3.2.30)$$

with

$$\begin{aligned} z_n &= \sqrt{\frac{\pi \nu |n|}{D}} (1 + i \operatorname{sgn} n) = \\ &= k_n (1 + i \operatorname{sgn} n), \end{aligned} \quad (3.2.31)$$

if $k_n = (\pi \nu |n| / D)^{1/2}$ (z_n is a complex number).

Let us now determine the two constants A and B . Since $\varphi_n(x)$ goes to infinity if $x \rightarrow +\infty$ (because of the first term), the condition $A \neq 0$ is not physically acceptable: a passive conductive medium cannot induce a raise in the temperature fluctuation amplitude. The other constant B is determined by equation (3.2.22b) on the preceding page considering $B = g_n = \varphi_n(0)$.

Therefore we can rewrite φ_n as

$$\varphi_n(x) = g_n e^{-k_n x} \exp(-i \operatorname{sgn}(n) k_n x). \quad (3.2.32)$$

Equation (3.2.22a) on page 35 has the following solution:

$$T(x, t) = \sum_{n=-\infty}^{+\infty} g_n \exp(-k_n x) \exp\left(i(2\pi\nu n t - \operatorname{sgn}(n) k_n x)\right). \quad (3.2.33)$$

The result is that a generic fluctuation with frequency ν is damped by $\exp(-\sqrt{\pi\nu/D} x)$. Furthermore, since $k \propto \sqrt{\nu}$ we have that the greater the frequency, the more the fluctuation is damped. Finally, because $k \propto \sqrt{1/D}$, a twofold increase in frequency is equivalent to halving the diffusion coefficient: a great value of D weakens the damping. We can see here how the diffusion coefficient is related to the propagation speed of temperature fluctuations in the medium.

With these results we can estimate which is the “critical frequency” ν_{crit} of temperature fluctuations in the LFI reference loads (whose length is $a \sim 1$ cm), i.e. what is the frequency for which fluctuations are damped to 50% after having passed through the reference load. The analytical form of ν_{crit} can be evaluated by solving equation $\exp(-k(\nu_{\text{crit}}) a) = 50\%$. By using the values reported in table 3.1 for the physical parameters and letting $a = 1$ cm, we obtain the following solution:

$$\nu_{\text{crit}} = \frac{(\ln 2)^2 D}{\pi a^2} \approx 0.15 \frac{D}{a^2} \approx 0.007 \text{ Hz}. \quad (3.2.34)$$

	Value	Unit
c	9.6×10^4	erg/g/K
k	0.8×10^4	erg/s/cm/K
ρ	1.70	g cm ⁻³
D	4.90×10^{-2}	cm ² s ⁻¹

Table 3.1: Typical values for Eccosorb CR110 thermal constants.

We shall see in section 4.2.1 on page 55 that using a better physical model which takes care of other boundary conditions the result will be about six times greater.

§ 3.3 Analytical Solutions using the Eigenfunction Expansion (EE) Method

In the previous sections the heat equation was solved in a somewhat “abstract” world, where no boundary conditions were defined. Now we are going to build a more physical framework which will be used in next chapters to study the thermal behaviour of the LFI reference loads.

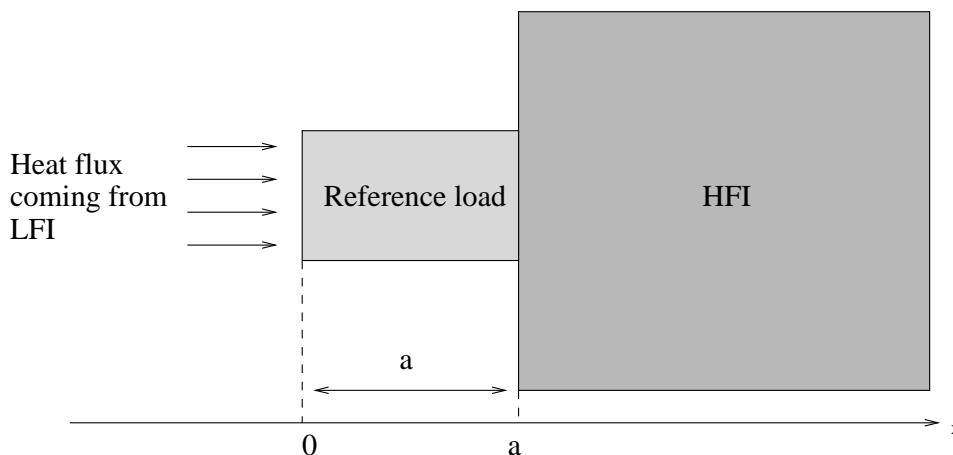


Figure 3.2: Configuration for the one-dimensional problem. A rod with large cross section (in order to make boundary effects negligible) is heated at $x = 0$ by a radiative source and is placed in thermal contact with a massive body at $x = a$.

In this section we shall use the Eigenfunction Expansion (EE) method to solve the heat equation. This method is used extensively in quantum mechanics problems (the Schrödinger equation is basically a diffusion equation with complex coefficients).

3.3.1. The One-Dimensional Solution. Let us consider the thermal behaviour of the reference load under the following simplifications:

1. The HFI shield is a *thermal tank*: it can exchange heat with the reference load without varying its temperature. This is justified by the fact that the HFI shield is much more massive than one reference load (several kilograms against ~ 10 g).
2. Boundary effects in the y and z directions (see figure 3.2) are negligible with respect to the x direction (i.e. only heat exchanges along the x direction are relevant).

With these assumptions, the reference load shown in **figure 3.2** can be considered unidimensional. The most natural boundary conditions which consider the presence both of HFI and LFI are:

1. a radiative heat flux at $x = 0$ coming from the LFI reference feed horn, described by a function $p(t)$ ($[p(t)] = \text{erg cm}^{-2} \text{s}^{-1}$); this places a boundary condition on the first space-derivative of T , as shown in Storck (1998);
2. a perfect thermal link with the HFI external shield at $x = a$, whose temperature is described by a function $T_a(t)$.

With these hypotheses, the heat conduction equation is of the form

$$T_t(x, t) - D T_{xx}(x, t) = 0, \quad (3.3.1a)$$

$$T_x(0, t) = -\frac{1}{k} p(t), \quad (3.3.1b)$$

$$T(a, t) = T_a(t), \quad (3.3.1c)$$

In order to solve equation (3.3.1a), we can change variables as explained in section 3.2.2. So we write the unknown solution as the sum of the “stationary” solution and of a new unknown function $\theta(x, t)$:

$$T(x, t) = \theta(x, t) + \underbrace{\frac{a-x}{k} p(t) + T_a(t)}_{\text{the stationary solution}}; \quad (3.3.2)$$

with $\theta(x, t)$ being an unknown function; then we have

$$\theta_t(x, t) - D \theta_{xx}(x, t) = r(x, t) \quad (3.3.3a)$$

$$\theta_x(0, t) = 0, \quad (3.3.3b)$$

$$\theta(a, t) = 0, \quad (3.3.3c)$$

with

$$r(x, t) = -\frac{a-x}{k} p'(t) - T_a'(t). \quad (3.3.4)$$

We stress again the fact that equation 3.3.3a describes how the difference between temperature $T(x, t)$ and the stationary solution $T_{\text{st}}(x)$ evolves in time.

The use of Green’s functions to solve this equation is not practical if we want a quantitative estimate of $T(x, t)$, because they are expressed in terms of generalized functions, which are difficult to approximate numerically.

An alternate method uses the Fourier series to solve equation (3.3.3a), by means of a so-called Eigenfunction Expansion (EE) of the solution (see Rauch 1991). This method uses implicitly the separation of variables, as Gustafson (1980) shows in Chapter 2.

Suppose we want to solve a partial differential equation of the form

$$u_t = Au + f \quad (3.3.5)$$

with f being an arbitrary function not dependent on u , and A being a linear differential operator on $\mathcal{L}^2([a, b])$ whose domain $\mathcal{D}(A)$ contains only those functions that satisfy the required boundary conditions. If A has a complete set of orthonormal eigenfunctions $\{e_n\}_{n=1}^{\infty}$ in $\mathcal{L}^2([a, b])$ — all of them satisfying the boundary conditions, since $e_n \in \mathcal{D}(A)$ for any n — then we can write $u(x, t)$ as

$$u(t) = \sum \varphi_n(t) e_n(x). \quad (3.3.6)$$

Substituting this expression into the equation leads to an ordinary differential equation in $\varphi_n(t)$. If the series in equation (3.3.6) converges uniformly for $t = 0$ (for which u reduces to the initial condition) then the series converges uniformly for any $t > 0$. From this follows that the general solution satisfies the boundary conditions (see Richtmyer 1978). In next chapters we shall use as initial condition $u(0) = 0$: in this way, any basis we choose the convergence will be always uniform.

Since we are studying heat conduction, we choose A as

$$\mathcal{D}(A) = \{u \in \mathcal{L}^2(\Omega) : u, u' \in \mathcal{C}_{\text{abs}}(\Omega), u'' \in \mathcal{L}^2(\Omega), u_x(0) = u_x(a) = 0\}, \quad (3.3.7)$$

$$A = \frac{1}{D} \nabla^2, \quad (3.3.8)$$

with $\Omega = [0, a]$. To solve equation (3.3.3a) on the page before, we need a complete set of orthonormal eigenfunctions for A . The following is the searched basis:

$$e_n(x) = \sqrt{\frac{2}{a}} \cos\left(\frac{\pi}{a} \left(n + \frac{1}{2}\right) x\right), \quad (3.3.9)$$

because it is of the form $\alpha \cos \beta x$ (eigenfunction for the second derivative operator) and satisfies equations (3.3.3b) and (3.3.3c). This set constitutes a basis for $\mathcal{L}^2([0, a])$. This fact can be justified by the Sturm-Liouville theory, as Kakaç and Yener (1985) show, but in appendix A on page 108 we offer a simpler proof that uses only some general facts about Hilbert spaces.

So, let us suppose our solution $\theta(x, t)$ can be written in the following way:

$$\theta(x, t) = \sum_{n=0}^{+\infty} \varphi_n(t) e_n(x), \quad (3.3.10)$$

where the series converges uniformly for $t = 0$.

If we consider equation (3.3.3a) on the page before, by using equation (3.3.10) we obtain

$$\sum_{n=0}^{+\infty} e_n(x) \left(\varphi_n'(t) + \frac{z_n^2 D \pi^2}{a^2} \varphi_n(t) \right) \stackrel{\text{a.e.}}{=} r(x, t) \stackrel{\text{a.e.}}{=} \sum_{n=0}^{+\infty} (r(\cdot, t)|e_n) e_n(x). \quad (3.3.11)$$

with

$$z_n = n + 1/2. \quad (3.3.12)$$

From the fact that $\{e_n\}_{n=0}^{\infty}$ is a set of linear independent functions, equation (3.3.11) is equivalent to the following set of equations (with $n = 0, \dots, \infty$):

$$\varphi_n'(t) + \frac{z_n^2 D \pi^2}{a^2} \varphi_n(t) = (r(\cdot, t)|e_n). \quad (3.3.13)$$

We evaluate $(r(\cdot, t)|e_n)$, the inner product in $\mathcal{L}^2([0, a])$, by using equation (3.3.4) on page 39:

$$\begin{aligned} (r(\cdot, t)|e_n) &= \int_0^a r(\xi, t) e_n(\xi) d\xi = \\ &= \int_0^a \left(\frac{a-x}{k} p'(t) + T'_L(t) \right) e_n(\xi) d\xi = \\ &= \frac{\sqrt{2} a a}{k \pi^2} \frac{p'(t)}{z_n^2} + \frac{\sqrt{2} a}{\pi} \frac{(-1)^n T'_L(t)}{z_n} \end{aligned} \quad (3.3.14)$$

By substituting this result into 3.3.3a, it follows that for each $n = 0 \cdots +\infty$

$$\varphi'_n(t) + \frac{1}{\tau_n} \varphi_n(t) + \frac{\sqrt{2} a a}{k \pi^2 z_n^2} p'(t) + \frac{(-1)^n \sqrt{2} a}{\pi z_n} T'_L(t) = 0, \quad (3.3.15)$$

where τ_n is defined by

$$\tau_n = \frac{a^2}{z_n^2 D \pi^2}, \quad (3.3.16)$$

and it is a “characteristic time” for the n -th component of our one-dimensional problem. After having solved equation (3.3.15) for every n , the solution for equation (3.3.1a) is

$$T(x, t) = \frac{a-x}{k} p(t) + T_a(t) + \sum_{n=0}^{+\infty} \varphi_n(t) e_n(x). \quad (3.3.17)$$

We now highlight some properties of equation (3.3.15).

1. By dividing equation (3.3.15) by $n^2 \pi^2/a^2$ and taking the limit $n \rightarrow +\infty$, we can prove that

$$\lim_{n \rightarrow +\infty} \varphi_n(t) = 0. \quad (3.3.18)$$

This result makes sense: $\varphi_n(t)$ goes into a series, and it must go to zero for $n \rightarrow +\infty$ (note that we did not make any assumption about $p(t)$ and $T_a(t)$, nor about initial conditions).

2. Equation (3.3.15) can be written as

$$\begin{cases} f'(t) &= \alpha f(t) + \zeta(t) \\ f(0) &= f_0 \end{cases} \quad (3.3.19)$$

which is satisfied by

$$f(t) = e^{\alpha t} \left(f_0 + \int_0^t e^{-\alpha \tau} \zeta(\tau) d\tau \right). \quad (3.3.20)$$

Thus, we have a direct formula to evaluate analytical solutions for equation (3.3.15).

3.3.2. The Two-Dimensional Solution. In the previous paragraphs we studied the heat conduction problem in the simplest case: a rod with length a , with a large section in order to avoid any boundary effect. Now we will increment the number of dimensions in order to consider effects coming from the rod boundaries.

Our 2-D model of a typical LFI reference load is shown in figure 3.3 on the next page: the reference load is surrounded by two aluminum walls, used to support the reference load; table 3.2 reports the physical constants for the aluminum.

	Value	Unit
c'	1.20×10^6	erg/s/cm/K
ρ'	2.71	g cm^{-3}
c'	3.88×10^3	erg/g/K
D'	1.14×10^2	$\text{cm}^2 \text{s}^{-1}$

Table 3.2: Thermal constants for aluminum (with solid crystalline structure), taken from Valenziano and Terenzi (2002).

Our interest lies in the reference load, not in the metallic walls: this will be the main source of radiation the LFI reference antenna will detect. So our coordinate system focuses on it: the metallic walls are considered to be part of the boundary conditions.

The system is composed by three thermally-coupled bodies: the reference load (made of Eccosorb) and two metallic walls. Each body reacts to temperature changes induced by the other two bodies and it itself influences them. Since heat propagates in the metallic walls $\sim 2 \times 10^3$ times faster than in the reference load (see the formula for characteristic time τ_n , equation (3.3.16) on the page before, and compare the values given in table 3.1 on page 37 with those in table 3.2), it is a good approximation to suppose that the thermal behaviour of the metallic walls can be considered independent of the presence of the reference load, and it can be considered a fixed boundary condition for the heat conduction problem. Obviously this is only an approximation, but we shall verify its validity with a numerical model which does consider thermal coupling.

Supposing the temperature profile of the two metallic walls is identical and its profile is given by $T_b(x, t)$, thermal conduction in the reference load

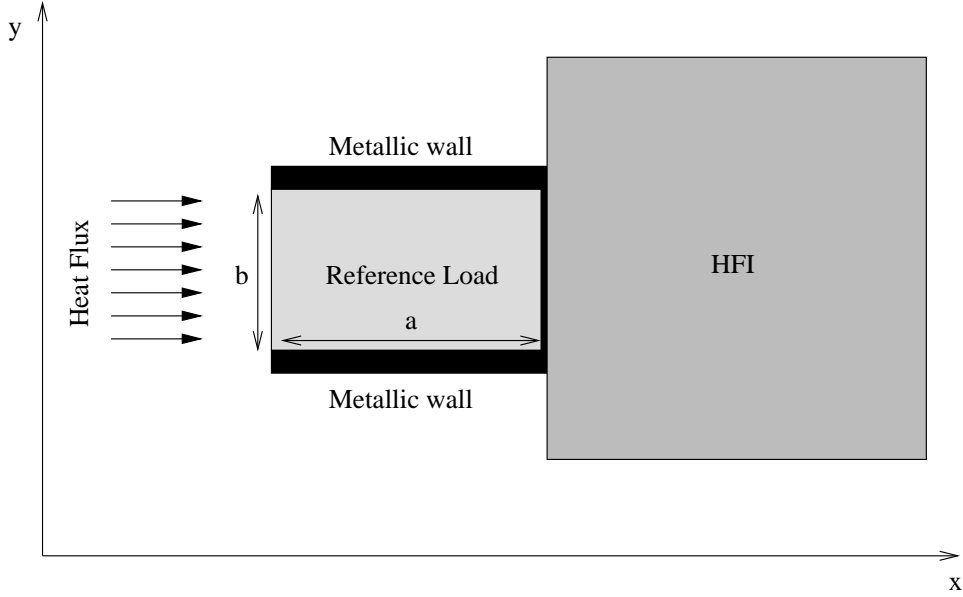


Figure 3.3: The 2-D problem geometry. The body under study is enclosed between two layers of some thermally conductive material, whose temperature distribution $T_b(x, t)$ is supposed to be known (the metallic layer at the HFI/RL interface is considered to be part of the HFI thermal mass). The role of the massive body and the origin of the heat flux are assumed to be the same as in the 1-D case.

can be described by the following PDE:

$$\partial_t T(x, y, t) = D \nabla^2 T(x, y, t), \quad (3.3.21a)$$

$$\partial_x T(0, y, t) = -\frac{p(t)}{k}, \quad (3.3.21b)$$

$$T(a, y, t) = T_a(t), \quad (3.3.21c)$$

$$T(x, 0, t) = T_b(x, t), \quad (3.3.21d)$$

$$T(x, b, t) = T_b(x, t). \quad (3.3.21e)$$

In the 1-D problem (see section 3.3.1 on page 38) the steady-state solution we used was

$$T(x) = T_0 + \frac{a-x}{k} p. \quad (3.3.22)$$

In a similar way, in order to solve equation (3.3.21) using the method developed in section 3.2.2, we must derive the solution for the following problem:

$$\partial_t T_{\text{st}}(x, y) = D \nabla^2 T_{\text{st}}(x, y, t), \quad (3.3.23a)$$

$$\partial_x T_{\text{st}}(0, y) = -\frac{p}{k}, \quad (3.3.23b)$$

$$T_{\text{st}}(a, y) = T_a, \quad (3.3.23c)$$

$$T_{\text{st}}(x, -b/2) = T_b(x), \quad (3.3.23d)$$

$$T_{\text{st}}(x, b/2) = T_b(x). \quad (3.3.23e)$$

(all the time-dependent boundary conditions are now constant). Recalling equation (3.2.13) on page 33, we can write $T_{\text{st}}(x, y)$ as

$$T_{\text{st}}(x, y) = \frac{a-x}{k} p + T_a + \hat{T}(x, y) \quad (3.3.24)$$

where $\hat{T}(x, y, t)$ is the solution of

$$\partial_t \hat{T}(x, y) = D \nabla^2 \hat{T}(x, y),$$

$$\partial_x \hat{T}(0, y) = 0,$$

$$\hat{T}(a, y) = 0,$$

$$\hat{T}(x, -b/2) = f(x) \equiv T_b(x) - \frac{a-x}{k} p - T_a,$$

$$\hat{T}(x, b/2) = f(x) \equiv T_b(x) - \frac{a-x}{k} p - T_a.$$

We do not supply the whole derivation of the result, as it can be found in Kakaç and Yener (1985):

$$T_{\text{st}}(x, y) = \frac{a-x}{k} p + T_a + \sum_{n=0}^{\infty} \frac{\cosh(\pi z_n y/a)}{\cosh(\frac{\pi}{2} z_n b/a)} (f|e_n) e_n(x), \quad (3.3.25)$$

where $z_n = n + 1/2$ as usual, and

$$e_n = \sqrt{\frac{2}{a}} \cos\left(\frac{\pi}{a} z_n x\right). \quad (3.3.26)$$

Note that the series goes to zero when $b \rightarrow \infty$, and $T_{\text{st}}(x, y)$ became the same as the one-dimensional steady solution.

A plot of $T_{\text{st}}(x, y)$ with the arbitrary choice $f(x) = x(x-a)$ is shown in figure 3.4 on the facing page.

With these tools we are able to solve equation (3.3.21) on the page before. Just let

$$T(x, y, t) = T_{\text{st}}(x, y, t) + \theta(x, y, t). \quad (3.3.27)$$

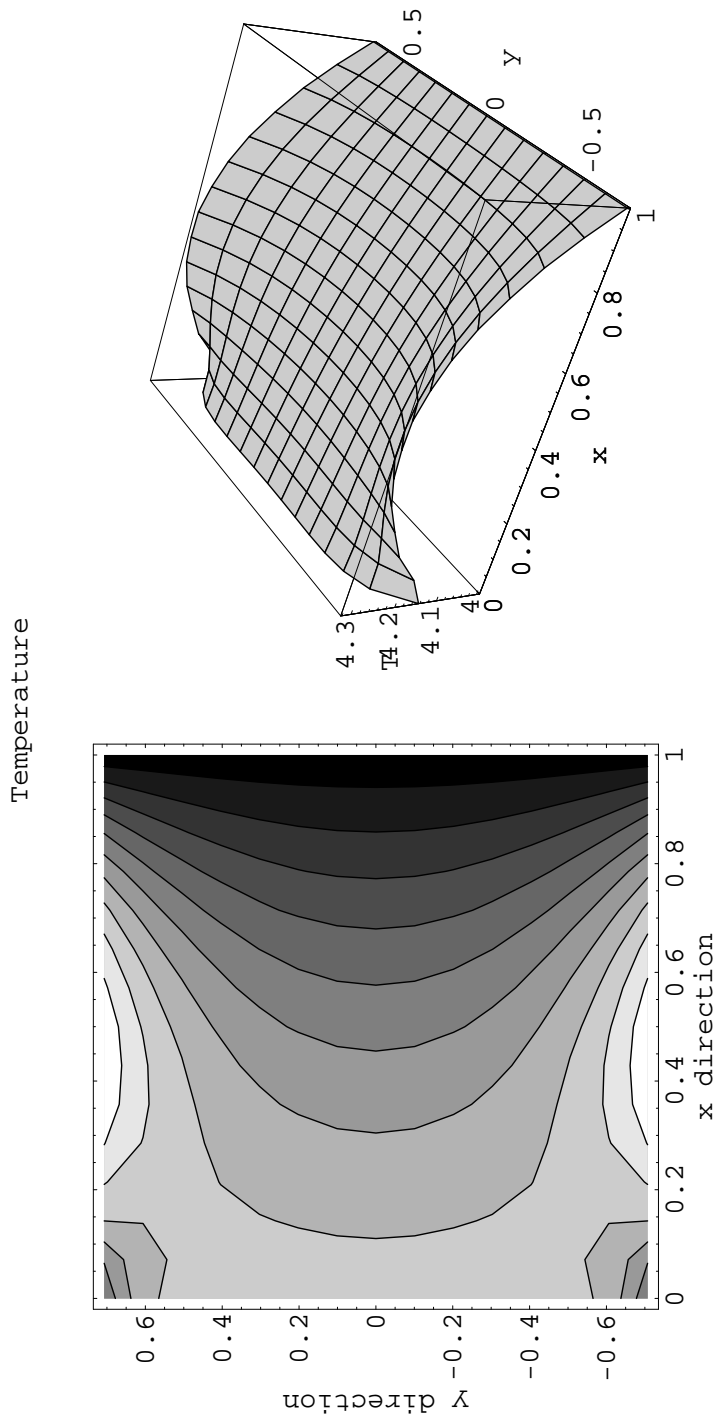


Figure 3.4: Temperature distribution on a 2-D rectangle with boundary conditions given as in equation (3.3.23) on the facing page. We chose $a = 1$, $b = \sqrt{2}$, $T_a = 4$, $p/k = 0.125$ and $T_b(x) = x(x - a)$ as boundary condition at $y = 0$ and $y = b$.

Then equation (3.3.21) on page 43 is equivalent to

$$\partial_t \theta(x, y, t) = D \nabla^2 \theta(x, y, t) - \partial_t T_{\text{st}}(x, y, t), \quad (3.3.28a)$$

$$\partial_x \theta(0, y, t) = 0, \quad (3.3.28b)$$

$$\theta(a, y, t) = 0, \quad (3.3.28c)$$

$$\theta(x, -b/2, t) = 0, \quad (3.3.28d)$$

$$\theta(x, b/2, t) = 0. \quad (3.3.28e)$$

To solve this problem, we let

$$e_n(x) = \sqrt{\frac{2}{a}} \cos\left(\frac{\pi}{a} z_n x\right),$$

$$h_m(y) = \sqrt{\frac{2}{b}} \cos\left(\frac{\pi}{b} (m+1)y + \frac{\pi}{2} m\right),$$

where e_n is the 1-D basis we used in section 3.3.1, while h_m is a new basis for the y direction which satisfies equations (3.3.28d) and (3.3.28e). We can express our solution $\theta(x, y, t)$ as

$$\theta(x, y, t) = \sum_{n=0}^{\infty} \sum_{m=0}^{\infty} \varrho_{nm}(t) e_n(x) h_m(y). \quad (3.3.29)$$

We need to know how to write $-\partial_t T_{\text{st}}(x, y, t)$ as a series in $e_n h_m$. Let's write $T_{\text{st}}(x, y, t)$ in a more compact form:

$$T_{\text{st}}(x, y, t) = \frac{a-x}{k} p(t) + T_a(t) + \sum_{n=0}^{\infty} \mu_n(y, t) e_n(x) \quad (3.3.30)$$

where μ_n is given by

$$\mu_n(y, t) = \frac{\cosh(\pi z_n y/a)}{\cosh(\frac{\pi}{2} z_n b/a)} (f(\cdot, t)|e_n) \quad (3.3.31)$$

By using equation (3.3.14) on page 41 we obtain

$$\begin{aligned} \partial_t T_{\text{st}}(x, y, t) &= \frac{a-x}{k} p'(t) + T'_a(t) + \sum_{n=0}^{\infty} \partial_t \mu_n(y, t) e_n(x) = \\ &= \sum_{n=0}^{\infty} \underbrace{\left(\frac{\sqrt{2} a a p'(t)}{k \pi^2 z_n^2} + \frac{(-1)^n \sqrt{2} a T'_a(t)}{\pi z_n} \right)}_{\equiv \eta_n(t)} + \partial_t \mu_n(y, t) e_n(x) = \\ &= \sum_{n=0}^{\infty} (\eta_n(t) + \partial_t \mu_n(y, t)) e_n(x). \end{aligned}$$

We must use a series representation not only in e_n , but in h_m as well (in other words, the dependence of $\partial_t T_{\text{st}}(x, y, t)$ on y must be expressed by means of the h_m basis). By using the properties of projectors in Hilbert spaces we get the following formulae:

$$1 = \sum_{m=0}^{\infty} \frac{\sqrt{2b}((-1)^m + 1)}{\pi(m+1)} h_m(y),$$

$$\frac{\cosh(\pi z_n y/a)}{\cosh(\frac{\pi}{2} z_n b/a)} = \sum_{m=0}^{\infty} \frac{\sqrt{2b}((-1)^m + 1)(m+1)}{\pi((m+1)^2 + (b/a)^2 z_n^2)} h_m(y).$$

As a result of our calculation, we get the following formula:

$$\partial_t T_{\text{st}}(x, y, t) = \sum_{n=0}^{\infty} \sum_{m=0}^{\infty} \zeta_{nm}(t) e_n(x) h_m(y), \quad (3.3.32)$$

where ζ_{nm} is defined by

$$\begin{aligned} \zeta_{nm}(t) = & \frac{\sqrt{2b}((-1)^m + 1)}{\pi(m+1)} \eta_n(t) + \\ & + \frac{\sqrt{2b}((-1)^m + 1)(m+1)}{\pi((m+1)^2 + (b/a)^2 z_n^2)} (\partial_t f(\cdot, t)|_{e_n}). \end{aligned} \quad (3.3.33)$$

Using this definition, we can rewrite equation (3.3.28) on the facing page as

$$\varrho'_{nm}(t) + \pi^2 D \left(\frac{z_n^2}{a^2} + \frac{(m+1)^2}{b^2} \right) \varrho_{nm}(t) + \zeta_{nm}(t) = 0, \quad (3.3.34)$$

which is our two-dimensional analogous for equation (3.3.15) on page 41 (one dimension). We note³ that if $b \rightarrow \infty$ then ζ_{nm} reduces to $\eta_n(t)$, which leads to the same equation as for the one-dimensional case. In equation (3.3.15) on page 41 the coefficient τ_n before φ_n was a “characteristic time”. In a similar way we can define

$$\tau_{nm} = \frac{1}{\pi^2 D} \left(\frac{z_n^2}{a^2} + \frac{(m+1)^2}{b^2} \right)^{-1} = \tau_n \left(1 + \frac{(m+1)^2}{z_n^2} \frac{a^2}{b^2} \right)^{-1}, \quad (3.3.35)$$

so our equation becomes

$$\varrho'_{nm}(t) + \frac{1}{\tau_{nm}} \varrho_{nm}(t) + \zeta_{nm}(t) = 0. \quad (3.3.36)$$

Note that $\tau_{nm} < \tau_n$ for any $n, m \geq 0$. Intuitively, this means that the heat conduction “speed” increases in the two-dimensional model, since there is

³Obviously, in the $b \rightarrow \infty$ approximation boundary conditions at the sides of the reference load have a negligible influence. This was the same hypothesis we did for the one-dimensional model, so obtaining the same result in this context is justified.

highly conductive material (the metallic walls) that helps heat transfer. In addition, $\lim_{b \rightarrow \infty} \tau_{nm} = \tau_n$, that is, when considering an infinitely large body, boundary effects disappear and we get back the one-dimensional characteristic time for the n -th component.

With equation (3.3.15) on page 41, each $\varphi_n(t)$ can be analytically evaluated using equation (3.3.20) on page 41. The complete solution is:

$$T(x, y, t) = \frac{a-x}{k} p(t) + T_a(t) + \sum_{n=0}^{\infty} \left(\mu_n(y, t) + \sum_{m=0}^{\infty} \varrho_{nm}(t) h_m(y) \right) e_n(x). \quad (3.3.37)$$

§ 3.4 Numerical Solutions

Analytical study of heat diffusion is impossible for most physical cases. When analytical formulae are of no use, the heat conduction equation can be studied using numerical algorithms. However, the analytical study is very important, since it can give us a tool to check the validity of numerical results for those cases which are analytically solvable. A lot of different methods to solve partial differential equations have been studied; we shall describe here the simplest.

3.4.1. The Finite Difference Method. To do a numerical study of equation (3.3.1a) on page 39, we discretize space and time in $n \times r$ intervals with a grid of $\Delta x \times \Delta t$. That is, instead of considering function $T(x, t)$ to be defined in each point of $[0, a] \times [0, +\infty)$, we suppose that T can be evaluated only at

$$w_i^j = T(x_i, t_j), \quad (3.4.1)$$

where $i = 1 \dots n$, $j = 1 \dots r$. The one-dimensional heat equation without heat sources would become

$$\frac{1}{D} \frac{w_i^{j+1} - w_i^j}{\Delta t} = \frac{w_{i+1}^j - 2w_i^j + w_{i-1}^j}{(\Delta x)^2}, \quad (3.4.2)$$

with a straightforward discretization of first and second derivatives. This solution is not the best one, as Strikwerda (1989) shows. It is strongly dependent on Δx and Δt , and if we choose bad values for these two quantities, it is unstable⁴. The error in equation (3.4.2) is

$$\epsilon = O(\Delta t) + O(\Delta x)^2. \quad (3.4.3)$$

⁴The numerical approximation of the solution of a PDE is said to be *unstable* if the rounding errors add up at every step of integration instead of balancing among themselves. See Strikwerda (1989) for a rigorous definition.

A more reliable method uses the Crank-Nicolson implicit discretization scheme. It uses the following formula:

$$\frac{1}{D} \frac{u_i^{j+1} - u_i^j}{\Delta t} = \frac{u_{i+1}^{j+1} - 2u_i^{j+1} + u_{i-1}^{j+1}}{2(\Delta x)^2} + \frac{u_{i+1}^j - 2u_i^j + u_{i-1}^j}{2(\Delta x)^2}. \quad (3.4.4)$$

The advantage of equation (3.4.4) over equation (3.4.2) is that the former gives solutions that are always stable. The error in equation (3.4.4) is $\epsilon = O(\Delta t)^2 + O(\Delta x)^2$.

If boundary conditions are given, such as $T_x(0, t) = p(t)$ e $T(a, t) = q(t)$, we could let

$$\frac{u_2^j - u_1^j}{\Delta t} = p(t_0 + (j - 1) \Delta t), \quad (3.4.5)$$

$$u_n^j = q(t_0 + (j - 1) \Delta t). \quad (3.4.6)$$

But equation (3.4.5) is only $O(\Delta x)$ accurate. If we plan to use a $O(\Delta x)^2$ method (like the Crank-Nicolson implicit scheme), we should better use a $O(\Delta x)^2$ formula, like the following⁵:

$$\frac{-3u_1^j + 4u_2^j - u_3^j}{2 \Delta x} = p(t_0 + (j - 1) \Delta t). \quad (3.4.8)$$

3.4.2. Matrix Formulation of the Finite Difference Formulae.

By using matrices, we can express equation (3.4.4) in a more compact way. Let $h = (\Delta x)^2/\Delta t$; we define matrices A and B as

$$A = \begin{pmatrix} 0 & 0 & 0 & 0 & \dots & 0 & 0 & 0 \\ 1 & -2(1 - h/D) & 1 & 0 & \dots & 0 & 0 & 0 \\ 0 & 1 & -2(1 - h/D) & 1 & \dots & 0 & 0 & 0 \\ \dots & \dots \\ 0 & 0 & 0 & 0 & \dots & 1 & -2(1 - h/D) & 1 \\ 0 & 0 & 0 & 0 & \dots & 0 & 0 & 0 \end{pmatrix} \quad (3.4.9)$$

⁵To get this formula, power series are used to expand

$$\alpha f(x) + \beta f(x + \Delta x) + \gamma f(x + 2\Delta x), \quad (3.4.7)$$

obtaining $p f(x) + q f'(x) \Delta x + r f''(x) (\Delta x)^2 + o(\Delta x)^2$ for some p, q and r . Then, letting $p = r = 0$ leads to a second-order approximation for $f'(x)$. This method can be used also to get third (and higher) order approximation, but it is useless if we plan to use the Crank-Nicolson formula (which is only second-order accurate).

$$\mathbf{B} = \begin{pmatrix} -1 & 4/3 & -1/3 & 0 & \dots & 0 & 0 & 0 \\ 1 & -2(1+h/D) & 1 & 0 & \dots & 0 & 0 & 0 \\ 0 & 1 & -2(1+h/D) & 1 & \dots & 0 & 0 & 0 \\ \dots & \dots \\ 0 & 0 & 0 & 0 & \dots & 1 & -2(1+h/D) & 1 \\ 0 & 0 & 0 & 0 & \dots & 0 & 0 & 1 \end{pmatrix} \quad (3.4.10)$$

$$\mathbf{s}^j = \left(\frac{2}{3} \Delta x p(t_0 + (j-1)\Delta t) \quad 0 \quad 0 \quad \dots \quad 0 \quad q(t_0 + (j-1)\Delta t) \right)^t \quad (3.4.11)$$

With these conditions, equation (3.4.4) and boundary conditions (3.4.8) and (3.4.6) are expressed by the following compact formula:

$$\mathbf{B} \mathbf{u}^{j+1} + \mathbf{A} \mathbf{u}^j = \mathbf{s}^{j+1}. \quad (3.4.12)$$

The solution, supposing that \mathbf{B} is invertible, is given by

$$\mathbf{u}^{j+1} = \mathbf{B}^{-1} \mathbf{s}^{j+1} - (\mathbf{B}^{-1} \mathbf{A}) \mathbf{u}^j. \quad (3.4.13)$$

Note that \mathbf{s} depends on j . This is because we have let boundary conditions to be dependent on time.

3.4.3. Implementation of a Simple FDM Solver. I wrote a simple C program to numerically integrate the diffusion equation in one dimension. The program is named `heat` and implements the formulas we got in section 3.4.2 on the preceding page.

The boundary conditions are:

1. A time-dependent flux of heat coming at $x = 0$.
2. A time-dependent temperature at $x = a$.

These are the same boundary conditions we studied in section 3.3 on page 37. A complete example of use is shown in appendix D on page 125.

CHAPTER 4

Analysis of Heat Conduction: Propagation of Thermal Fluctuations

In the previous chapter we obtained a set of equations that describe the conductive thermal behaviour of the LFI Reference Load (RL)s. In this chapter we will solve these equations considering three different boundary conditions:

1. Sudden temperature change in the HFI shield ($T_a(t)$ is a step function). By studying this problem we can estimate the order of magnitude of the characteristic time needed for a temperature perturbation to propagate through the RL.
2. Sinusoidal temperature fluctuation in the HFI shield ($T_a(t)$). This problem is used to study the ability of RLs to damp temperature fluctuations. Also, these calculations can be extended to a generic periodic T_a by means of the Fourier theorem.
3. Sinusoidal fluctuation in the heat flux coming from the LFI reference antenna ($p(t)$). This problem allows us to estimate the impact of the reference antenna radiative emission on the RL temperature stability.

In the next chapter we shall analyze the mathematical properties and physical implications of the solutions derived here.

§ 4.1 Propagation of a Boundary Temperature Step Change

Let us write a step change in temperature from T_0 to T_1 at $t = t_0$ as

$$T_a(t) = T_0 + (T_1 - T_0) \theta(t - t_0) \quad (4.1.1)$$

(where θ is the step function), that is, the HFI shield in $x = a$ undergoes an impulsive temperature change at $t = t_0$, from T_0 to T_1 . Then

$$T'_a(t) = (T_1 - T_0) \delta(t - t_0). \quad (4.1.2)$$

The heat flux coming from the LFI reference antenna is supposed to be zero, as well as the black-body radiation emitted by the RL itself (no radiative heat exchanges), so that we can write

$$p(t) = 0. \quad (4.1.3)$$

4.1.1. The One-Dimensional Solution. In this case equation (3.3.15) on page 41 can be written as

$$\varphi_n'(t) + \frac{1}{\tau_n} \varphi_n(t) + \frac{(-1)^n \sqrt{2a}}{\pi z_n} (T_1 - T_0) \delta(t - t_0) = 0, \quad (4.1.4)$$

which is satisfied by

$$\varphi_n(t) = \frac{\sqrt{2a} (-1)^{n+1}}{\pi z_n} \exp\left(-\frac{t - t_0}{\tau_n}\right) (T_1 - T_0) \theta(t - t_0) \quad (4.1.5)$$

if we take $\varphi_n(t_0) = 0$ as the initial condition, that is by assuming that the temperature in the RL is T_0 everywhere for $t < t_0$. This satisfies the requirement stated in section 3.3.1 on page 38 for using the Eigenfunction Expansion (EE) method: the $\sum \varphi_n(t) e_n(x)$ series must converge uniformly for $t = t_0$. For $t > t_0$ the temperature profile is given by equation (3.3.17) on page 41:

$$T(x, t) = T_1 - (T_1 - T_0) \frac{\sqrt{2a}}{\pi} \sum_{n=1}^{\infty} \frac{(-1)^n}{z_n} \exp\left(-\frac{t - t_0}{\tau_n}\right). \quad (4.1.6)$$

4.1.2. The Two-Dimensional Solution. If the heat flux $p(t)$ is zero, the relevant quantities used in section 3.3.2 on page 42 become:

$$f(x, t) = T_b(x, t) - T_a(t) \quad (4.1.7)$$

$$\partial_t f(x, t) = \partial_t T_b(x, t) - T_a'(t) \quad (4.1.8)$$

$$\eta_n(t) = \frac{(-1)^n \sqrt{2a} T_a'(t)}{\pi z_n} \quad (4.1.9)$$

If we consider a metallic wall as a one-dimensional finite rod which is not thermally influenced by the contact with the RL¹, then heat conduction in the wall can be described by the one-dimensional solution derived in section 4.1.1 (see section 3.3.1 on page 38). This fixes our boundary condition $T_b(x, t)$:

$$T_b(x, t) = \frac{a - x}{c'} p_0 + T_a(t) + \sum_{n=0}^{\infty} \varphi_n(t) e_n(x), \quad (4.1.10)$$

¹In the physical system considered here this approximation is physically meaningful because the thermal conductivity constant of the metallic walls is about 100 times greater than the t.c. of the RL.

with

$$\varphi_n(t) = \frac{\sqrt{2a}(-1)^{n+1}}{\pi z_n} (T_1 - T_0) \theta(t - t_0) \exp\left(-\frac{t - t_0}{\tau'_n}\right),$$

$$\tau'_n = \frac{a^2}{D' \pi^2 z_n^2}.$$

Since we are considering a metallic body, thermal conductivity c' and diffusive constant D' will be different from the c and D we used in section 4.1.1, with $D' \gg D$.

Relevant quantities are

$$f(x, t) = \left(\frac{1}{c'} - \frac{1}{c}\right) (a - x) p_0 + \sum_{n=0}^{\infty} \varphi_n(t) e_n(x),$$

$$(f(\cdot, t)|e_n) = \frac{\sqrt{2a^3}}{\pi^2 z_n^2} \left(\frac{1}{c'} - \frac{1}{c}\right) p_0 + \varphi_n(t),$$

$$(\partial_t f(x, t)|e_n(x)) = \varphi'_n(t),$$

$$\mu_n(y, t) = \frac{\cosh(\pi z_n y/a)}{\cosh(\frac{\pi}{2} z_n b/a)} (f(\cdot, t)|e_n),$$

$$\eta_n(t) = \frac{(-1)^n \sqrt{2a}}{\pi z_n} (T_1 - T_0) \delta(t - t_0),$$

$$\zeta_{nm}(t) = (T_1 - T_0) \left(r_{nm}(t)|_{t=t_0} \delta(t - t_0) + s_{nm} \frac{\theta(t - t_0)}{\tau'_n} \right).$$

where $r_{nm}(t)|_{t=t_0}$ is equal to

$$\begin{aligned} r_{nm}(t)|_{t=t_0} &= \\ &= \frac{2(-1)^n \sqrt{ab}}{\pi^2 z_n} \left(\frac{(-1)^m + 1}{m + 1} - \frac{((-1)^m + 1)(m + 1)}{(m + 1)^2 + (b/a)^2 z_n^2} \exp\left(-\frac{t - t_0}{\tau'_n}\right) \right) \Big|_{t=t_0} = \\ &= \frac{2(-1)^n \sqrt{ab}}{\pi^2 z_n} ((-1)^m + 1) \left(\frac{1}{m + 1} - \frac{m + 1}{(m + 1)^2 + (b/a)^2 z_n^2} \right), \end{aligned}$$

and s_{nm} is equal to

$$s_{nm} = \frac{2(-1)^n \sqrt{ab}}{\pi^2 z_n} \frac{(-1)^m + 1}{(m + 1)^2 + (b/a)^2 z_n^2}. \quad (4.1.11)$$

Note that we consider r_{nm} only for $t = t_0$ since it is multiplied by $\delta(t - t_0)$, so that we can assume r_{nm} to be time-independent².

²We would be not allowed to use this substitution if we needed to use $\zeta'_{nm}(t)$ or any higher derivative. But we use no $\zeta_{nm}(t)$ derivative when solving equation (3.3.36) on page 47.

The solution to equation (3.3.36) on page 47 is therefore

$$\begin{aligned} \varrho_{nm}(t) = & (T_1 - T_0) \theta(t - t_0) r_{nm} \exp\left(-\frac{t - t_0}{\tau_{nm}}\right) + \\ & + (T_1 - T_0) \theta(t - t_0) \frac{s_{nm}}{1 - \tau'_n/\tau_{nm}} \left(\exp\left(-\frac{t - t_0}{\tau_{nm}}\right) - \exp\left(-\frac{t - t_0}{\tau'_n}\right) \right), \end{aligned} \quad (4.1.12)$$

and the temperature profile is given by

$$\begin{aligned} T(x, y, t) = & \frac{a - x}{c} p_0 + T_0 + (T_1 - T_0) \theta(t - t_0) + \\ & + \sum_{n=0}^{\infty} \left(\mu_n(y, t) + \sum_{m=0}^{\infty} \varrho_{nm}(t) h_m(y) \right) e_n(x). \end{aligned} \quad (4.1.13)$$

4.1.3. Dependence of the Temperature Distribution from Physical Parameters. In many cases of practical interest it is useful to estimate the dependence of the temperature distribution on physical parameters like thermal conductivity, thermal capacity, etc. In this section we derive analytical relationships that allow to estimate the deviation δT on $T(x, t)$ starting from an uncertainty δD on thermal diffusivity D .

If we want to evaluate a generic function $f(x)$ where $x = \bar{x} \pm \delta x$ is a normally distributed parameter with standard deviation δx , then our estimate for $f(x)$ has an error equal to

$$\delta f = |f'(\bar{x})| \delta x. \quad (4.1.14)$$

In our case we want to know the error associated with T if the thermal mass linked to the rod undergoes a step temperature change. The ratio between the absolute error and the temperature change in the boundary condition is

$$\frac{\delta T(x, t)}{T_1 - T_0} = \text{err}_{T|D}(x, t) \frac{\delta D}{D}, \quad (4.1.15)$$

with

$$\text{err}_{T|D}(x, t) = \frac{\delta T(x, t)/\Delta T}{\delta D/D} = D \left| \frac{\partial_D T(x, t)}{T(x, t)} \right| \quad (4.1.16)$$

being the ratio between the temperature relative error and the relative error on D .

To evaluate the partial derivative, we use the following formulae:

$$\begin{aligned} \frac{\partial \tau_n}{\partial D} &= -\frac{\tau_n}{D}, \\ \frac{\partial \phi_n(t)}{\partial D} &= -\frac{\phi_n}{D} \frac{t}{\tau_n}, \end{aligned}$$

which lead us to the following relationship:

$$\text{err}_{T|D}(x, t) = \left| \frac{\sum \varphi_n(t) e_n(x) t/\tau_n}{T_1 - T_0} \right|. \quad (4.1.17)$$

§ 4.2 Propagation of Boundary Temperature Periodic Fluctuations

In this section we use our analytical models to study what happens when the temperature at the HFI/RL interface fluctuates in time. We start considering a sinusoidal fluctuation, and we then extend the result obtained to a generic periodic function using the Fourier theorem.

4.2.1. The One-Dimensional Solution. Let us suppose the temperature at $x = a$ changes in time according to the following law:

$$T_a(t) = T_0 + T_d \sin(2\pi\nu t) \quad (4.2.1)$$

while $p(t) = 0$ as in the previous section (no heat flow from the LFI reference antenna). Then the first derivative of $T_a(t)$ is

$$T'_a(t) = 2\pi\nu T_d \cos(2\pi\nu t), \quad (4.2.2)$$

and equation (3.3.15) on page 41 becomes

$$\varphi'_n(t) + \frac{1}{\tau_n} \varphi_n(t) + \frac{(-1)^n 2\sqrt{2a}\nu}{z_n} T_d \cos(2\pi\nu t) = 0. \quad (4.2.3)$$

If $T_a(t)$ is given by equation (4.2.1), the solution of equation (3.3.15) on page 41 is:

$$\begin{aligned} \varphi_n(t) = & (-1)^{n+1} \frac{\sqrt{2a} K_n(\nu) T_d}{\pi z_n (1 + K^2(\nu))} (\cos(2\pi\nu t) + K_n(\nu) \sin(2\pi\nu t)) + \\ & + Z_n \exp\left(-\frac{t}{\tau_n}\right), \end{aligned} \quad (4.2.4)$$

with

$$z_n = n + \frac{1}{2}, \quad K_n(\nu) = 2\pi\nu\tau_n \quad (4.2.5)$$

and Z_n being a “free” constant that depends on the initial condition; if we suppose that $\varphi_n(0) = 0$ (so that $T(x, 0) = T_0$ like in section 4.1.1) then we have that

$$Z_n = (-1)^n \frac{\sqrt{2a} K_n(\nu) T_d}{\pi z_n (1 + K_n^2(\nu))}. \quad (4.2.6)$$

Note that only the third term in equation (4.2.4) depends on the initial condition. This term is a time-decreasing exponential with τ_n as temporal constant. This means that for $t \gg \tau_n$ the solution is independent from the initial conditions because the periodic boundary condition prevails. If we suppose that $t \gg \tau_n$, then $\varphi_n(t) \approx \bar{\varphi}_n(t)$, with

$$\bar{\varphi}_n(t) = (-1)^{n+1} \frac{\sqrt{2a} K_n(\nu) T_d}{\pi z_n (1 + K^2(\nu))} (\cos(2\pi\nu t) + K(\nu) \sin(2\pi\nu t)). \quad (4.2.7)$$

This is the solution we shall consider from now on, supposing that the system is already in a periodic condition for $t \geq 0$. We shall use the symbol φ_n in place of $\bar{\varphi}_n$ to simplify the notation.

By using equation (3.3.17) on page 41 we obtain the complete solution:

$$T(x, t) = T_0 + T_d \sin(2\pi \nu t) + \sum_{n=0}^{+\infty} \varphi_n(t) e_n(x). \quad (4.2.8)$$

This can be rewritten as

$$\begin{aligned} T(x, t) = & T_0 + \\ & + T_d \left(\sum_{n=0}^{+\infty} c_n(\nu) e_n(x) \right) \cos(2\pi \nu t) \\ & + T_d \left(1 + \sum_{n=0}^{+\infty} s_n(\nu) e_n(x) \right) \sin(2\pi \nu t), \end{aligned} \quad (4.2.9)$$

with

$$c_n(\nu) = (-1)^{n+1} \frac{\sqrt{2a} K_n(\nu)}{\pi z_n (1 + K^2(\nu))}, \quad (4.2.10a)$$

$$s_n(\nu) = c_n(\nu) K_n(\nu). \quad (4.2.10b)$$

Since equation (4.2.9) is of the following form:

$$T_0 + A(x, \nu) \cos(2\pi \nu t) + B(x, \nu) \sin(2\pi \nu t), \quad (4.2.11)$$

it can be simplified by using the following variable change:

$$A(x, \nu) = T_d \gamma_T(x, \nu) \sin \psi_T(x, \nu), \quad (4.2.12a)$$

$$B(x, \nu) = T_d \gamma_T(x, \nu) \cos \psi_T(x, \nu), \quad (4.2.12b)$$

which leads to

$$T(x, \nu) = T_0 + T_d \gamma_T(x, \nu) \sin(2\pi \nu t + \psi_T(x, \nu)), \quad (4.2.13)$$

with $\gamma_T(x, \nu)$ and $\psi_T(x, \nu)$ being adimensional quantities. The solution in this form indicates that in each point x the temperature oscillates around T_0 (mean temperature at $x = a$) with an amplitude γ_T and a phase delay ψ_T , both dependent on x and ν . These two function are given by

$$\gamma_T(x, \nu) = \sqrt{\left(\sum_{n=0}^{+\infty} c_n(\nu) e_n(x) \right)^2 + \left(1 + \sum_{n=0}^{+\infty} s_n(\nu) e_n(x) \right)^2}, \quad (4.2.14)$$

$$\psi_T(x, \nu) = \arctan \frac{\sum_{n=0}^{+\infty} c_n(\nu) e_n(x)}{\left(1 + \sum_{n=0}^{+\infty} s_n(\nu) e_n(x) \right)^2}. \quad (4.2.15)$$

Note that the phase shift (given by ψ_T) does not depend on T_d , while the amplitude ($T_d \gamma$) is proportional to it: this is physically reasonable, and it follows from the linearity of equation (3.3.15) on page 41.

4.2.2. The Two-Dimensional Solution. Let us calculate the temperature distribution along the metallic wall placed at $y = -b/2$ and $y = b/2$ according to our 1-D model (as we did in section 4.1.2 on page 52). Then, we have that

$$T_b(x, t) = T_a(t) + \sum \varphi_n(t) e_n(x), \quad (4.2.16)$$

with $\varphi_n(t)$ given by equation (4.2.7):

$$\begin{aligned} \varphi_n(t) &= T_d \frac{(-1)^{n+1} \sqrt{2a} K'_n(\nu)}{\pi z_n (1 + (K'_n)^2(\nu))} (\cos(2\pi\nu t) + K'_n(\nu) \sin(2\pi\nu t)) = \\ &= T_d c'_n(\nu) \cos(2\pi\nu t) + T_d s'_n(\nu) \sin(2\pi\nu t), \end{aligned} \quad (4.2.17)$$

where

$$K'_n(\nu) = 2\pi\nu\tau'_n, \quad \tau'_n = \frac{a^2}{\pi^2 D' z_n}. \quad (4.2.18)$$

These boundary conditions lead to the following solution for equation (3.3.36) on page 47:

$$\begin{aligned} \varrho_{nm}(t) &= T_d r_{nm}(\nu) \left((\beta_{nm}(\nu) - K_{nm}(\nu) \alpha_{nm}(\nu)) \cos(2\pi\nu t) + \right. \\ &\quad \left. + (\alpha_{nm}(\nu) + K_{nm}(\nu) \beta_{nm}(\nu)) \sin(2\pi\nu t) \right), \end{aligned} \quad (4.2.19)$$

with

$$\begin{aligned} K_{nm}(\nu) &= 2\pi\nu\tau_{nm}, \\ r_{nm}(\nu) &= \frac{((-1)^m + 1) \sqrt{2b} K_{nm}(\nu)}{\pi (1 + K_{nm}^2(\nu))}, \\ \alpha_{nm}(\nu) &= \frac{m+1}{(m+1)^2 + (b/a)^2 z_n^2} c'_n(\nu), \\ \beta_{nm}(\nu) &= -\frac{m+1}{(m+1)^2 + (b/a)^2 z_n^2} s'_n(\nu) + \frac{(-1)^{n+1} \sqrt{2a}}{\pi (m+1) z_n}. \end{aligned}$$

The temperature T can be written as:

$$T(x, y, t) = T_0 + T_d \gamma(x, y, \nu) \sin(2\pi\nu t + \psi(x, y, \nu)). \quad (4.2.20)$$

where $\gamma(x, y, \nu)$ and $\psi(x, y, \nu)$ are given by

$$\begin{aligned} \gamma(x, y, \nu) &= \left(\left(\sum_n e_n(x) \left(\Phi_n(y) c'_n(\nu) + \sum_m h_m(y) A_{nm}(\nu) \right) \right)^2 + \right. \\ &\quad \left. + \left(1 + \sum_n e_n(x) \left(\Phi_n(y) s'_n(\nu) + \sum_m h_m(y) B_{nm}(\nu) \right) \right)^2 \right)^{1/2}. \end{aligned} \quad (4.2.21)$$

$$\psi(x, y, \nu) = \arctan \frac{\sum_{n=0}^{\infty} e_n(x) \left(\Phi_n(y) c'_n(\nu) + \sum_{m=0}^{\infty} h_m(y) A_{nm}(\nu) \right)}{1 + \sum_{n=0}^{\infty} e_n(x) \left(\Phi_n(y) s'_n(\nu) + \sum_{m=0}^{\infty} h_m(y) B_{nm}(\nu) \right)} \quad (4.2.22)$$

To simplify the expressions, we used the following definitions:

$$\begin{aligned} \Phi_n(y) &= \frac{\cosh(\pi z_n y/a)}{\cosh(\frac{\pi}{2} z_n b/a)}, \\ A_{nm}(\nu) &= r_{nm}(\nu) (\beta_{nm}(\nu) - K_{nm}(\nu) \alpha_{nm}(\nu)), \\ B_{nm}(\nu) &= r_{nm}(\nu) (\alpha_{nm}(\nu) + K_{nm}(\nu) \beta_{nm}(\nu)). \end{aligned}$$

The configuration used for the 2-D model is symmetric with respect to the y axis; it is physically reasonable to expect that the analytical solution will be symmetric as well, e.g. $T(x, y, t) = T(x, -y, t)$. This can be proven by noting that $\mu_n(y, t) = -\mu_n(-y, t)$ and $\varrho_{nm} \propto r_{nm}$, which is zero if m is odd. Since the inner series contains only even terms and h_{2m} is always even, then $\mu_n(y, t)$ is an even function. Then the whole $T(x, y, t)$ is even with respect to y , which is what we wanted.

This 2-D solution can be reduced to equation (4.1.6) on page 52 (the 1-D solution) in many ways (this gives of course a way to check the correctness of the calculations!). For instance, we can consider the case when $b \rightarrow +\infty$: this implies that the boundary effects induced by the metallic walls are more and more negligible. Note that if b is large then $\Phi_n(y) \rightarrow 0$, $\tau_{nm} \rightarrow \tau_n$, $\alpha_{nm}(\nu) \rightarrow 0$; this means that

$$\beta_{nm} \rightarrow \frac{(-1)^{n+1} \sqrt{2a}}{\pi(m+1)z_n}, \quad (4.2.23)$$

so that

$$T(x, y, t) \rightarrow T_0 + \sum_{n=0}^{\infty} e_n(x) \varphi_n(x, t), \quad (4.2.24)$$

which is the same as equation (4.1.6). The two-dimensional formula can be reduced to the one-dimensional one also by letting $D' = D$ (we do not show the calculations here).

4.2.3. Dependence of the Solution on Physical Parameters. Like in section 4.1.3 we shall derive an analytical relationship of the sensitivity of T on thermal diffusivity D . We shall use equation (4.1.14) on page 54 again to evaluate $\delta T_{\max}/(T_d \gamma(x, \nu))$, the ratio between the maximum absolute error in temperature and the temperature fluctuation amplitude. We speak about a *maximum* absolute error because δT is a time-fluctuating function

like T : instead of taking the value of δT , we prefer to consider the amplitude of this fluctuation.

By doing some calculations, we get the following formulae:

$$\begin{aligned}\frac{\partial c_n}{\partial D}(\nu) &= -\frac{c_n(\nu)}{D} \frac{1 - K_n^2(\nu)}{1 + K_n^2(\nu)}, \\ \frac{\partial s_n}{\partial D}(\nu) &= -\frac{s_n(\nu)}{D} \frac{2}{1 + K_n^2(\nu)},\end{aligned}$$

which we can use to evaluate the relative error (remember that $\gamma(x, \nu) = T_d \eta(x, \nu)$):

$$\frac{\delta T_{\max}}{\gamma(x, \nu)} = \frac{\delta D}{D} \times \text{err}_{T|D}(x, \nu), \quad (4.2.25)$$

where

$$\begin{aligned}\text{err}_{T|D}(x, \nu) &= \frac{1}{\eta(x, \nu)} \left(\left(\sum_{n=0}^{\infty} c_n(\nu) \frac{1 - K_n^2(\nu)}{1 + K_n^2(\nu)} e_n(x) \right)^2 + \right. \\ &\quad \left. + \left(\sum_{n=0}^{\infty} s_n(\nu) \frac{2}{1 + K_n^2(\nu)} e_n(x) \right)^2 \right)^{1/2}. \quad (4.2.26)\end{aligned}$$

§ 4.3 Propagation of Boundary Heat Flux Periodic Fluctuations

In this section we shall study what happens in the case of a sinusoidal fluctuation of the radiative heat flux coming from the LFI reference horn ($x = 0$). We choose not to develop the two-dimensional model in this case, since results of the one-dimensional analysis already show that the mean amplitude of heat flux fluctuations is ~ 100 times smaller than the amplitude of HFI temperature fluctuations.

4.3.1. The Analytical Solution. The boundary conditions are the following:

$$T_a(t) = T_0, \quad (4.3.1a)$$

$$p(t) = p_0 + p_d \sin(2\pi\nu t) \quad (4.3.1b)$$

(HFI temperature T_0 is constant while the heat flux coming from LFI oscillates around p_0).

Equation (3.3.15) on page 41 becomes

$$\varphi_n'(t) + \frac{1}{\tau_n} \varphi_n(t) + \frac{\sqrt{2} a}{c \pi^2 z_n^2} p'(t) = 0. \quad (4.3.2)$$

which is very similar to equation (4.2.3) on page 55. The stationary solution is

$$\varphi_n(t) = -p_d \frac{\sqrt{2} a^3 K_n(\nu)}{c \pi^2 z_n^2 (1 + K_n(\nu))} (\cos(2\pi\nu t) + K_n(\nu) \sin(2\pi\nu t)) \quad (4.3.3)$$

which has been evaluated using the same approximations used in equation (4.2.9) on page 56 (i.e. this solution is meant to be used if $t \gg \tau_n$ for any $n > 0$). The meaning of $p(\nu)$ and z_n remains the same as in equation (4.2.9) on page 56.

The formulae used in section 4.2.1 on page 55 can be used here (with some minor modification) if we replace equation (4.2.10a) and equation (4.2.10b) with the following definitions:

$$c_n(\nu) = -\frac{\sqrt{2a} K_n(\nu)}{\pi^2 z_n^2 (1 + K_n^2(\nu))}, \quad (4.3.4a)$$

$$s_n(\nu) = c_n(\nu) K_n(\nu). \quad (4.3.4b)$$

The complete solution is therefore

$$\begin{aligned} T(x, t) = & \frac{a-x}{c} p_0 + T_0 + \\ & + \frac{a}{c} p_d \left(\sum_{n=0}^{\infty} c_n(\nu) e_n(x) \right) \cos(2\pi\nu t) + \\ & + \frac{a}{c} p_d \left(1 - \frac{x}{a} + \sum_{n=0}^{\infty} s_n(\nu) e_n(x) \right) \sin(2\pi\nu t). \end{aligned} \quad (4.3.5)$$

which again can be written as

$$T(x, t) = \frac{a-x}{c} p_0 + T_0 + \frac{a}{c} p_d \gamma_f(x, \nu) \sin(2\pi\nu t + \psi_f(x, \nu)) \quad (4.3.6)$$

with

$$\gamma_f(x, \nu) = \sqrt{\left(\sum_{n=0}^{\infty} c_n(\nu) e_n(x) \right)^2 + \left(1 - \frac{x}{a} + \sum_{n=0}^{\infty} s_n(\nu) e_n(x) \right)^2} \quad (4.3.7a)$$

$$\psi_f(x, \nu) = \arctan \frac{\sum_{n=0}^{\infty} c_n(\nu) e_n(x)}{1 - x/a + \sum_{n=0}^{\infty} s_n(\nu) e_n(x)} \quad (4.3.7b)$$

§ 4.4 Combination of Temperature Fluctuations and Heat Flux Fluctuations

Assuming a temperature fluctuation at $x = a$ and a heat flux fluctuation at $x = 0$, the solution can be derived by noting that equation (3.3.15) on page 41 is linear. If we define the following matrix

$$\mathbf{A}_n = \begin{bmatrix} 1 & 0 \\ 0 & z_n^2 D \pi^2 / a^2 \end{bmatrix}, \quad (4.4.1)$$

then equation (3.3.15) can be written as

$$\mathbf{A}_n \cdot \begin{pmatrix} \varphi'_n \\ \varphi_n \end{pmatrix} = K T'_a(t) + Q p'(t). \quad (4.4.2)$$

4.4 Combination of Temperature Fluctuations and Heat Flux Fluctuations 61

Because the above equation is linear and the right term is a combination of functions $T'_a(t)$ and $p'(t)$, then we can split it into the following two equations:

$$\mathbf{A}_n \cdot \begin{pmatrix} \phi'_n \\ \phi_n \end{pmatrix} = K T'_a(t),$$

$$\mathbf{A}_n \cdot \begin{pmatrix} \psi'_n \\ \psi_n \end{pmatrix} = Q p'(t).$$

where

$$\phi_n + \psi_n = \varphi_n \quad (4.4.3)$$

$$\phi'_n + \psi'_n = \varphi'_n \quad (4.4.4)$$

which implies that the solution is the sum of the solutions of the following boundary condition problems:

1. Oscillating temperature

$$T_a(t) = T_0 + T_d \sin 2\pi\nu t \quad (4.4.5)$$

at $x = a$ and constant heat flux ($p'(t) = 0$) at $x = 0$.

2. Oscillating heat flux

$$p(t) = p_0 + p_d \sin(2\pi\nu t + \zeta) \quad (4.4.6)$$

at $x = 0$, with ζ constant in time, and constant temperature ($T'_a(t) = 0$) at $x = a$.

Using equation (4.2.9) and equation (4.3.5) we can write

$$\begin{aligned} T(x, t) = & \frac{a-x}{c} p(t) + T_a(t) + \\ & + T_d \eta_T(x, \nu) \sin(2\pi\nu t + \psi_T(x, \nu)) + \\ & + \frac{a}{c} p_d \eta_f(x, \nu) \sin(2\pi\nu t + \psi_f(x, \nu) + \theta). \end{aligned}$$

This can be rewritten as

$$T(x, t) = \frac{a-x}{c} p(t) + T_a(t) + \gamma(x, \nu) \sin(2\pi\nu t + \xi(x, \nu)) \quad (4.4.7)$$

if we let

$$\gamma(x, \nu) = \sqrt{(T_d \eta_T(x, \nu))^2 + \left(\frac{a^2}{c^2} p_d \eta_f(x, \nu)\right)^2 + 2T_d \frac{a}{c} p_d \eta_T(x, \nu) \eta_f(x, \nu) \cos \theta},$$

$$\xi(x, \nu) = \arctan \left(\frac{c T_d \eta_T(x, \nu)}{p_d a \eta_f(x, \nu)} \csc \theta + \cot \theta \right).$$

Remembering that $\eta_T(x, \nu) \leq 1$, $\eta_f(x, \nu) \leq 1$, we find that the fluctuation amplitude $\gamma(x, \nu)$ is such that

$$\left| T_d - \frac{a}{c} p_d \right| \leq \gamma(x, \nu) \leq T_d + \frac{a}{c} p_d. \quad (4.4.8)$$

CHAPTER 5

Results and Discussion

§ 5.1 Propagation of a Boundary Temperature Step Change

5.1.1. One-Dimensional Analysis. Let us recall the solution we achieved in section 4.1.1 on page 52:

$$T(x, t) = T_1 - (T_1 - T_0) \frac{\sqrt{2a}}{\pi} \sum_{n=1}^{\infty} \frac{(-1)^n}{z_n} \exp\left(-\frac{t - t_0}{\tau_n}\right). \quad (\rightarrow 4.1.6)$$

Each term in the series is a decreasing exponential with temporal constant equal to τ_n , which becomes smaller and smaller as n increases. Then, if $t \gg \tau_0$ only the first term will be important: the characteristic time t_{1-D}^* (which describes how quickly the system reacts to temperature changes) is such that

$$t_{1-D}^* \sim \tau_0 = \frac{a^2}{z_0^2 D \pi^2} \sim 8 \text{ s}, \quad (5.1.1)$$

if $a = 1 \text{ cm}$ and $D = 0.049 \text{ cm}^2/\text{s}$ (Eccosorb CR110) is taken from table 3.1 on page 37. A plot of the formula is given in **figure 5.1** on the facing page.

Plots of $T(x, t)$ are shown in **figure 5.2** on the next page (animation-like frames) and **5.3** (comparison between analytical model and numerical simulation). The numerical simulation was made with FElt (see appendix E on page 131) using the same boundary conditions, and shows a good agreement with our numerical model.

Figure 5.4 on page 65 shows plots of $T(x = 0, t)$ using different values of D . Note how the slope of the curve increases with D , consistently with the fact that the characteristic time t_{1-D}^* is inversely proportional to D .

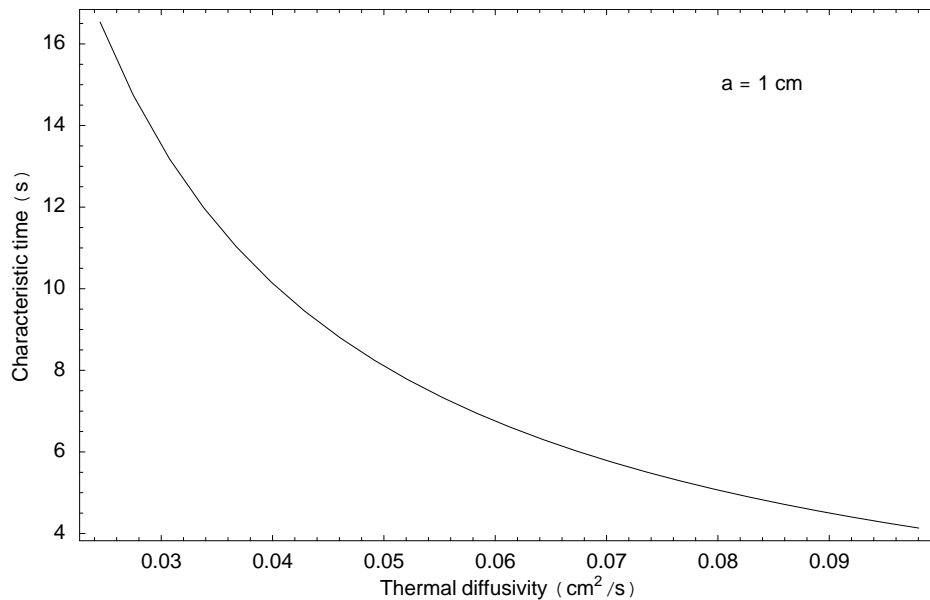


Figure 5.1: Dependence of the characteristic time t_{1-D}^* on the diffusivity constant D . The length of the RL is supposed to be $a = 1$ cm.

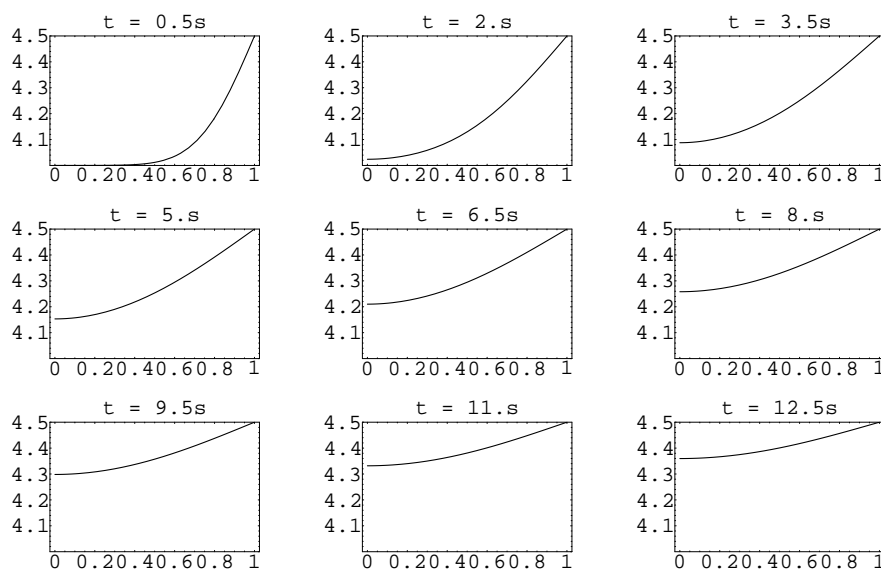


Figure 5.2: Temperature profile for a rod with a impulsive temperature change at $t = 0$ in $x = a$, from $T_0 = 4$ K to $T_1 = 4.5$ K. The x axis shows the position (in centimeters), while the y axis shows the temperature (Kelvin). $D = 0.049$ cm²/s is taken from table 3.1 on page 37.

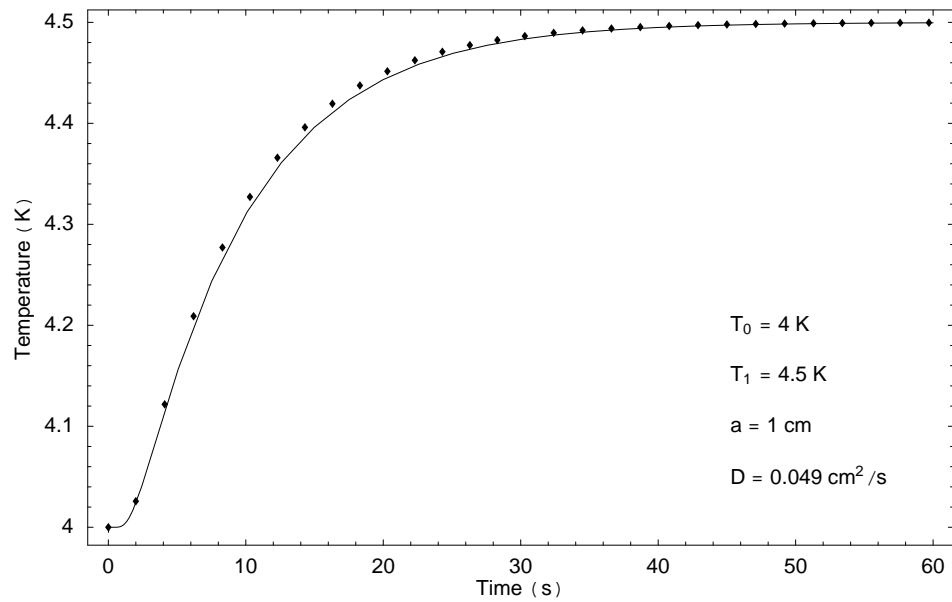


Figure 5.3: Temperature versus time at $x = 0$ for the same physical system of figure 5.2 on the page before. Constants are: $T_0 = 4 \text{ K}$, $T_1 = 4.5 \text{ K}$; the other physical parameters are taken from table 3.1 on page 37. The continuous line shows the analytical solution, while the dots show the result of a numerical simulation made with `heat` (see appendix D on page 125).

5.1.2. Two-Dimensional Analysis. The solution we achieved in section 4.1.2 on page 52 was

$$T(x, y, t) = \frac{a-x}{k} p_0 + T_0 + (T_1 - T_0) \theta(t - t_0) + \sum_{n=0}^{\infty} \left(\mu_n(y, t) + \sum_{m=0}^{\infty} \varrho_{nm}(t) h_m(y) \right) e_n(x), \quad (\rightarrow 4.1.13)$$

where $\mu_n(y, t)$, ϱ_{nm} and the other relevant quantities are defined in section 4.1.2.

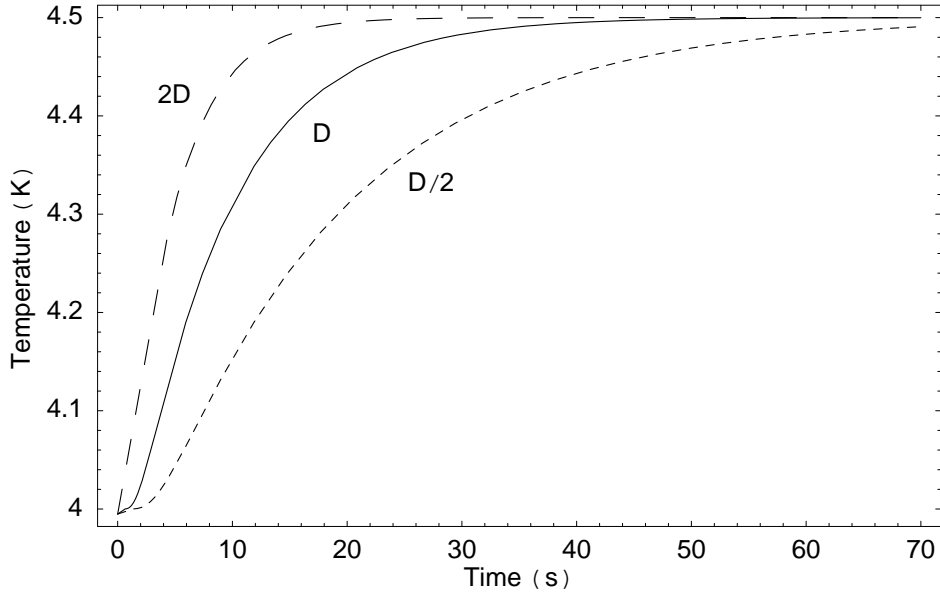


Figure 5.4: Temperature profile at $x = 0$ for three different values of thermal diffusivity: D (the same as in figure 5.3), $D/2$ (better insulator) and $2D$ (worse insulator). Other parameters are as in figure 5.3.

The 2-D model predicts a temperature variation at $x = 0$ which is faster than the 1-D model, because of the presence of metallic walls. We can suppose that the characteristic time t_{2-D}^* (which describes how quickly the system reacts to temperature changes, as in section 5.1.1) has the same order of magnitude of $\tau_{0,0}$, the time constant of the $n = 0, m = 0$ term in equation (4.1.13). In this case we have that

$$t_{2-D}^* \sim \tau_{0,0} = (\tau_0)_{1-D} \left(1 + 4 \frac{a^2}{b^2} \right)^{-1} \sim t_{1-D}^* \left(1 + 4 \frac{a^2}{b^2} \right)^{-1}. \quad (5.1.2)$$

Note that we expressed t_{2-D}^* as the product between t_{1-D}^* and a factor which depends on a^2/b^2 , a “geometrical” coefficient factor which vanishes if $b \rightarrow +\infty$. This means that, as one expects, the 2-D model gives the

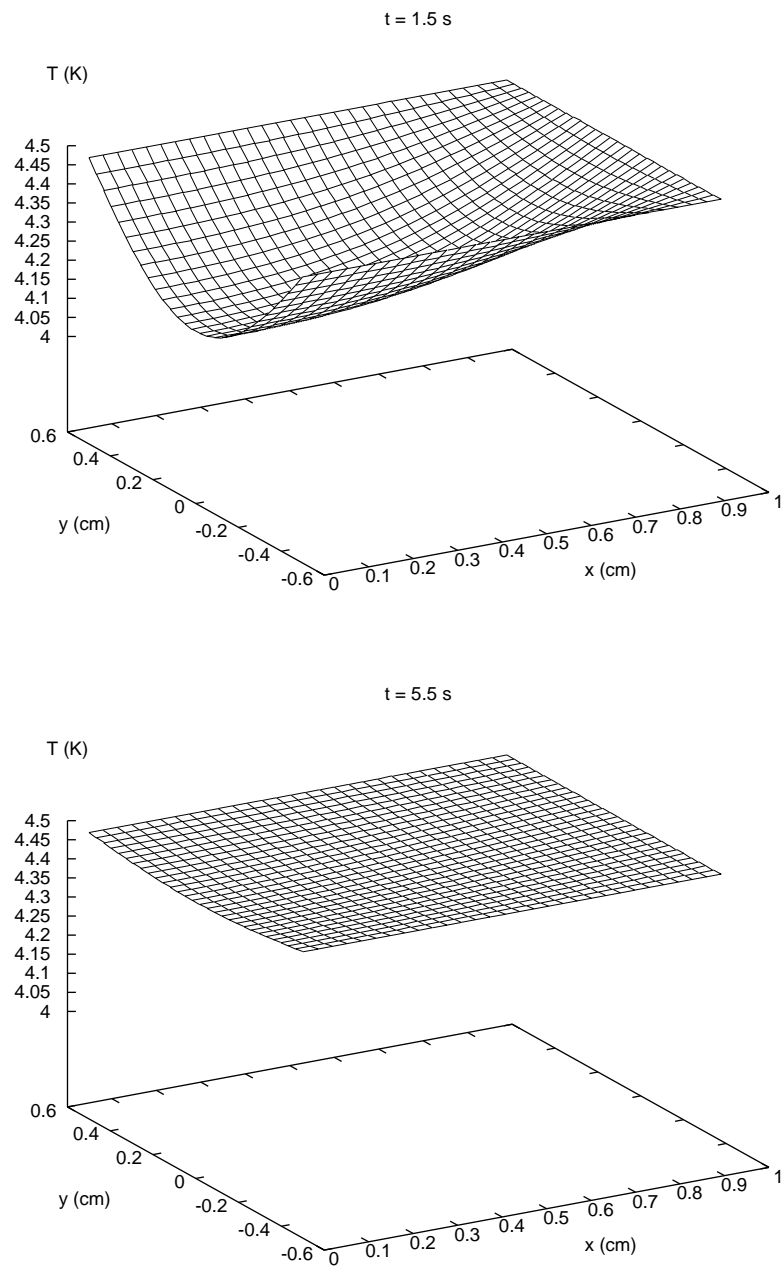


Figure 5.5: Two successive views of the temperature evolution in a rectangle. At the right side of the plot there is a sudden change in the temperature at time $t_0 = 0.5$ s, from 4.0 K to 4.5 K. The boundary conditions used are described in the text. The initial condition at $t = 0$ s is $T(x, y) = 4$ K everywhere. The constants used are $D = 0.049$ cm²/s, $D' = 114$ cm²/s, $a = 1.000$ cm, $b = 1.414$ cm.

Frequency (GHz)	a (cm)	b (cm)	a/b
30	1.967	3.333	0.59
44	1.500	2.274	0.66
70	1.129	1.429	0.79
100	0.940	1.000	0.94

Table 5.1: Values of the a/b ratio for the four shapes used in the LFI Reference Loads.

same predictions of the 1-D model when the metallic walls are removed or placed far from the centre: a reasonable behaviour. **Table 5.1** reports the a/b ratio for the four types of RL mounted on PLANCK; since these values have been provided some time after my study, I was not able to use them in the simulations. Instead, I assumed the RL to have a size of ($a = 1$ cm) \times ($b = \sqrt{2}$ cm = 1.414 cm) so that $a/b \sim 0.71$ (these values are not very different from the real values of the 70 GHz RL); using the values reported in table 5.1 would not change the order of magnitude of my results.

The temperature in the metallic walls was estimated using the 1-D model, thus neglecting the presence of the reference load. In other words, metallic walls are not influenced by the reference load, while the RL is influenced by them. To estimate the level of this approximation, I have built a simple 2-D model with FElt that considers this effect¹. I considered a 2-D Eccosorb plate surrounded on two edges by a layer of aluminum (like our analytical model) by means of a perfect thermal link between the walls and the Eccosorb. This link allows heat to be exchanged both from and to the metallic walls, thus modeling a real thermal coupling between the two materials. Results are shown in **figure 5.6** on the next page: a thickness of 1 mm in the two metallic walls gives a good agreement with the analytical model. Note also that a thickness of 0.1 mm leads to a slower temperature increase, as it should be: our analytical model does not consider this effect².

5.1.3. Sensitivity of the Temperature Distribution from Physical Parameters. The “error function” $\text{err}_{T|D}$ for a step temperature change at $x = a$ was derived in section 4.1.3 on page 54:

$$\text{err}_{T|D}(x, t) = \left| \frac{\sum \varphi_n(t) e_n(x) t / \tau_n}{T_1 - T_0} \right|. \quad (\rightarrow 4.1.17)$$

A plot of $\text{err}_{T|D}$ is shown in **figure 5.7** on the next page. Note that at the extremes ($t \rightarrow +\infty$, $t \rightarrow 0^+$) the temperature becomes insensitive to changes in D . This is because at both extremes the system is stationary and the equilibrium state does not depend on the diffusivity constant, which govern the transition the two states only. Also note that the peak at $t \sim 10$ s

¹A simplified version of the model is reported in section E.1 on page 131

²From a physical point of view, this model supposes that metallic walls have an infinite thickness, in order not to be influenced by the thermal behaviour of the body.

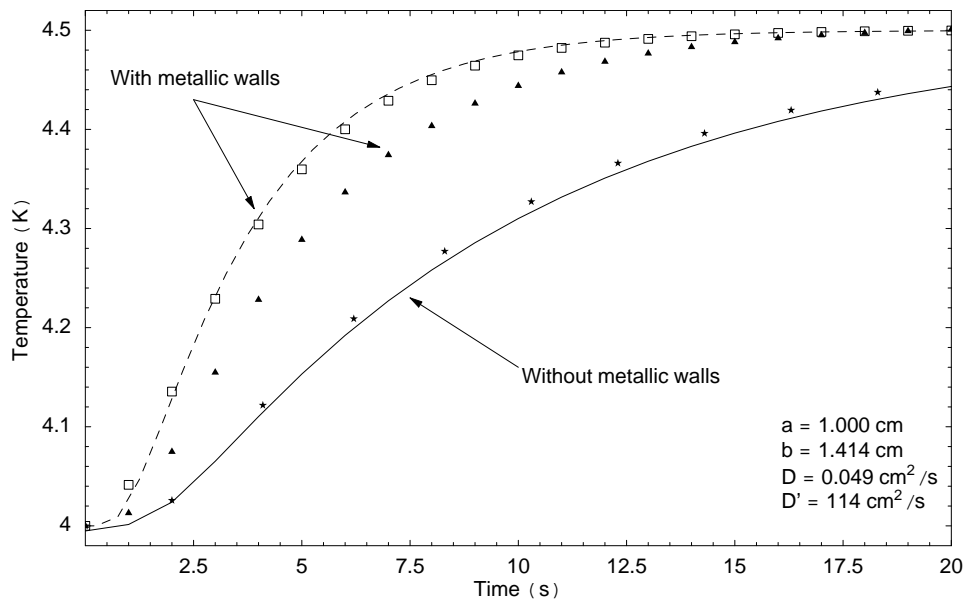


Figure 5.6: Temperature at $(x, y) = (0, 0)$ induced by a step temperature change from 4 K to 4.5 K at $x = a = 1 \text{ cm}$. The analytical models are shown by lines (continuous: 1-D model; dashed: 2-D model), numerical data by points (stars: 1-D model; triangles: 2-D model with 0.1 mm-thick walls; squares: 2-D model with 1 mm-thick walls).

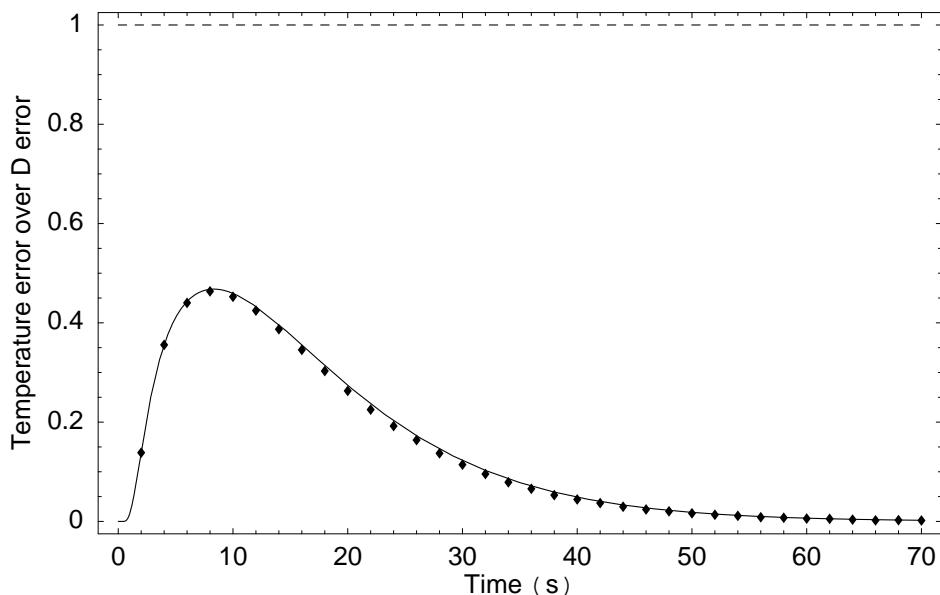


Figure 5.7: Relative sensitivity of T from D at $x = 0$. A value of 0.1 means that the relative error on T will be 10% of the relative error on D . Black dots show the result of a numerical simulation (see text).

is lower than 100%: if we make an error of 100% when determining D , then T has an error less than 50%.

The plot shows a set of black points calculated using the numerical model with two slightly different thermal diffusivities D and $D + \delta D$; the numerical estimate for $\text{err}_{T|D}(t)$ is given by

$$\text{err}_{T|D}(t) \approx \frac{T_D(x=0, t) - T_{D+\delta D}(x=0, t)}{(T_1 - T_0) \delta D}. \quad (5.1.3)$$

The agreement is extremely good.

§ 5.2 Propagation of Boundary Temperature Periodic Fluctuations

5.2.1. The One-Dimensional Model. The solution was derived in section 4.2.1 on page 55:

$$T(x, t) = T_0 + T_d \gamma_T(x, \nu) \sin(2\pi\nu t + \psi_T(x, \nu)). \quad (\rightarrow 4.2.13)$$

with $\gamma_T(x, \nu)$ and $\psi_T(x, \nu)$ being defined in equations (4.2.14) and (4.2.15).

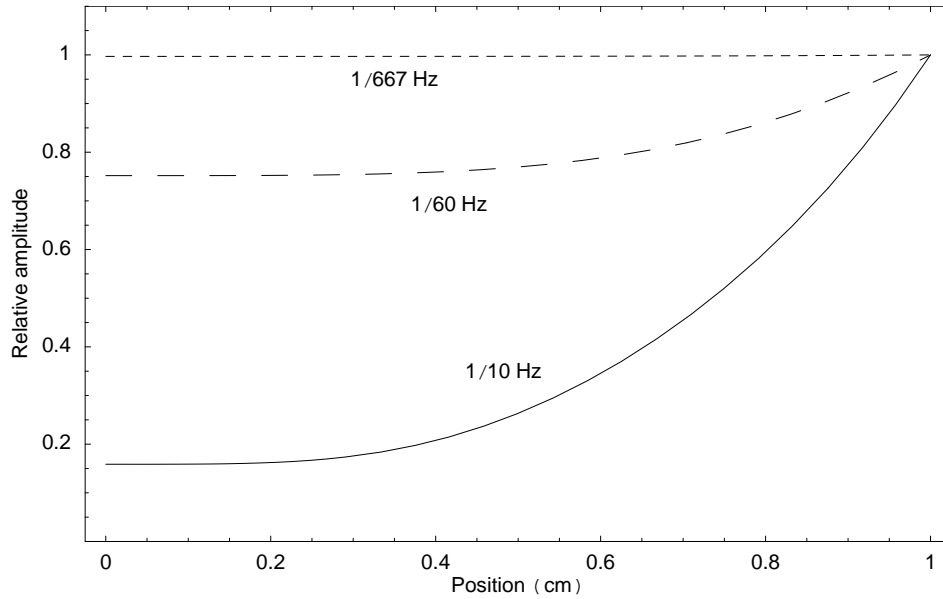


Figure 5.8: Temperature fluctuation amplitude (in relative units) versus position x in the body with $a = 1$ cm for three frequencies, considering a sinusoidal b.c. at $x = a$.

In section 3.2.3 on page 35 we found that the damping factor goes to zero if $\nu \rightarrow +\infty$. It is possible to derive the same result from equation (4.2.13): if $\nu \rightarrow \infty$, then $c_n \rightarrow 0$, $s_n \rightarrow (-1)^{n+1} \sqrt{2a}/\pi z_n$. By decomposing 1 into a series with $\{e_n\}_{n=0}^{\infty}$ as basis, it can be proved that

$$\sum_{n=0}^{\infty} \frac{(-1)^{n+1} \sqrt{2a}}{\pi z_n} e_n(x) \stackrel{\text{a.e.}}{=} -1, \quad (5.2.1)$$

so that

$$\begin{aligned} \lim_{\nu \rightarrow \infty} \gamma_T(x, \nu) &= \sqrt{\left(\sum_{n=0}^{+\infty} c_n(\nu) e_n(x) \right)^2 + \left(1 + \sum_{n=0}^{+\infty} s_n(\nu) e_n(x) \right)^2} \\ &= \sqrt{0 + (1 - 1)^2} = 0. \end{aligned} \quad (5.2.2)$$

This means that the higher the frequency, the better the Reference Load damps this fluctuation: the same result we derived in section 3.2.3 on page 35.

Since the reference load is used as a reference blackbody for the LFI radiometers, we are mainly interested in the temperature at the side facing the antenna ($x = 0$). The amplitude γ_T and phase ψ_T of the fluctuation at $x = 0$ is

$$\gamma_T(0, \nu) = \sqrt{\left(\sqrt{\frac{2}{a}} \sum_{n=0}^{+\infty} c_n(\nu) \right)^2 + \left(1 + \sqrt{\frac{2}{a}} \sum_{n=0}^{+\infty} s_n(\nu) \right)^2}, \quad (5.2.3)$$

$$\psi_T(0, \nu) = \arctan \frac{\sqrt{2/a} \sum_{n=0}^{+\infty} c_n(\nu)}{\left(1 + \sqrt{2/a} \sum_{n=0}^{+\infty} s_n(\nu) \right)^2}, \quad (5.2.4)$$

from the fact that $e_n(0) = \sqrt{2/a}$. The values of $\gamma_T(x = 0, \nu)$ at some frequencies that are most recurrent in the contest of PLANCK LFI are tabulated here for the thickness a of the LFI RLs:

a (cm)	1/4000 Hz	1/667 Hz	1/60 Hz
1.967 (30 GHz)	1.00	0.96	0.26
1.500 (44 GHz)	1.00	0.98	0.44
1.129 (70 GHz)	1.00	1.00	0.66
0.940 (100 GHz)	1.00	1.00	0.79

The frequencies included in this table are the same mentioned in chapter 2 on page 17: 4000s is the period required for the PLANCK sorption cooler to complete a whole cycle, while 667s is the period required for a single compressor bed. Finally, 60s is the spinning period of the spacecraft (see chapter 2 on page 17). From the tabulated values it seems that the reference load with the proposed length ($1 \div 3.3$ cm; see section 2.3 on page 21) does not damp the 1/4000 Hz and 1/667 Hz fluctuations, while 1/60 Hz fluctuations are damped at different levels according to the shape of the RL (better damping is obtained by the 30 Ghz RLs).

In section 3.2.3 on page 35 we estimated the “critical frequency” ν_{crit} for which temperature fluctuations coming from the HFI shield are reduced down to 50% of their original value by propagating through the reference loads. Here we repeat the derivation with the complete 1-D model by deriving an analytical form for the ν_{crit} frequency at $x = 0$ for which

$$\gamma_T(x = 0, \nu_{\text{crit}}) = 50\%. \quad (5.2.5)$$

To solve this equation we take advantage of the fact that if $\nu < 1/60$ Hz, then equation (4.2.14) can be approximated (with an accuracy of $\sim 97\%$) by taking only the $n = 0$ terms of the two series. The result is

$$\nu_{\text{crit}} = \frac{\pi^2 D}{8 a^2} \sqrt{\frac{3}{32\pi - 3\pi^2 - 64}} \approx 0.81 \frac{D}{a^2}. \quad (5.2.6)$$

For a rod made of Eccosorb with $a = 1$ cm, the estimation for the critical frequency is $\nu_{\text{crit}} \approx 0.04$ Hz. The result we found in section 3.2.3 without considering the boundary condition at $x = 0$ was $\nu_{\text{crit}} \approx 0.007$ Hz: this means that the presence of a boundary condition in the heat flux weakens the fluctuation damping (the greater ν_{crit} , the less fluctuations of a given frequency are damped) by ~ 6 times.

Plots of γ_T and ψ_T are shown in **figure 5.9** on the next page and **5.10**. Figure 5.9 shows a plot of $\gamma_T(x = 0, \nu)$ (continuous line) together with the results of a numerical simulation made under the same hypotheses (black dots). Figure 5.10 shows the time interval Δt_{del} between a temperature peak at $x = a$ (HFI side) and the corresponding peak at $x = 0$; it is given by

$$\Delta t_{\text{del}} = \frac{\psi(x = 0, \nu) - \psi(x = a, \nu)}{2\pi\nu} = \frac{\psi(x = 0, \nu)}{2\pi\nu}, \quad (5.2.7)$$

since from equation (4.2.1) on page 55 the phase shift ψ at $x = a$ is always zero.

Each data point in figure 5.9 and 5.10 was calculated from a single run of the numerical model with a temperature at $x = a$ given by equation (4.2.1). In order to extract the amplitude and the phase delay from each dataset, the following algorithms were used instead of a classical χ^2 -fit for speed reasons:

- To evaluate the fluctuation amplitude $\gamma_T(\nu)$, for each frequency plotted in figure 5.9 I ran a simulation lasting eight periods ($0 < t < 8/\nu$); after this time I discarded the first four periods (in order to ignore transient effects at the beginning of the simulation) and searched the maximum and minimum temperature T_{max} and T_{min} at $x = 0$. The value of γ_T is given by

$$\gamma_T \approx \frac{T_{\text{max}} - T_{\text{min}}}{2}. \quad (5.2.8)$$

- To evaluate the phase delay Δt_{del} , I discarded the first period³ and then searched for the first maximum in the data set; the phase delay

³I chose not to run the simulation for eight periods as in the case of the amplitude determination because in order to get a good precision (~ 0.1 s) in the delay reconstruction it is necessary to have a very little time step δt in the simulation. Running a simulation for the 1/4000 Hz frequency that lasts eight periods means to simulate $8 \times 4000 \text{ s} / 0.1 \text{ s} = 320,000$ steps. Apart from being a time-expensive process, numerical errors increase at every step thus making the additional effort useless.

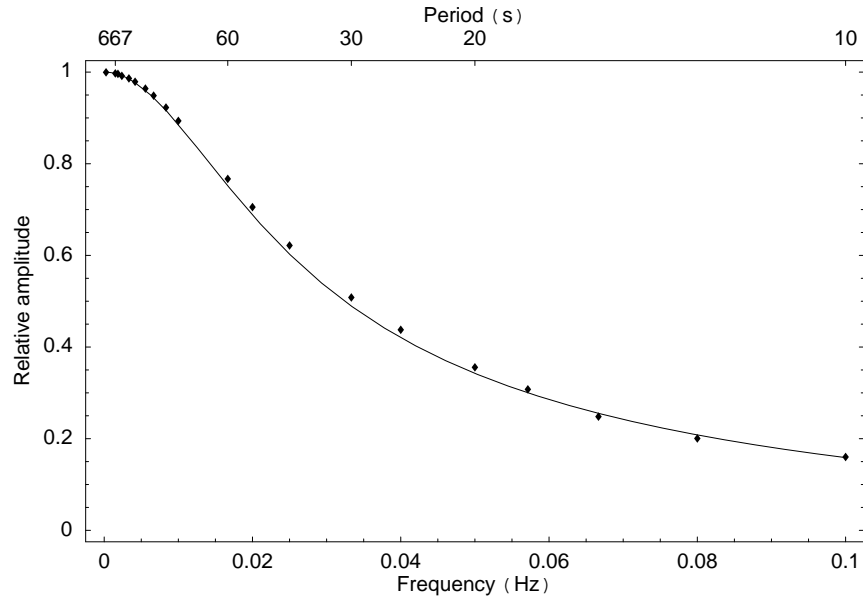


Figure 5.9: Plot of the relative amplitude γ_T versus frequency at $x = 0$ for a sinusoidal temperature fluctuation at $x = a$ ($a = 1$ cm). The dots show the result of a numerical simulation: the agreement is good.

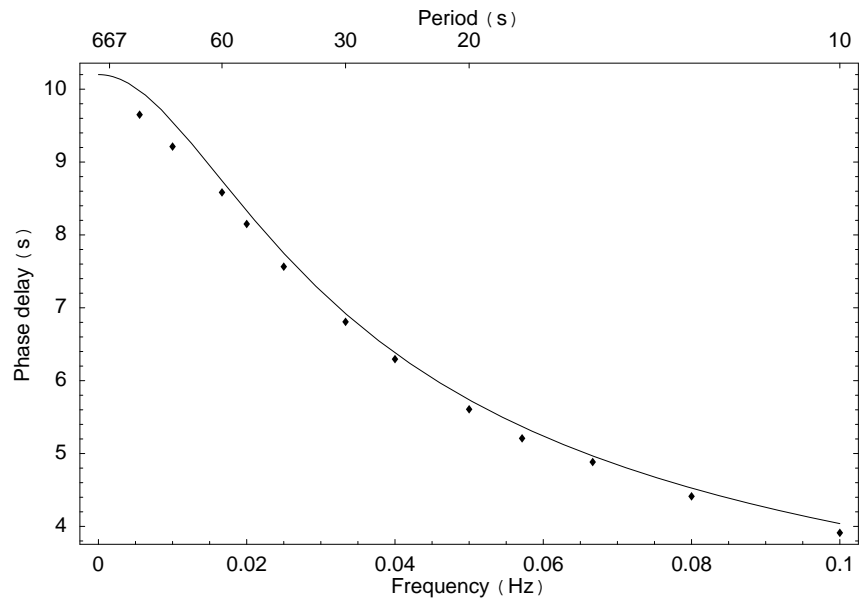


Figure 5.10: Peak retardation (in seconds) between $x = 0$ and $x = a$ for a sinusoidal temperature fluctuation at $x = a$, according to the 1-D model. This delay is equal to $|\psi(0, \nu) - \psi(a, \nu)| / (2\pi\nu)$, where $\psi(x, \nu)$ is the phase shift at x . The dots show the result of a numerical simulation: the agreement is good (the discrepancies are probably due to the numerical algorithm used to evaluate the points; see text).

is given by

$$\Delta t_{\text{del}} \approx \frac{1}{4\nu} - t_{\text{extr}}, \quad (5.2.9)$$

where t_{extr} is the time of the extremum and $1/4\nu$ is the time of the first maximum of equation (4.2.1).

5.2.2. The Two-Dimensional Model. The solution we obtained in section 4.2.2 on page 57 was

$$T(x, y, t) = T_0 + T_d \gamma(x, y, \nu) \sin(2\pi\nu t + \psi(x, y, \nu)). \quad (\rightarrow 4.2.20)$$

with $\gamma(x, y, \nu)$ and $\psi(x, y, \nu)$ being defined from equation (4.2.21) on page 57 and equation (4.2.22). Plots of these functions are shown in **figure 5.11** and **figure 5.12**. In figure 5.11 it is possible to see that the 2-D model predicts a smaller damping in temperature fluctuations. This is due to the metallic walls, as we said when commenting equation (3.3.35) on page 47.

The asymptotic behaviour of $\gamma(x, y, \nu)$ is identical to the one-dimensional case: the greater the frequency is, the better the body will damp the fluctuation. If $\nu \rightarrow 0$, then $c'_n(\nu) \rightarrow 0$, and so do $s'_n(\nu)$, $A_{nm}(\nu)$ and $B_{nm}(\nu)$. Then from equation (4.2.21) on page 57 follows that $\gamma(x, y, t) \rightarrow 1$, which means that slow fluctuations are not damped.

If $\nu \rightarrow \infty$, then $c'_n(\nu) \rightarrow 0$ but

$$s'_n(\nu) \rightarrow \frac{\sqrt{2a}}{\pi z_n}. \quad (5.2.10)$$

Since both $A_{nm}(\nu)$ and $B_{nm}(\nu)$ go to zero, we have that

$$\gamma(x, y, t) \sim \left| 1 + \sum_{n=0}^{\infty} e_n(x) \Phi_n(y) s'_n(\nu) \right| = 0 \quad \text{for } \nu \rightarrow \infty, \quad (5.2.11)$$

which means that fluctuations of great frequency are completely damped by the reference load.

5.2.3. Dependence of the Solution on Physical Parameters. The expression for $\text{err}_{T|D}(x, \nu)$ was derived in section 4.1.3 on page 54:

$$\text{err}_{T|D}(x, t) = D \left| \frac{\partial_D T(x, t)}{T(x, t)} \right| \quad (\rightarrow 4.1.16)$$

A plot of $\text{err}_{T|D}(x, \nu)$ is shown in **figure 5.14** on page 76 and **5.15**.

For the frequencies of interest (1/4000 Hz, 1/667 Hz and 1/60 Hz) the ratio between temperature error and diffusion error is always less than one: this means that the precision in determining temperatures is always greater at these frequencies than the precision obtained in the measure of D .

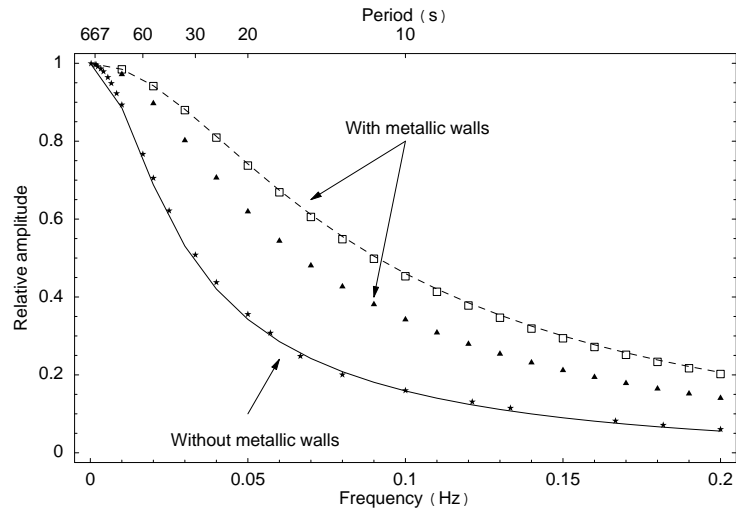


Figure 5.11: Relative amplitude at $(x, y) = (0, 0)$ for a sinusoidal temperature fluctuation at $x = b$. The physical size of the RL is supposed to be $(a = 1.000 \text{ cm}) \times (b = 1.414 \text{ cm})$. The triangle and square points are the result of two numerical simulation, supposing two different thicknesses for the metallic walls (squares: 1 mm, triangles: 0.1 mm). The continuous lines show the 2-D analytical solution (“With metallic walls”) and the 1-D solution (“Without metallic walls”). The stars are the result of a 1-D numerical simulation.

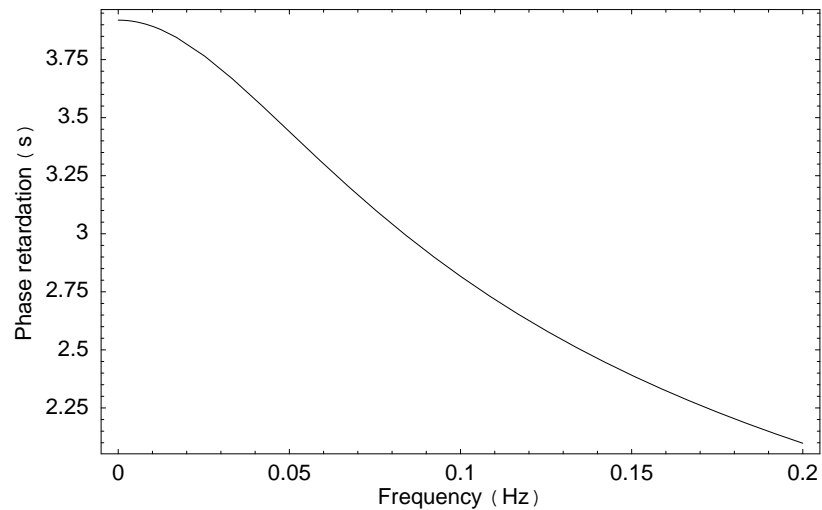


Figure 5.12: Peak retardation (in seconds) between $(x, y) = (0, 0)$ and $x = a$ for a sinusoidal temperature fluctuation at $x = a$, according to the 2-D model.

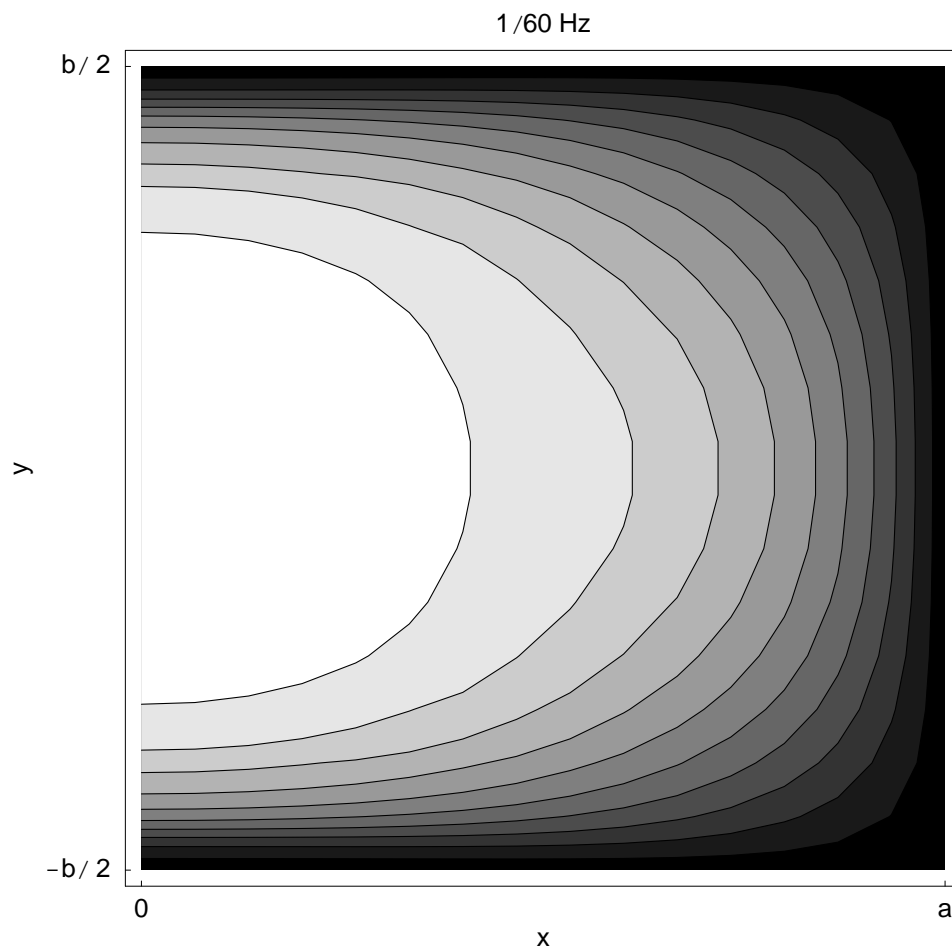


Figure 5.13: Contour plot of the relative amplitude of a fluctuation with frequency $1/60$ Hz in the reference load, according to the 2-D model. The darker the color is, the greater the amplitude is (white does not indicate a zero amplitude).

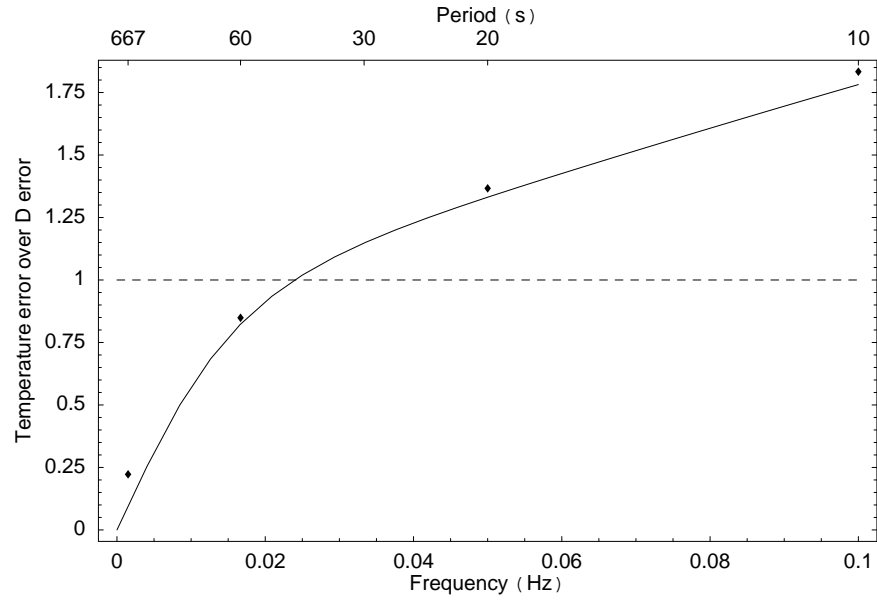


Figure 5.14: Frequency dependence of the relative error in temperature on the relative error in the D coefficient at $x = 0$. A value of 0.5 means that the relative error on T will be 50% of the relative error on D . The black points show the result of a numerical simulation, and agree reasonably well with our analytical model.

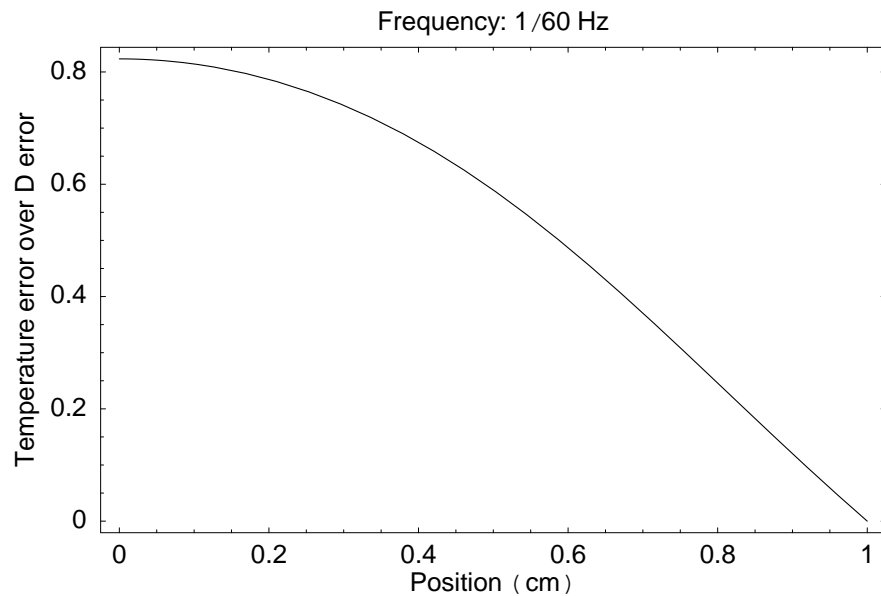


Figure 5.15: Dependence of the relative error in temperature on the relative error in the D coefficient for $\nu = 1/60$ Hz. The body length is supposed to be 1 cm, so the plot shows a full view.

5.2.4. Example of the application of 1-D models to a temperature fluctuation with complex shape. In this section we shall use the `heat` computer program (see appendix D on page 125) to perform a numerical realization of equation (4.2.14) on page 56 using a boundary condition on the temperature and comparing the estimation of the analytical formula with the results of the program.

We need a set of data which has some periodicity (in order to use a Fourier decomposition) and a complex shape (in order to perform a full test of the model). From this point of view the most natural choice would be a simulated temperature profile of the interface between the HFI external shield and the reference loads, which considers any thermal effect in the whole cryogenic chain of PLANCK. These data are not available yet for the contribution of the 4 K cooler, so we decided to use a dataset evaluated at the Jet Propulsion Laboratory (Pasadena, CA) for the profile of temperature at the interface of the instrument with the 20 K sorption cooler. As mentioned, this fluctuation will indeed contribute to the fluctuation at the HFI/RL interface through its propagation in the instrument mechanical structure.

Figure 5.16 on page 79 is a plot of the supposed temperature fluctuations on the HFI shield. The data file containing the set of samples shown in figure 5.16 has been used as input to `heat`, which simulated the heat conduction process in the body and output the temperature profile at the $x = 0$ side of the reference load (the side facing the LFI reference antenna). The first 2000 temperature samples in the output (corresponding to the first 2000 s of simulation time) were not included in the analysis in order to discard transient effects.

A plot of the samples output by `heat` is shown in figure 5.17. The highest frequencies have been removed by the fluctuation temperature, but the lower frequencies are still present.

A spectrum plot of the two fluctuations has been drawn in the same plot (the “input” temperature fluctuation and the simulated fluctuation at $x = 0$): see figure 5.18 on page 80. This spectrum was evaluated by applying the Discrete Fourier Transform (DFT) on the input data. Figure 5.19 compares the result of the numerical simulation with the prediction of the analytical formula for $\gamma_T(x = 0, \nu)$ (equation (4.2.14) on page 56). Some properties of these plots are discussed here:

- According to figure 5.18, low frequency fluctuations are transmitted through the Reference Load without damping: the gray line (the simulated fluctuation at $x = 0$) is exactly superimposed to the black line (the spectral plot of the HFI temperature fluctuation).
- In the same plot, higher frequencies are damped by thermal conduction. This is evident for $\nu \gtrsim 0.03$ Hz.
- For $\nu \sim 1$ Hz, fluctuations are less damped in the numerical simulation

than in the analytical prediction (figure 5.19). There are two possible explanations for this behaviour. This could be due to the so-called *aliasing effect* of the DFT. This is due to the discrete nature of the DFT. We quote Press et al. (1992) for a clear explanation of this effect:

“The bad news concerns the effect of sampling a continuous function that is *not* bandwidth limited to less than the Nyquist critical frequency. In that case, it turns out that all of the power spectral density that lies outside of the frequency range $-f_c < f < f_c$ is spuriously moved into that range. This phenomenon is called *aliasing*. Any frequency component outside of the frequency range $(-f_c, f_c)$ is *aliased* (falsely translated) into that range by the very act of discrete sampling. You can readily convince yourself that two waves $\exp(2\pi i f_1 t)$ and $\exp(2\pi i f_2 t)$ give the same samples at an interval Δ if and only if f_1 and f_2 differ by a multiple of $1/\Delta$, which is just the width in frequency of the range $(-f_c, f_c)$.” (page 501)

There is another possible explanation that is related again to the discrete nature of the DFT. The greater frequencies of the fluctuation spectrum ($\nu \sim 1$ Hz) are very close to the frequency used to sample the HFI temperature (1 sample per second). Numerical errors are likely to be more important near this frequency than for lower values of ν .

- A proof of the last statement is in the fact that for $\nu \rightarrow 1$ Hz there is more noise in the spectrum of the numerical samples (compare with the spectrum of the HFI temperature, which is quite narrow even for $\nu \sim 1$ Hz). This of course indicates that numerical errors got into the evaluation of the result.

We shall check if the numerical result matches our analytical formulae. In particular, we are going to consider equation (4.2.14) on page 56 (remember that this equation gives the relative amplitude for a sinusoidal temperature fluctuation with frequency ν), applying the formula to each spectral component shown in figure 5.18. Figure 5.19 shows the spectrum for the data plotted in figure 5.17. This is superimposed with $\gamma(\nu)$ in order to show the good agreement between the numerical and the numerical model; the only visible discrepancy is for $\nu \sim 1$ Hz, but we already said that numerical data are probably not reliable near these “critical” frequencies.

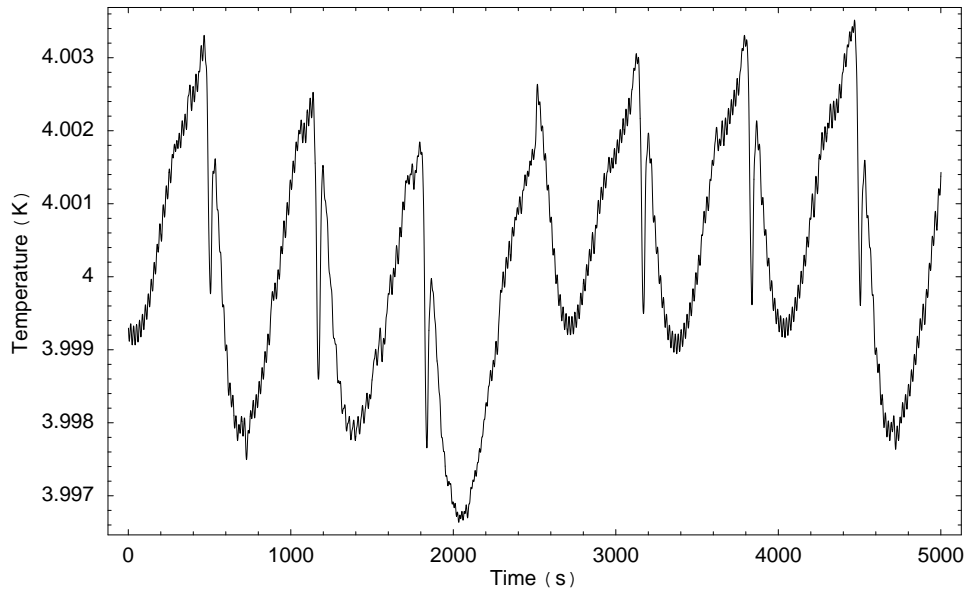


Figure 5.16: Temperature at the HFI side of the reference load ($x = a$). This set of samples is the result of a simulation made at the JPL, and it shows the temperature fluctuations in the sorption coolers. We imagine this to be the same in the HFI belt to whom the reference loads are linked.

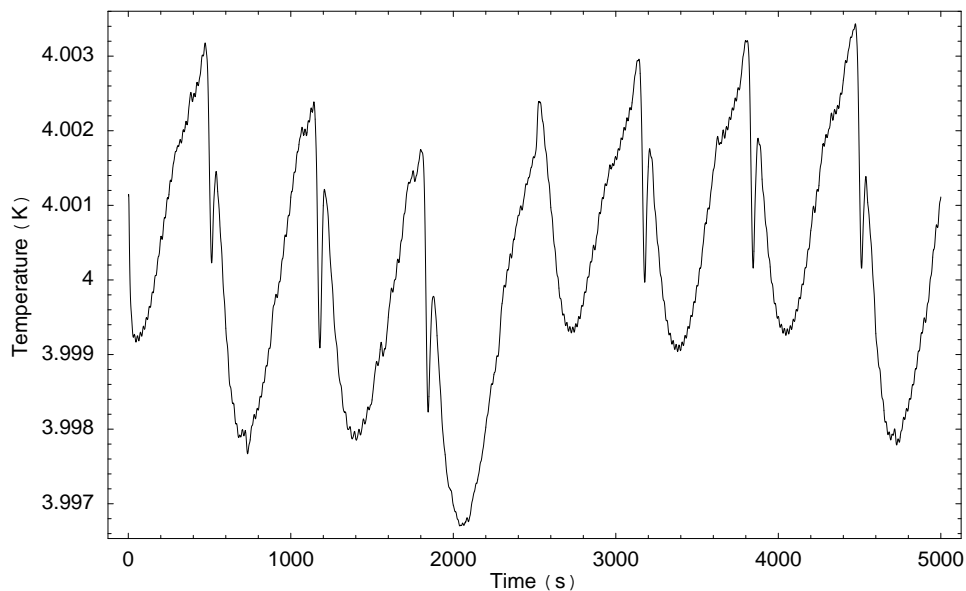


Figure 5.17: Temperature at the radiometer side of the reference load ($x = 0$) induced by a thermal fluctuation at $x = a$ (see figure 5.16). The samples are calculated by the `heat` program supposing a purely conductive heat conduction in the reference load.

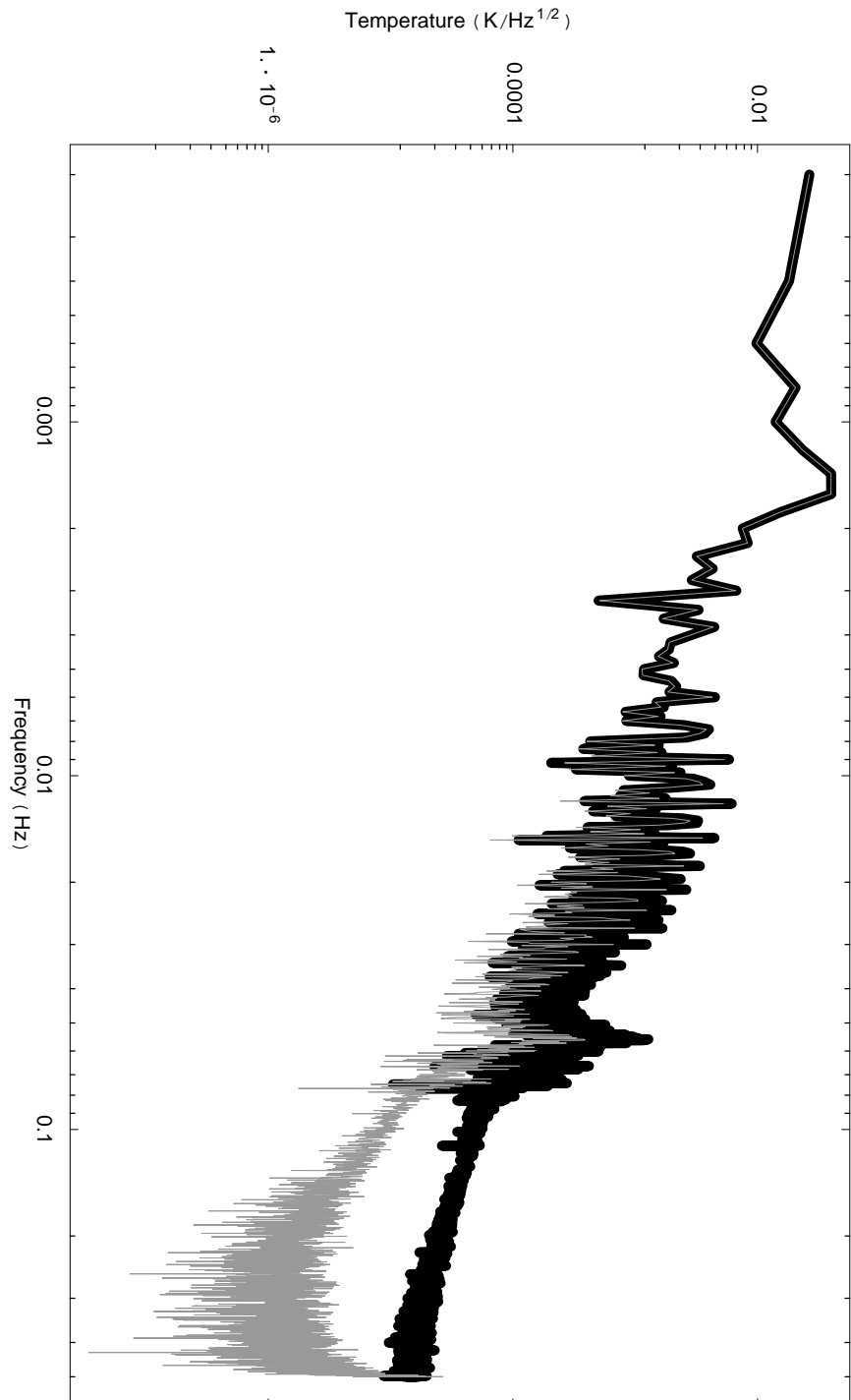


Figure 5.18: Fourier transform of the data sets shown in figures 5.16 (thick black line) and 5.17 (thin gray line). Note how the heat fluctuations are damped when propagating from HFI to the LFI radiometers: the greater the frequency is, the better it is damped.

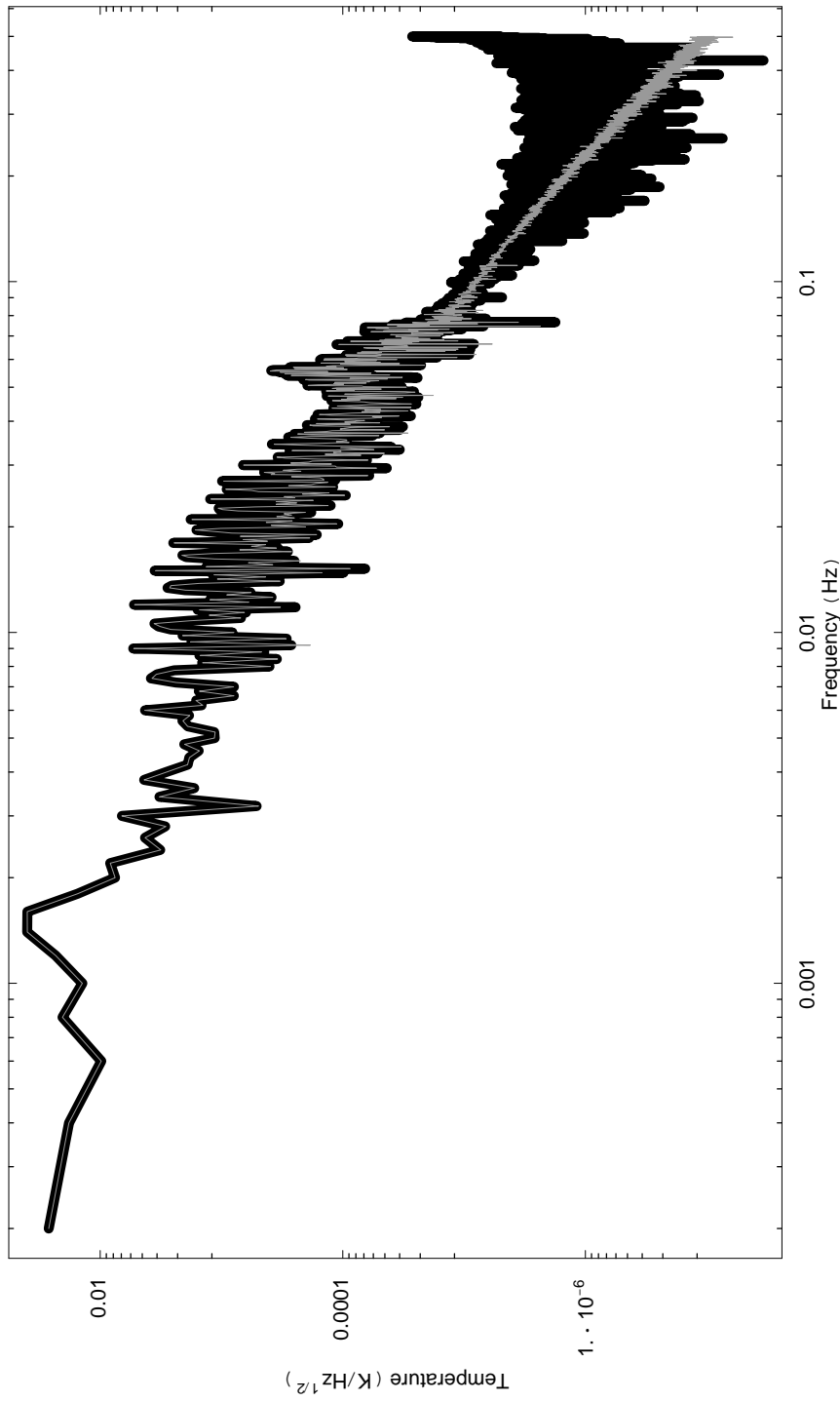


Figure 5.19: Comparison between the numerical model given by heat (thick black line) and the analytical formula for equation (4.2.14) on page 56 (thin gray line). The discrepancy at the right side of the plot could be due to the aliasing effect of the Discrete Fourier Transform (see text).

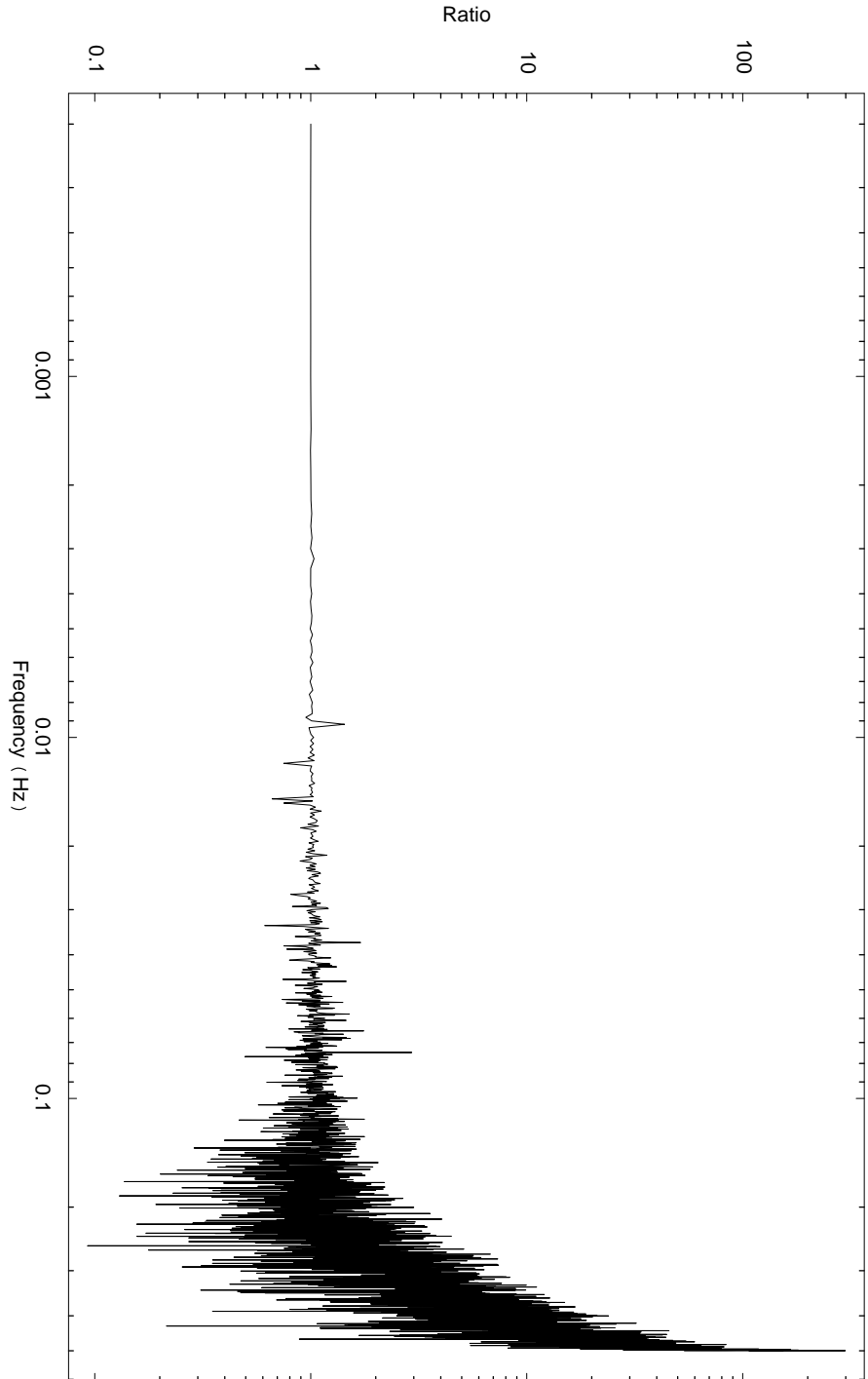


Figure 5.20: Ratio between the numerical data calculated by `heat` and the analytical formula. This ratio should be close to 1. We see that this does not hold for high frequencies, but only if $\nu \lesssim 0.2$ Hz. If $\nu \sim 1$ Hz, the numerical simulation is greater than the analytical formula. This means that the numerical formula dampens quick fluctuations less than the analytical one.

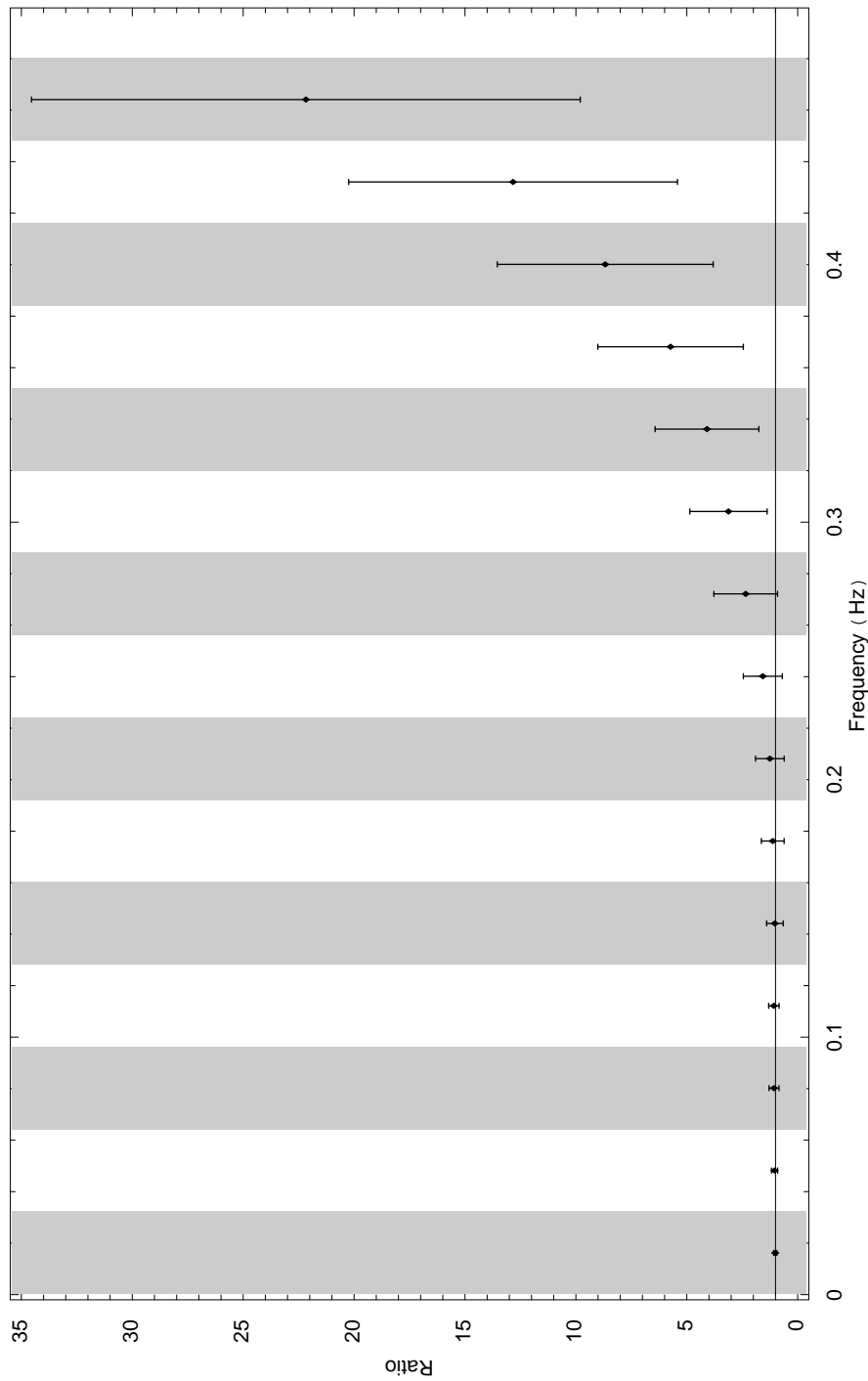


Figure 5.21: This plot shows the ratio between the numerical data calculated by `heat` and the analytical formula, like figure 5.20 on the facing page. The difference is that here the frequency domain has been split into bands ($\Delta\nu \sim 0.03$ Hz), in which the ratio has been averaged to one point. This means that every sample represents an average over many frequencies (the sample point is arbitrarily placed in the center of the band). The error bars are the standard deviation from the average value.

§ 5.3 Propagation of Boundary Heat Flux Periodic Fluctuations

Since this study is devoted to the characterization of the reference loads in the PLANCK experiment, we must consider temperature fluctuations in the LFI radiometers to estimate p_0 and p_d . Crude calculations show that the total power coming on each reference load will be about $A p_0 \sim 10^{-5}$ mW (with $A \sim 1.5$ cm² being the reference load surface), and the fluctuation amplitude will be $A p_d \sim 10^{-8}$ mW (obviously this value is frequency-dependent: we choose a “mean” estimate). Then, the induced fluctuation in the reference load is

$$\delta T_f \lesssim \frac{a}{k} p_d \approx 15 \text{ nK}, \quad (5.3.1)$$

very small when compared with typical HFI temperature fluctuations (whose order of magnitude is $1 \mu\text{K}$). Then, I decided not to use the 2-D model in this context because the 1-D model shows that the influence of heat flux fluctuations is negligible with respect to HFI fluctuations.

The temperature profile for the 1-D model was derived in section 4.3.1 on page 59:

$$T(x, t) = \frac{a-x}{k} p_0 + T_0 + \frac{a}{k} p_d \gamma_f(x, \nu) \sin(2\pi\nu t + \psi_f(x, \nu)), \quad (\rightarrow 4.3.6)$$

where $\gamma_f(x, \nu)$ and $\psi_f(x, \nu)$ are defined in equation (4.3.7a) on page 60 and equation (4.3.7b). See **figure 5.22**, **5.23** and **5.24** for a plot of these two functions.

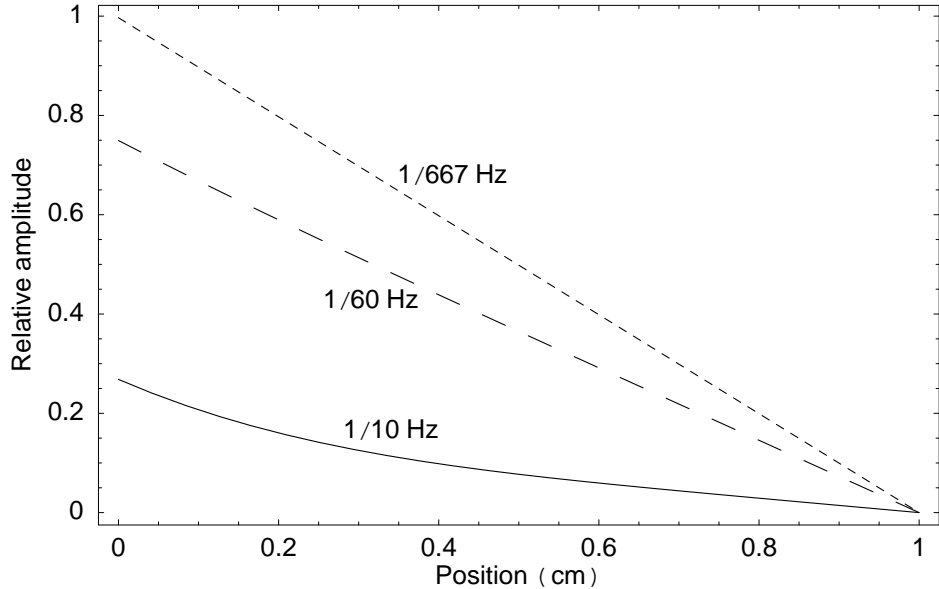


Figure 5.22: Amplitude of temperature fluctuations induced at $x = 0$ by a sinusoidal heat flux in a body with $a = 1$ cm. The “relative amplitude” is simply $\gamma_f(x, \nu)$.

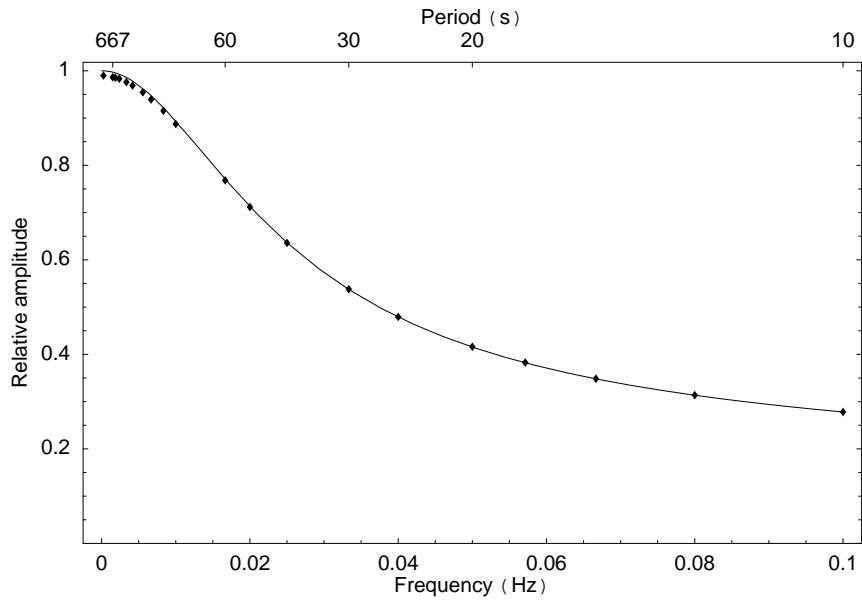


Figure 5.23: Relative amplitude at $x = 0$ for a sinusoidal fluctuation of frequency $\nu = 0$ in the heat flux coming at $x = 0$. The points show the results of a numerical simulation, and are in good agreement with our analytical model. The “relative amplitude” is simply $\gamma_f(x, \nu)$.

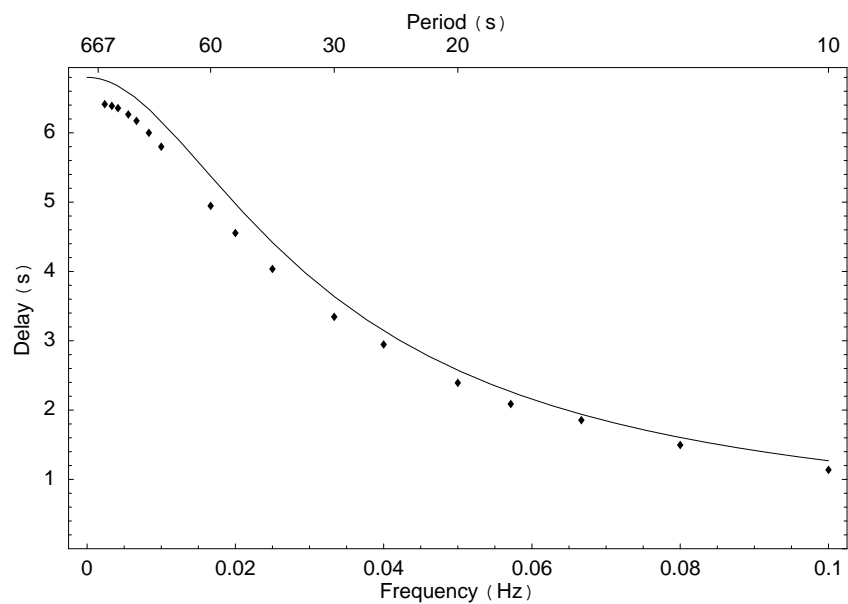


Figure 5.24: Time delay between a heat flux peak and a temperature peak at $x = 0$. The points show the results of a numerical simulation.

Note the behaviour of $T(x, t)$ at $x = a$ (side of the HFI shield): since $e_n(a) = 0$ for all $n \geq 0$, then $\gamma_f(a, \nu) = 0$. This is obvious, since in $x = a$ our boundary condition $T(a, t) = T_0$ states that the temperature does not fluctuate. At the opposite side ($x = 0$) the fluctuation amplitude is at its maximum, while for $0 < x < a$ the shape of $\gamma_f(x, \nu)$ is approximately linear, especially if ν is small:

$$\gamma_f(x, \nu) \approx \left(1 - \frac{x}{a}\right) \gamma_f(0, \nu) \quad (5.3.2)$$

with an error less than $\sim 2.5\%$ if $\nu \lesssim 1/100$ Hz. If $\nu = 1/60$ Hz, the approximation gives a result that is $\sim 7\%$ accurate, while if $\nu = 1/667$ Hz the error is $\sim 0.06\%$. See **figure 5.22** on page 84.

If $\nu \rightarrow \infty$ then $\gamma_f(x, \nu) = 0$ identically: since

$$\lim_{\nu \rightarrow \infty} c_n(\nu) = 0, \quad (5.3.3a)$$

$$\lim_{\nu \rightarrow \infty} s_n(\nu) = -\frac{\sqrt{2a}}{\pi^2 z_n^2} \quad (5.3.3b)$$

and

$$\sum_{n=0}^{\infty} \lim_{\nu \rightarrow \infty} s_n(\nu) e_n(x) = \frac{x}{a} - 1 \quad (5.3.4)$$

(series expansion of $x/a - 1$ using $\{e_n\}$ as basis), then from equation (4.3.7a) on page 60 follows that

$$\begin{aligned} \lim_{\nu \rightarrow \infty} \gamma_f(x, \nu) &= \lim_{\nu \rightarrow \infty} \sqrt{\left(\sum_{n=0}^{\infty} c_n(\nu) e_n(x)\right)^2 + \left(1 - \frac{x}{a} + \sum_{n=0}^{\infty} s_n(\nu) e_n(x)\right)^2} = \\ &= \sqrt{0 + \left(1 - \frac{x}{a} + \frac{x}{a} - 1\right)^2} = 0. \end{aligned} \quad (5.3.5)$$

If a radiative heat fluctuation has high ν , then this fluctuation will not influence the thermal behavior of the reference load (like high-frequency temperature fluctuations at $x = a$).

The phase shift of the temperature fluctuation at the interface ($x = 0$) is related to the time interval between a maximum in the heat flux coming from the LFI antenna and the next maximum in the temperature of the reference load. Note from figure 5.24 that $\psi(x = 0, \nu)/(2\pi\nu) \neq 0$ even if $\nu = 0^+$: that is, there is always a delay between the heat flux peak and the body temperature peak, even at $x = 0$ and even if $\nu \searrow 0$; if ψ is the phase shift, then the time delay is

$$t = \frac{|\psi(x = 0, \nu)|}{2\pi\nu}. \quad (5.3.6)$$

5.4 Combined Effect of Temperature and Heat Flux Periodic Fluctuations 87

We shall now calculate t_0 , the phase shift for $\nu \searrow 0$. Since $\psi(0,0) = 0$, the definition for t leads to an indeterminate form $0/0$. By using the theorem by L'Hôpital, we have that:

$$t_0 = \frac{|\partial_\nu \psi(x=0, \nu)|_{\nu=0}}{2\pi}. \quad (5.3.7)$$

It is simple to show that

$$\partial_\nu \psi(0,0) = \frac{(1 + \sum s_n(0)) \sum c'_n(0) - \sum c_n(0) \sum s'_n(0)}{\sum c_n(0) + (1 + \sum s_n(0))^2}. \quad (5.3.8)$$

Note that $\sum s_n(0) = 0$, $\sum c_n(0) = 0$, $\sum s'_n(0) = 0$, because c_n , s_n and s'_n are proportional to $p(\nu)^n$ for some n , and $p(0) = 0$. It follows that

$$\partial_\nu \psi(0,0) = \sum c'_n(0) = -\frac{2\pi a^2}{3D} \quad (5.3.9)$$

and then t_0 is given by

$$t_0 = \frac{|\partial_\nu \psi(0,0)|}{2\pi} = \frac{a^2}{3D} \sim 7 \text{ s} \quad (5.3.10)$$

if $a = 1$ cm. Note that $t_0 \propto a^2$: the dependence of t_0 on the length of the reference load gives some hints about its physical meaning. A possible explanation is that the maximum temperature at $x = 0$ can be reached only when the energy associated with the heat peak has been “distributed” from $x = 0$ in the whole body: if a is very small or D is very large, this condition can be quickly reached and t is therefore smaller.

§ 5.4 Combined Effect of Temperature and Heat Flux Periodic Fluctuations

From equation (4.4.8) on page 61 we can infer that, since $T_d \gg a p_d/c$, any fluctuation in the radiative heat flux is negligible and does not influence significantly the thermal stability of the reference loads (within a level of $\sim 98.5\%$).

CHAPTER 6

Other Applications of the EE Method

§ 6.1 Damping Improvements using Thermal Breaks

In this section we shall study the effect of a thin thermal insulator placed between the reference load and the HFI shield (between $x = a$ and $x = a'$; see **figure 6.1**) to further damp temperature fluctuations from the HFI shield.

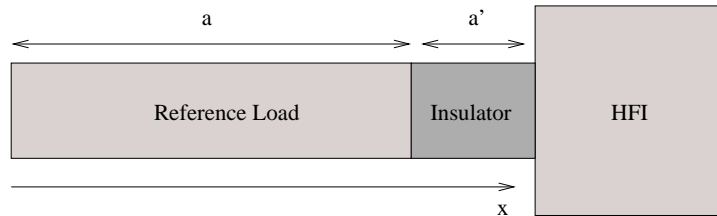


Figure 6.1: By placing an insulator between the reference load and the HFI shield, one can reduce the amplitude of temperature fluctuations coming from the HFI.

A complete thermal model of the HFI shield is currently under development. The possibility that this model shows temperature fluctuations above the requirements of LFI (some μK for the /RLs) must be taken in account; in this case, the implementation of an insulator could fulfill the LFI requirements even in presence of a poor thermal stability in the HFI shield.

There is but a cost in implementing an insulator: its presence leads to a higher temperature in the RL, due to the fact that the PLANCK structure irradiates heat towards the RL which is not efficiently dissipated in the HFI shield. In the next section we shall quantify this temperature increase using the steady-state heat equation.

6.1.1. Steady-state case. In this paragraph we consider the steady-state problem with the one-dimensional heat equation, in order to prove that

the presence of a thermal insulator increases the temperature of the RLs.

We consider the following problem¹:

$$\begin{cases} \partial_x T_1(x) = 0, \\ \partial_x T_1(0) = -p/k, \end{cases} \quad \text{and} \quad \begin{cases} \partial_x T_2(x) = 0, \\ T_2(a + a') = T_a, \end{cases} \quad (6.1.1)$$

where p is the power coming from the LFI antenna, k the thermal conductivity of the RL, $T_1(x)$ the temperature of the RL (defined for $x \in [0, a]$) and $T_2(x)$ the temperature of the insulator (defined for $x \in [a, a + a']$). We require an appropriate thermal link at the interface:

$$T_1(a) = T_2(a), \quad (6.1.2a)$$

$$k \partial_x T_1(a) = k' \partial_x T_2(a), \quad (6.1.2b)$$

supposing that the two bodies have the same temperature and heat flux at the interface.

The solution is

$$T_1(x) = T_a + \frac{a-x}{k} p + \frac{p}{k'} a', \quad (6.1.3a)$$

$$T_2(x) = T_a + \frac{a+a'-x}{k'} p, \quad (6.1.3b)$$

and it consists of two straight lines joining at $x = a$, where T_1 (temperature of the rod) differs from the standard steady-state solution without insulator $T(x) = T_a + p(a-x)/k$ because of the additive term

$$\boxed{T_{\text{ins}} = \frac{p}{k'} a'}, \quad (6.1.4)$$

which is the temperature increase due to the presence of the thermal insulator. In fact, the insulator prevents the rod from releasing too much heat (coming from LFI) to the thermal mass, so the RL is warmer.

For the RL mounted on LFI we expect p to be about 10^{-11} W/cm²; common insulators like G-10CR have $k \sim 10^{-3}$ W/cm/K at ~ 4 K. Supposing that the insulator will be about 1 mm thick (the maximum allowed insulator thickness will not be far greater than this value because of mechanical constraints), this means that $T_{\text{ins}} \sim 10$ nK. This value is very small if compared with typical HFI temperature fluctuations (~ 1 μ K), so the implementation of a thermal insulator is not prevented by these calculations.

¹This follows from the fact that the thermal conductivity is a two-valued function:

$$k(x) = k + (k' - k) \theta(x - a'),$$

where θ is the step function, k and k' the thermal conductivities of the RL and the insulator, respectively. In literature this problem is often solved by using the following variable substitution:

$$\theta(x) = \int_{a+a'}^x \frac{k(\xi)}{k(0)} T'(\xi) d\xi,$$

6.1.2. Temperature Fluctuation in the Thermal Mass. In this chapter we consider the effect of a thermal insulator placed at the interface between HFI and the RL in presence of temperature fluctuations at the interface. In particular we shall focus on fluctuations that are synchronous with the satellite spin frequency ($\sim 1/60$ Hz) as these are potential sources of spin-synchronous systematic effects.

In order to simplify the calculations, we ignore the presence of the RL and consider the thermal insulator alone. With this assumption we can use the 1-D model developed in section 4.2.1 on page 55, with the precaution to change a (length of the RL) with a' (thickness of the insulator). The boundary conditions are:

1. On one end, a temperature fluctuation with shape

$$T(t) = T_0 + T_d \sin(2\pi\nu t). \quad (6.1.5)$$

Frequency ν , fluctuation amplitude T_d and temperature T_0 are supposed to be constant in time.

2. On the other end, heat flux $p(t)$ is zero ($[p] = \text{W}/\text{cm}^2$).

Figure 6.2 on the next page shows a plot of D versus the thickness a' of the insulator. The gray area shows those points (a', D) that satisfy the following condition:

$$\gamma(1/60 \text{ Hz}, a', D) < \frac{1}{10}. \quad (6.1.6)$$

Since this model does not consider the reference load, the requirement we get from these calculations will be overestimated: in the experimental apparatus the reference load will provide a further damping mass (1/60 Hz fluctuations are damped to 75% of their original amplitude by a 1 cm-long box of Eccosorb, as we said in section 5.2.1 on page 69).

6.1.3. Possible Choices for the Insulator Material. I searched for possible materials that satisfy the requirements stated in the previous section, mainly polymers and graphites. The materials considered are reported in **table 6.1** on the next page.

At room temperature polymers such as polystyrene and molded polypropylene would be a good choice, since the required insulator thickness is a few millimeters. At cryogenic temperatures I found data only for G-10CR and Kapton; these materials would require a large thickness (~ 5 cm) in order to effectively damp temperature fluctuation at 10% level, but mechanical constraints prevent the insulators from being more than a few millimeters thick. Further investigation has to be made to find better cryogenic insulators.

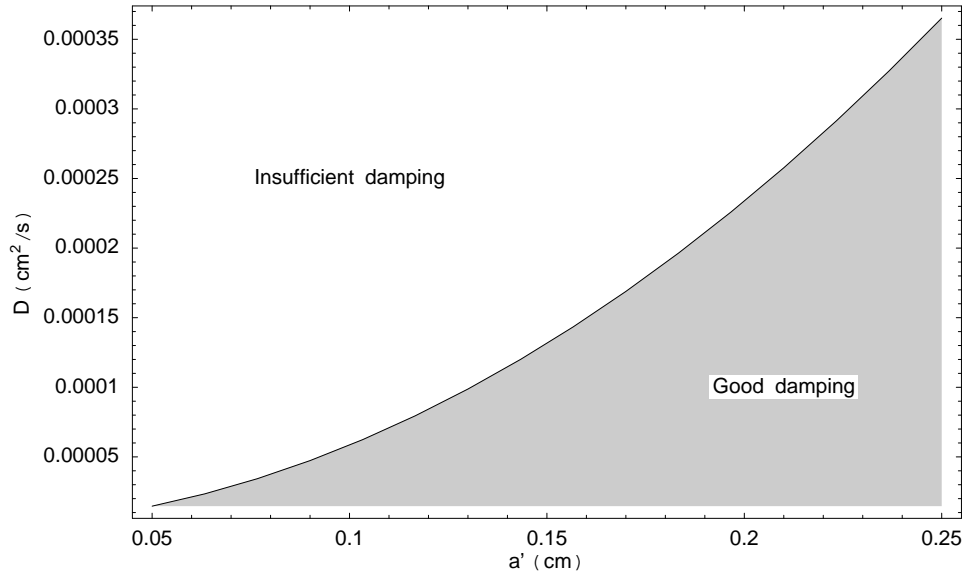


Figure 6.2: The plot shows under what conditions a thermal insulator can damp 1/60 Hz fluctuations down to 1/10 of their original amplitude. A thermal insulator is identified by its length a and its thermal diffusivity D (which depends on the material used), that is, by a point in the plot. If the point lies in the gray region, then thermal fluctuations at 1/60 Hz will be reduced to 1/10 and less of their initial amplitude.

	$T(\text{K})$	$D(\text{cm}^2/\text{s})$	Required $a'(\text{cm})$
ORNL Graphite ^a	300	4.5	$\gtrsim 27.7$
Graphite ^b	300	3.84×10^{-2}	$\gtrsim 2.6$
Polystyrene	300	7×10^{-4}	$\gtrsim 0.4$
Molded Polypropylene	300	5.8×10^{-4}	$\gtrsim 0.3$
G10 ^c	4	2×10^{-1}	$\gtrsim 5.8$
Kapton ^c	4	9×10^{-2}	$\gtrsim 3.9$

^a Highly conductive graphite, given as reference.

^b Considering an heat flow perpendicular to lattice planes.

^c From Marquardt et al. (2002).

Table 6.1: Possible choices for the material to be used in thermal insulators. For each element the minimum thickness a' for damping 1/60 Hz fluctuations to 1/10 is reported.

§ 6.2 Laboratory Measurements of Thermal Constants

In this section we shall discuss the current status of the laboratory measurements conducted at the TESRE institute in Bologna (Italy) by Dr. Luca Valenziano and his collaborators. These experiments aim at measuring the physical properties of the Eccosorb CR110 and CR117, which are the materials that will be used in the LFI RL; till now, only CR110 has been used in the experiments. In particular, we shall show a possible approach to analyze

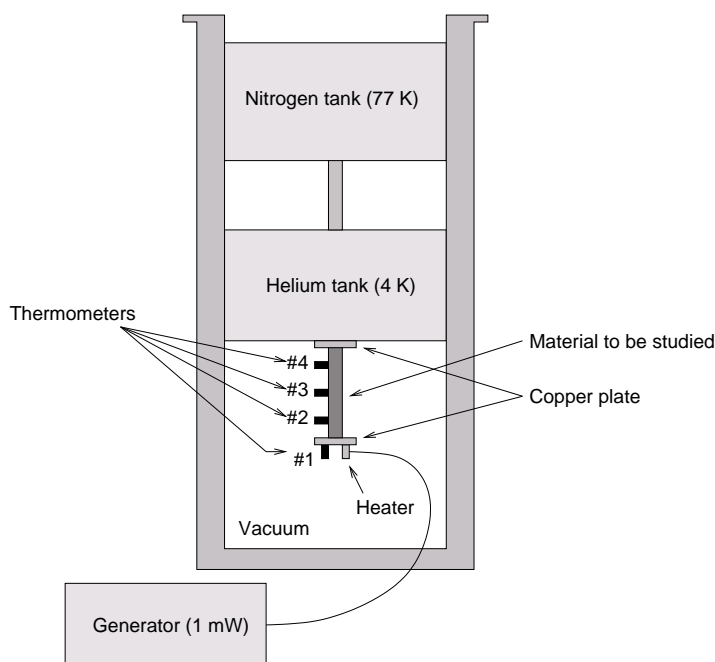


Figure 6.3: The apparatus used at TESRE for measuring the Eccosorb CR110 physical properties. Details are in the text.

the results of these experiments by using the mathematical theory developed in the previous chapters.

6.2.1. The Apparatus. The current layout of the apparatus is shown in **figure 6.3** and **figure 6.4**. This apparatus has been used to measure the thermal constants of Eccosorb CR110, but it shall be used for other kinds of cryogenic measurements on the RL as well.

The material to be studied is shaped as a cylindrical rod of some length a and placed in a vacuum chamber, in thermal contact with an helium tank through a copper plate. The helium tank is cooled down to 4K with the aid of a pre-cooling nitrogen chamber (77 K). At the opposite end of the rod there is another copper plate which is linked to a generator (~ 1 mW) through a Nichrome Heater Wire NC-32 (resistance at 4.2 K: 33.2Ω ; total length: 121 cm; effective length²: 98 cm). The generator can heat the plate with a power of about 0.4 mW.

Four germanium thermometers (LakeShore GR200A; at 4.2 K the sensitivity is 0.3 mK and the accuracy is ± 25 mK) are used in the experiment: three are placed on the rod, while the fourth is placed on the heater plate that is to be heated (see **figure 6.3**). With this thermometer it is possible sample temperature data near the heater, in order to check if the apparatus works as expected. From now on the axis of the rod will be the x axis, with

²This is the length of the wire between the generator and the plate.

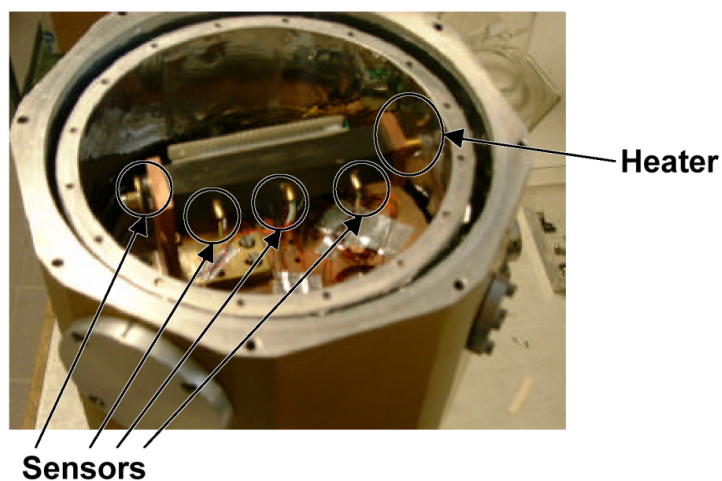


Figure 6.4: A picture of the instrument with the bottom cover removed. The configuration shown has been changed for the experiment discussed in the text: the first sensor (leftmost) is now placed on the heater plate (on the right).

#1	#2	#3	#4
On the plate	1.50 cm	3.80 cm	6.45 cm

Table 6.2: Position of the four temperature sensors. The heat plate is placed at $x = 0$, while the plate connected to the helium tank is at $x = a = (8.00 \pm 0.05)$ cm.

$x = 0$ being the position of the heater plate. The positions of the sensors are reported in **table 6.2**.

The copper wire radiates heat towards the rod, but the power is less than 0.3% of the power given by the copper plate by conduction. So, the problem can be considered purely conductive.

6.2.2. Experimental Details. The physical parameters of the Eccosorb CR110 to be used for the LFI reference loads are not well known: the accuracy of the values given in table 3.1 on page 37 (taken from the Cullmore & Ring datasheets) is not known. So, the first experiments at the IASF aim at obtaining better measurements of these constants.

The current outline of the experiments is the following: after the apparatus has reached thermal equilibrium (rod at ~ 4 K), the generator is powered on and the rod is heated in a certain amount of time. By measuring how temperature changes in the rod, one can deduce the thermal constants for the Eccosorb CR110. In the next sections I shall present some data and propose a physical interpretation for them.

6.2.3. Data Analysis of a Set of Measures. A set of measures has been taken during July 2002 at the TESRE with a (8.00 ± 0.05) cm rod made by Eccosorb CR110. During the experiment the generator was repeatedly turned on and off, with a period of about 30 minutes, while the sensors were

monitoring the temperature of the rod (at three different points) and of the heater plate. In this section I shall analyze the data taken during one of the cooling phases.

Figure 6.5 on the facing page shows the temperature profile measured at the four sensors (sensor 1 is placed on the copper plate) immediately after having turned off the generator. Each sensor measured an exponential-like decrease in the temperature. The temperature at $t = 0$ measured by the three sensors on the bar show a gradient (induced by the generator) which is clearly visible in **figure 6.6** on page 96. Some notes about this plot:

1. The difference at $t = 0$ between the heater plate temperature (upper purple box at $x = 0$) and the extrapolated value (dashed line) suggests the presence of a contact resistance between the plate and the rod or a temperature gradient in the copper plate.
2. Temperature inside the rod at $t = 0$ shows a good fit with a straight line. The method of least squares gives the following fit:

$$T(x, t = 0)[\text{K}] = q + mx = (7.052 \pm 0.0006) - (0.3137 \pm 0.0015)x[\text{cm}]. \quad (6.2.1)$$

3. By interpolating the previous formula at $x = a = 8.0$ cm for $t = 0$ we get the temperature of the rod near the interface with the helium tank:

$$T(x = 8 \text{ cm}, t = 0) = (4.54 \pm 0.03) \text{ K} \quad (6.2.2)$$

4. At $x = a = 8.0$ cm the temperature decreases from $t = 0$ to $t = 600$ s by ~ 0.3 K. Since the helium tank does not change its temperature with time, this means the thermal contact between the tank and the rod is not perfect.

6.2.4. An Analytical Model. The two copper plates present in the current experimental layout introduce some problems in the comparison between numerical and analytical methods. Presently work is in progress to modify the apparatus to eliminate these drawbacks; in this section I shall present the current status of the analytical model. Improvements to this model will be discussed in the next chapter.

The analysis of the experimental data is complex because there is a possible contact resistance at the two interfaces between the rod and the copper plates. This is evident from **figure 6.6** on page 96: at $x = 0$ there is a temperature gap between the analytical model (red line) and the temperature of the plate (upper purple box at $x = 0$), while at $x = 8$ cm the temperature is not constant in time, but show a ~ 0.3 K decrease from $t = 0$ to $t = 600$ s.

As a first approximation, I analyzed the cooling of the rod after the generator has been powered off: the heat exchanged between the plate and

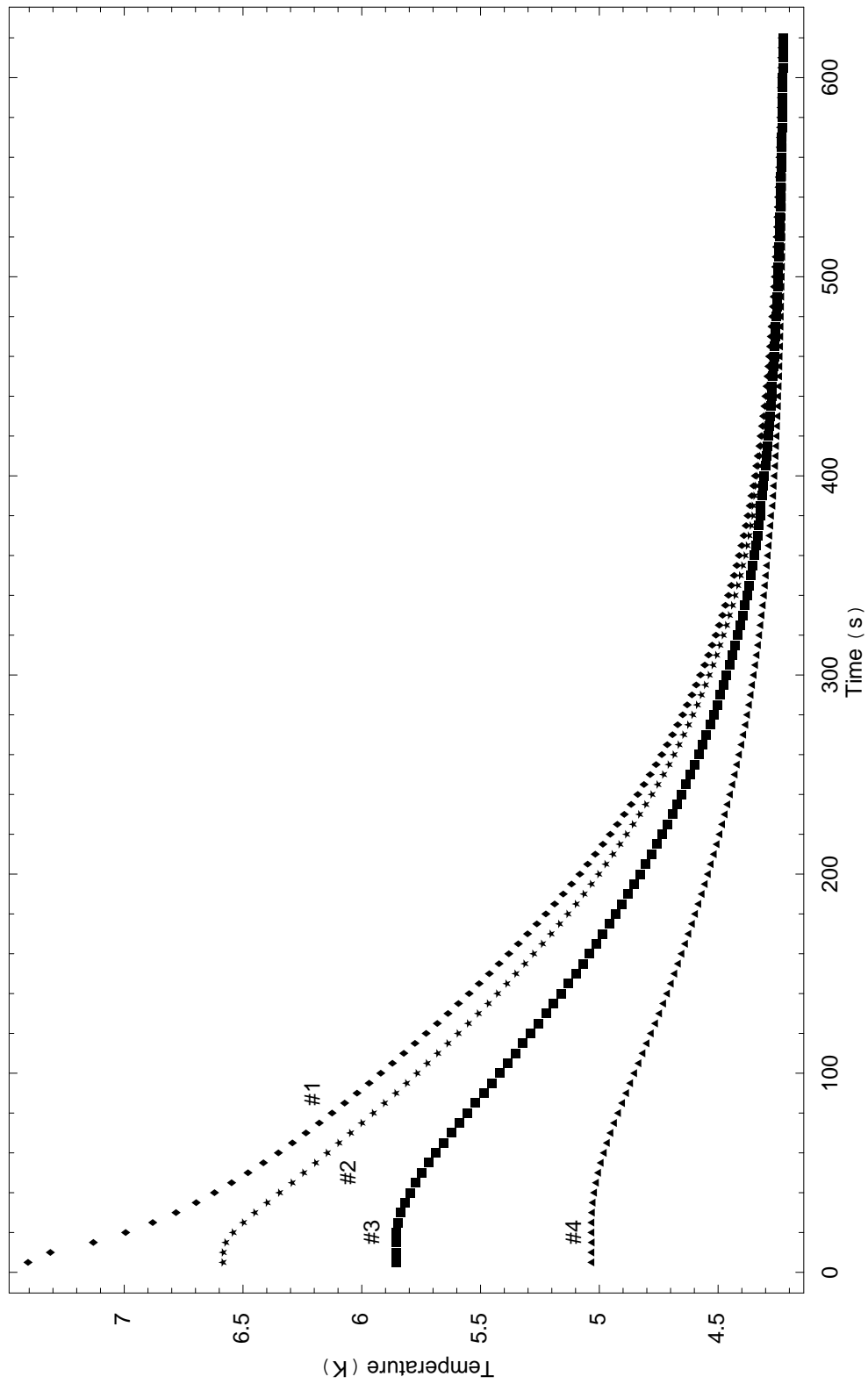


Figure 6.5: Temperature profile of the Ecosorb CR110 rod at the four sensors. The generator was powered on and then shut down after the system reached thermal equilibrium. The data are collected since the generator has been turned off. The four sensors have different temperatures at $t = 0$, meaning there is a temperature gradient in the rod.

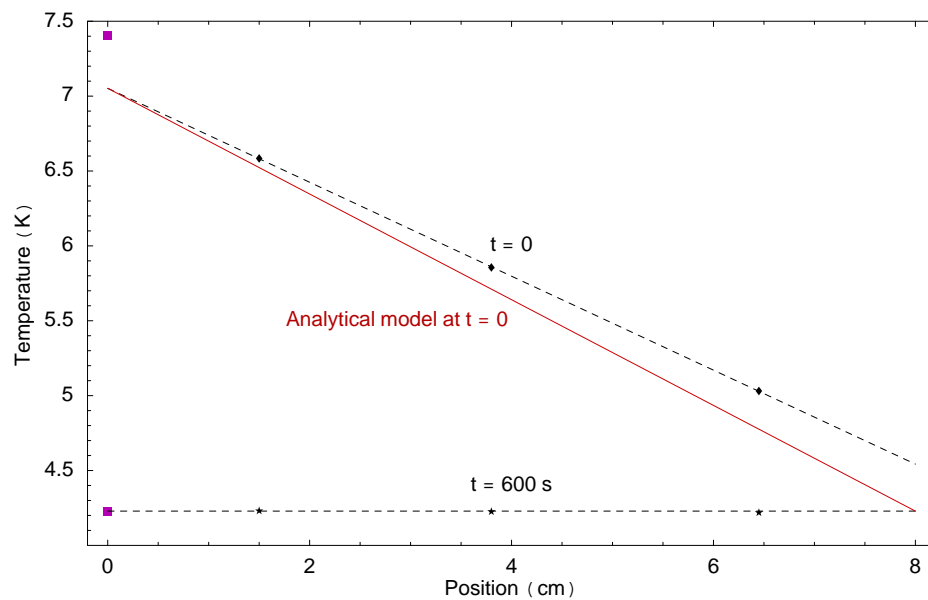


Figure 6.6: Stationary profile at $t = 0$ and $t = 600$ s. The temperature on the heater plate both at $t = 0$ and $t = 600$ s is drawn as a purple box at $x = 0$. The dashed line shows a linear interpolation on the $t = 0$ data which has left off the first sample (for obvious reasons), while the red line shows the analytical solution at $t = 0$ (which considers no contact resistance).

the rod in this phase is very small when compared with the heat released by the rod to the helium tank, so the overall thermal influence of the heater plate on the rod is negligible. If the plate cools off from $T(x = 0, t = 0) = 7.5 \text{ K}$ to $T_{\text{end}} = 4.2 \text{ K}$, then the heat it releases to the rod is

$$Q' = S' \delta x \rho' c' \Delta T \approx 5.3 \times 10^4 \text{ erg}, \quad (6.2.3)$$

where $S' = 4 \text{ cm}^2$ is the plate area, $\delta x = 0.5 \text{ cm}$ is the plate thickness, $\rho' = 8.92 \text{ g/cm}^3$ and $c' = 910 \text{ erg/g@4 K}$ are the copper density and specific heat, and $\Delta T \approx 3.3 \text{ K}$ is the temperature variation in the plate. The heat released by the rod to the helium tank is

$$\begin{aligned} Q &= \int_0^a c \Delta T(x) \rho S \, dx = & (6.2.4) \\ &= \int_0^a c (T(x, t = 0) - T_{\text{end}}) \rho S \, dx = \\ &= c \rho S \int_0^a (q - mx - T_{\text{end}}) \, dx = \\ &= c \rho S \left((q - T_{\text{end}}) a - \frac{1}{2} m a^2 \right) = \\ &= 4.7 \times 10^6 \text{ erg}, & (6.2.5) \end{aligned}$$

where q and m are given in equation (6.2.1), $S = 2.25 \text{ cm}^2$ is the rod cross-sectional area of the rod and the other constants are given in table 3.1 on page 37. Since $Q \gg Q'$, we choose to ignore the presence of the copper plate.

Using this approximation and supposing a perfect thermal contact between the rod and the helium tank, we use equation (3.3.1a) on page 39 (heat propagation in one dimension) with the following boundary conditions:

1. The heat exchanges near the copper plate are negligible, i.e. $p(t) = 0$.
2. The temperature at the interface between the rod and the helium tank is constant: $T_a(t) = T_a$.

By using the EE method, the heat conduction problem is solved by finding a solution for equation (3.3.15) on page 41 with $p'(t)$ and $T_L'(t)$ both being zero:

$$\varphi_n'(t) + \frac{1}{\tau_n} \varphi_n(t) = 0. \quad (6.2.6)$$

The solution is obviously

$$\varphi_n(t) = \varphi_n(0) \exp\left(-\frac{t}{\tau_n}\right), \quad (6.2.7)$$

where $\varphi_n(0)$ is given by the initial condition, that is the temperature profile in the rod for $t = 0$ (when the generator has been turned off). We can

suppose this shape to be a straight line of the form

$$T(x, t = 0) = T_0 + (T_a - T_0) \frac{x}{a} \quad (6.2.8)$$

where T_0 is the temperature at the side linked with the heater plate, while T_a is the temperature at the side linked with the helium tank. In terms of $\varphi_n(t)$, this condition is restated as

$$\varphi_n(t = 0) = \frac{\sqrt{2a}(T_0 - T_a)}{\pi^2 z_n^2}. \quad (6.2.9)$$

(remember that $\sum \varphi_n$ is equal to $T(t) - T_{\text{st}}$, where T_{st} is the stationary solution). **Figure 6.6** on page 96 shows that the measured profile is indeed a straight line (except for the first point, which is measured by the sensor placed on the heater plate).

The complete solution for the problem is

$$T(x, t) = T_a + \frac{2(T_0 - T_a)}{\pi^2} \sum_{n=0}^{\infty} \frac{\exp(-t/\tau_n)}{z_n^2} \cos\left(\frac{\pi}{a} z_n x\right), \quad (6.2.10)$$

and it has been derived from equation (6.2.7) and equation (6.2.9) as well as equation (3.3.17) on page 41. Remind that $\tau_n = \tau_n(D)$, where D (thermal diffusivity) is the only free parameter to fit.

A χ^2 -fit has been done on the temperatures reported by the second and the third thermometer using the `NonlinearRegress` function implemented by the *Mathematica* computer program. Results are reported in **table 6.3**; the error for each estimated is calculated by *Mathematica*; σ is defined by the following relation:

$$\sigma = \sqrt{\frac{1}{N-2} \sum_{i=1}^N (T_i - T(x, t_i))^2} \quad (6.2.11)$$

where N is the number of samples, T_i the i -th temperature sample and t_i the time associated to x_i . Note from table 6.3 that σ is about six times greater than the accuracy (~ 25 mK) of the measurement; this is a further proof that the analytical formula does not fit well the data.

Source	Position (cm)	D (cm ² /s)	σ (K)
#2	1.50	0.1397 ± 0.0035	0.164
#3	3.80	0.1405 ± 0.0036	0.128
#4	6.45	0.1187 ± 0.0065	0.123

Table 6.3: Estimates for the diffusivity constant D .

Figures **6.7** and **6.8** show the fit between the analytical function and the experimental data. The fit is not good, especially for the fourth sensor. It is

likely that the heater plate has some influence on the rod temperature for $t \lesssim 60$ s, since in this time-window the measured temperature decrease is not as quick as predicted by the analytical formula. The fits on the #3 and the #4 dataset are even worse; this can be explained by the fact that the contact resistance at $x = 8$ cm was neglected when deriving the analytical model, and this approximation is worse near $x = 8$ cm (see figure 6.6).

The estimates for D evaluated using datasets #2 and #3 are in good agreement and show a value three times larger than the value reported by Cullmore & Ring (table 3.1 on page 37). The meaning of this value is difficult to interpret because of the poor fit (especially for dataset #4, mainly because of the contact resistance at $x = a$). The weighted mean of datasets #2, #3 and #4 and the mean calculated without dataset #4 are reported here:

$$\begin{aligned} \text{Weighted mean: } & 0.1374 \pm 0.0023 \text{ cm}^2/\text{s} \\ \text{Weighted mean (w/o \#4): } & 0.1401 \pm 0.0025 \text{ cm}^2/\text{s} \end{aligned}$$

A better analytical model should be developed in order to improve these results. We shall discuss this in next chapter.

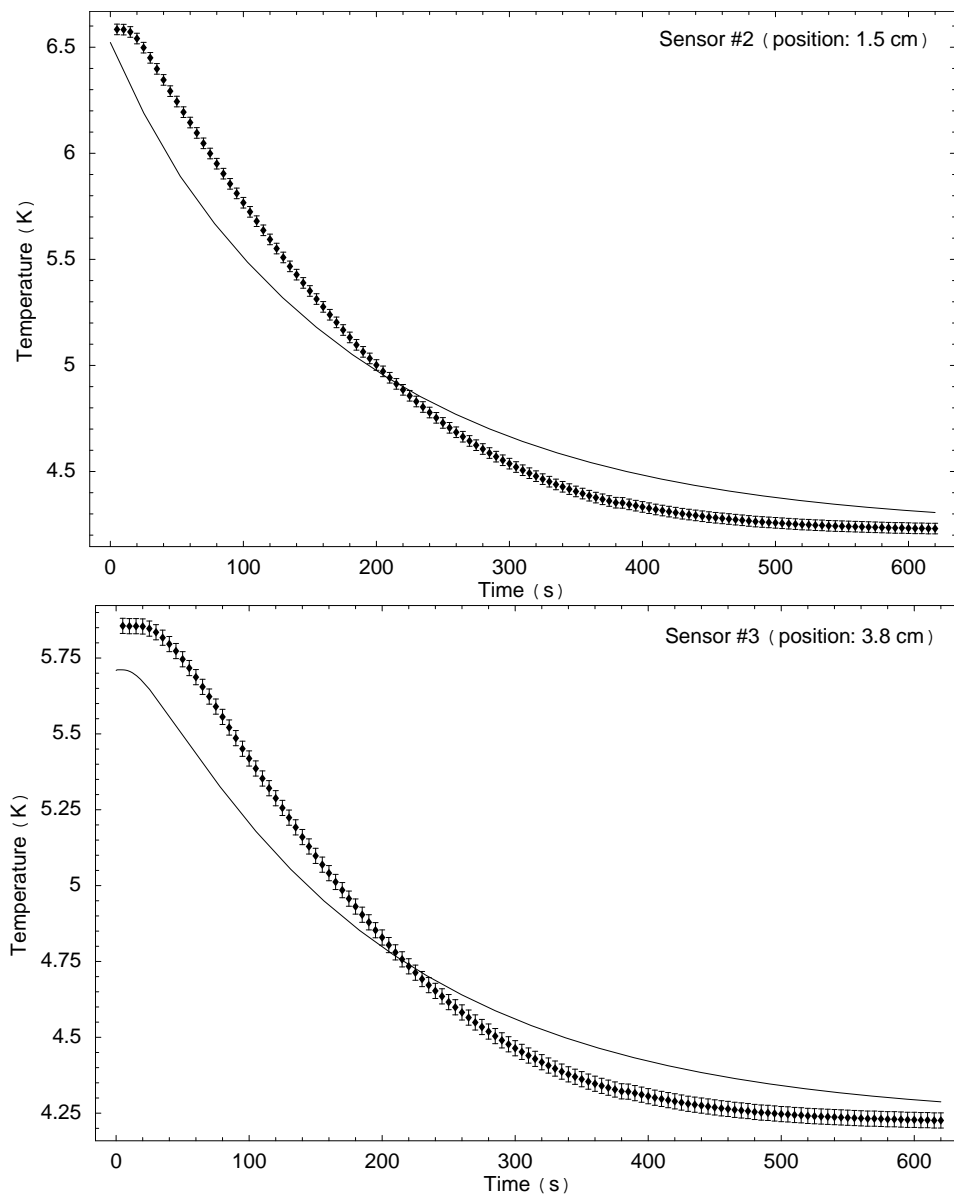


Figure 6.7: Comparison of the samples taken by the second and third temperature sensor with our analytical model. Each sample as an accuracy of ± 25 mK.

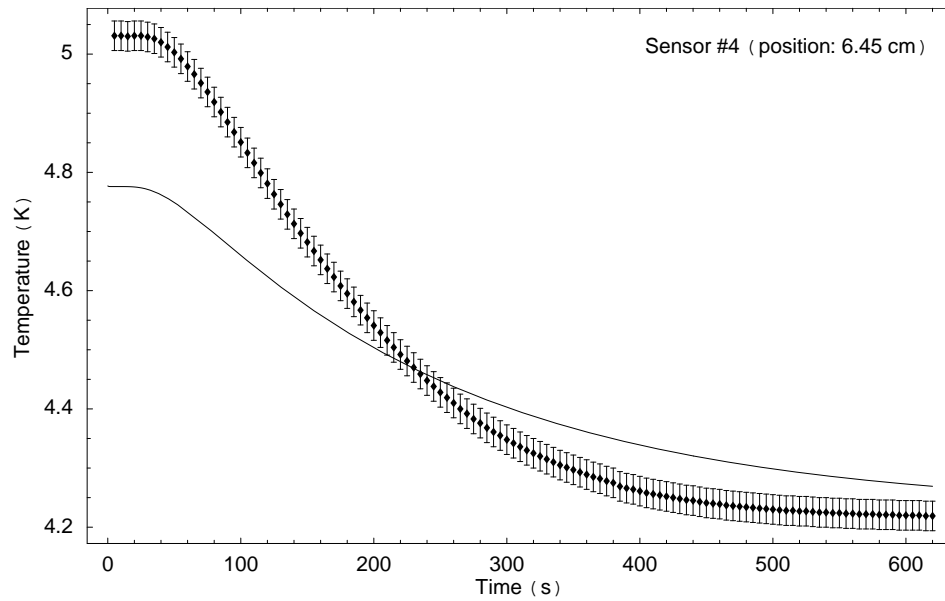


Figure 6.8: Best χ^2 -fit for the dataset #4. From the high discrepancy at $t = 0$ we can infer that the fourth sensor ($x = 6.45$ cm) is particularly sensitive to the imperfect thermal link at $x = 8$ cm between the helium tank and the rod. Each sample has an accuracy of ± 25 mK.

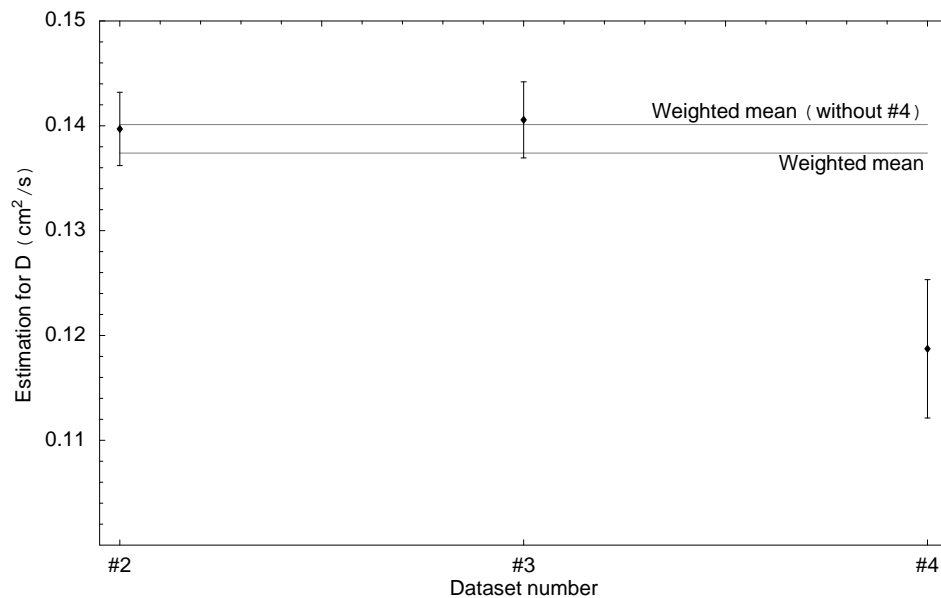


Figure 6.9: The estimated value for D . The two horizontal lines show the weighted mean of the samples; the lower one does not consider dataset #4.

CHAPTER 7

Conclusions and Future Work

§ 7.1 Conclusions

In this work I have considered the propagation of temperature fluctuations in the Reference Load (RL) used in the the PLANCK Low Frequency Instrument (LFI). The RL are fixed to the High Frequency Instrument (HFI) external shield and are used as reference blackbodies by the LFI radiometers; this requires the reference signal to be stable at the level of $\sim 1 \mu\text{K}$. The final objective of this study aims at developing a complete radiative characterization of the RL; this work discusses a 1-D/2-D analytical model of the conductive properties of the RL, and is to be considered a first step in the development of the full radiative model of the RLs.

There are many causes which lead to temperature fluctuations in the RL, both of conductive and radiative origin. The most important one is expected to be the temperature fluctuation in the HFI external shield. This work has shown that, while the high frequencies ($\nu \gg 1/60 \text{ Hz}$) are almost completely damped during the propagation in the RL, the low frequencies propagates almost without damping (this is especially true if $\nu \lesssim 1/667 \text{ Hz}$); the spin-synchronous frequency ($\sim 1/60 \text{ Hz}$) shows different damping factors according to the size of the RL (74% damping for the 30 GHz RL, to be compared with 21% for the 100 GHz). To improve the damping capabilities of the system, the implementation of a thermal insulator has been proposed to disconnect the RL from the HFI shield. This thesis has placed requirements on the material and thickness to be used in its implementation: a thermal diffusivity of $\sim 10^{-4} \text{ cm}^2/\text{s}$ is required for an insulator with a thickness of $\sim 0.1 \text{ cm}$ in order to add a factor of 10 in damping; we expect an increase in the temperature of the RL which is dependent on the thermal conductivity of the insulator (typical 1 mm-thick insulators lead to a temperature increase $< 100 \text{ nK}$).

The influence of the fluctuations in the radiative heat flux emitted by the LFI reference antenna are not as important as fluctuations at the HFI/RL

interface because of the LFI surface low emissivity: according to the analytical models, their importance is $\sim 1\%$ when compared with temperature fluctuations induced by HFI.

The material to be used in the RL (Eccosorb CR110/CR117) has to be thermally characterized because the informations provided by the seller (Cullmore & Ring) are not complete, especially for Eccosorb CR117. The team leaded by Dr. Luca Valenziano (CNR/IASF in Bologna, Italy) has developed a cryofacility to measure the thermal constants of the Eccosorb. In this work I analyzed some data taken in July 2002; the results are not conclusive because of some features of the cryofacility that are difficult to model.

§ 7.2 Other Possible Cases of Study

7.2.1. Dependence of Diffusivity on the Temperature. Till now we have considered the physical parameters as temperature-independent values. But this assumption is not always correct: in fact, specific heat of solids is dependent on the temperature T , showing a decrease to zero for $T \rightarrow 0$. This behavior is due to the *Debye effect*, and it must be considered in cryogenic experiments. In this section we consider this to be a “first order effect”, e.g. deviations of the physical parameters from the original value are small with respect to their absolute value.

Let us consider the heat equation with D being dependent on temperature T :

$$\begin{cases} \partial_t T(\mathbf{x}, t) - D(T) \nabla^2 T(\mathbf{x}, t) = 0, \\ T(\mathbf{x}, t)|_{\partial\Omega} = T_b(\mathbf{x}, t) \end{cases} \quad (7.2.1)$$

on some given domain Ω . Let us suppose that

$$D(T) \approx D_0 + D_\epsilon \frac{T - T_0}{T_0},$$

that is, $D(T)$ is expanded to first-order around temperature T_0 supposing that $D_\epsilon (T - T_0)/T_0 \ll D_0$.

We write $T(\mathbf{x}, t)$ in the following form

$$T(\mathbf{x}, t) = \tilde{T}(\mathbf{x}, t) + T_\epsilon(\mathbf{x}, t),$$

where $\tilde{T}(\mathbf{x}, t)$ is the solution of equation (7.2.1) when $D(T) = D_0$ (that is, D is not temperature-dependent); T_ϵ is the correction we are looking for. Intuitively, this quantity must satisfy the following properties:

1. If $\tilde{T} = T_0$ or $D' = 0$ then T_ϵ must be zero, since in this case $D = D_0$ and then $T = \tilde{T}$.
2. If the configuration is stationary, T_ϵ must be zero. In this case the exact value of D is not important, since it does not appear in the steady state equation $\nabla^2 T(\mathbf{x}) = 0$.

3. If D' is small, $T_\epsilon/\tilde{T} \ll 1$, that is, the correction to be added to \tilde{T} must be small.

By rewriting the heat equation and neglecting second-order terms we have

$$\begin{cases} \partial_t T_\epsilon(\mathbf{x}, t) - D_0 \nabla^2 T_\epsilon(\mathbf{x}, t) = D' (\tilde{T}(\mathbf{x}, t) - T_0)/T_0 \nabla^2 \tilde{T}(\mathbf{x}, t), \\ T_\epsilon(\mathbf{x}, t)|_{\partial\Omega} = 0. \end{cases} \quad (7.2.2)$$

This equation has the same form of equation (3.2.17) on page 34. It is basically a heat conduction equation with a “virtual” heat source, like equation (7.2.1) on the page before:

$$\dot{q}_{\text{virt}} = c_0 \rho_0 D' \frac{\tilde{T}(\mathbf{x}, t) - T_0}{T_0} \nabla^2 T_{\text{var}}(\mathbf{x}, t), \quad [\dot{q}_{\text{virt}}] = \text{W/cm}^3 \quad (7.2.3)$$

(where c_0 and ρ_0 are the specific heat and density for $T = T_0$). If $\dot{q}_{\text{virt}} = 0$ then the only possible solution for equation (7.2.2) is zero¹

Note that from equation (7.2.3) T_ϵ satisfies those properties we mentioned above:

1. If $D' = 0$ then $\dot{q}_{\text{virt}} = 0$ and $T_\epsilon = 0$ from equation (7.2.3).
2. If $\tilde{T}(\mathbf{x}, t) = T_0$ then, again, $T_\epsilon = 0$ from equation (7.2.3).
3. If $\nabla^2 \tilde{T}(\mathbf{x}, t) = 0$ then $\tilde{\theta}(\mathbf{x}, t)$ is a stationary solution. Thus $T_\epsilon = 0$.

In principle, solving equation (7.2.2) would require the same mathematical tools we developed in the previous chapter. The main problem with this particular equation is the right-hand term

$$(\tilde{T}(\mathbf{x}, t) - T_0)/T_0 \nabla^2 \tilde{T}(\mathbf{x}, t).$$

If we use a solution calculated with the EE method to express \tilde{T} , then we have the product of two series. Recall that the EE method requires to express the source term of the heat equation as a series in some \mathcal{L}^2 basis. To apply the method here, we should decompose a double series into a single series, which leads to a complex equation (although not impossible to solve).

¹It is simple to show this: if $\dot{q}_{\text{virt}} = 0$ then the PDE is linear, thus it has a null solution. If the PDE is a well-posed problem (we shall prove this in appendix C on page 114) then there exists only one solution, and thus this must be the null solution.

7.2.2. Presence of a Contact Resistance. When two bodies conducting heat are placed in contact, heat flows from the hot body to the cooler body. Contact between the two bodies is never perfect, because of microscopic imperfections in the surface flatness, unavoidable air voids along the interface and so on. This leads to a temperature gap at the interface between the two bodies, which depends on the amount of heat exchanged between them.

Thermal contact resistance is a physical quantity that measures this phenomenon. It is defined by the following formula:

$$R_C = \frac{T_1 - T_0}{Q/S}, \quad [R_C] = \text{K cm}^2/(\text{erg/s}), \quad (7.2.4)$$

where T_0 and T_1 are the temperature of the two bodies, Q the amount of exchanged heat and S the area of the interface. Common values for the contact resistance range from $10^2 \text{ K cm}^2/\text{Watt}$ to $10^4 \text{ K cm}^2/\text{Watt}$.

Considering the contact resistance in the EE method is a difficult task. Let us use the assumptions considered in section 3.3 on page 37: a one-dimensional rod which extends from $x = 0$ to $x = L$ and is in thermal contact with a massive body at $x = a$. The exchanged heat is the heat flowing from the rod to the massive body, that is:

$$Q = -k \partial_x T|_{x=a^-}$$

(temperature of the massive body is constant). Using equation (7.2.4), we obtain

$$-\frac{R_C k}{S} \partial_x T|_{x=a^-} = T|_{x=a^-} - T_0,$$

where T_0 is the temperature of the massive body. By rewriting this we obtain the following boundary condition:

$$\left[\partial_x T + \frac{S}{k R_C} T \right]_{x=a^-} = \frac{S}{k R_C} T_0.$$

To use the EE method we must find a orthonormal basis $\{e_n\}_{n=1}^\infty$ in $\mathcal{L}^2([0, a])$ which satisfy this boundary condition:

$$\partial_x e_n(a) + \frac{S}{k R_C} e_n(a) = 0, \quad (7.2.5)$$

in order to express the solution as a series in this basis. Since the basis must be built from eigenfunctions of the diffusion operator, sines and cosines must be used. We use the following basis

$$e_n(x) = \alpha_n \sin(\psi_n x),$$

where α_n and ψ_n are to be determined. Since α_n is a normalization factor, we can ignore it for the moment: we concentrate on ψ_n . In order to satisfy equation (7.2.5), the following relation must hold:

$$\tan(\psi_n x) = \frac{\alpha_n}{\psi_n}.$$

This is a transcendental equation, since the unknown appears both in the α_n/ψ_n term and as the argument of a trigonometric function. Thus no analytical solutions can be found, and the orthonormalization of the basis is problematic.

The use of numerical algorithms could help in this, but it would lead to a series of problems. For instance, finding a good basis is the first step of the EE method: by having only a numerical approximation of it, one should perform every other step by means of numerical algorithms. From this point of view, a numerical simulation with thermal analysis software would lead to the same results with much less work.

§ 7.3 Numerical 3-D Model with SINDA

The objective of a thermal study of the LFI RLs is to build a full 3-D numerical model which implements the whole geometry of the RL as shown in figure 2.5 on page 21. I developed a 3-D model using SINDA, a thermal analysis software by Cullmore & Ring, but I could not do a full test of the model because of lack of time. It is important to continue this work, because it will be used as a basis for the complete radiative model of the RL, the final objective of the studies on the RL.

Appendices

APPENDIX A

Completeness of the cosine set

Theorem A.1. *Given the operator $A = D \nabla^2$ in $\mathcal{L}^2([-a, a])$ with the following domain:*

$$\begin{aligned} \mathcal{D}(A) = \left\{ u \in \mathcal{L}^2([0, a]) : u, u' \in \mathcal{C}_{abs}([0, a]), \right. \\ \left. u'' \in \mathcal{L}^2([0, a]), u_x(0) = u(a) = 0 \right\}, \end{aligned} \quad (\text{A.1})$$

the set of functions $\{c_n\}_{n=0}^{+\infty}$ given by

$$c_n = \sqrt{\frac{2}{a}} \cos \left[\frac{\pi}{a} \left(n + \frac{1}{2} \right) x \right] \quad (\text{A.2})$$

is a complete orthonormal system for $\mathcal{L}^2([-a, a])$, and $c_n \in \mathcal{D}(A)$ for any $n \in \mathbb{N}$.

Proof. The proof that equation (A.2) is an orthonormal system for $\mathcal{L}^2([0, a])$ and $c_n \in \mathcal{D}(A)$ is simple and it is omitted. We prove here that this system is complete¹.

It is known that

$$e_n = \sqrt{\frac{1}{a}} \sin \left(\pi n \frac{x+a}{2a} \right)$$

is a basis for $\mathcal{L}^2([-a, a])$ (see Abbati and Cirelli 1997). We can write this set in the following way:

$$\begin{aligned} e_{2n} &= \frac{(-1)^n}{\sqrt{a}} \sin \left(\frac{\pi}{a} n x \right), \\ e_{2n+1} &= \frac{(-1)^n}{\sqrt{a}} \cos \left[\frac{\pi}{a} \left(n + \frac{1}{2} \right) x \right] \end{aligned}$$

¹The completeness can also be considered a consequence of the Sturm-Liouville theorem (see Gustafson 1980).

Note that e_{2n} is odd while e_{2n+1} is even.

Since $\{e_k\}_{k=0}^{+\infty}$ is a complete orthonormal system for $\mathcal{L}^2([-a, a])$, if $\tilde{f} \in \mathcal{L}^2([-a, a])$ then it follows that

$$\tilde{f} = \sum_{k=0}^{+\infty} (\tilde{f}|e_k) e_k, \quad (\text{A.3})$$

where the series converges in the norm of \mathcal{L}^2 .

Let us consider a function $f \in \mathcal{L}^2([0, a])$. We extend it to $\tilde{f} \in \mathcal{L}^2([-a, a])$ by applying the following definition:

$$\tilde{f}(x) \stackrel{\text{a.e.}}{=} \begin{cases} f(x) & \text{if } x > 0, \\ f(-x) & \text{if } x < 0. \end{cases}$$

Since $f \in \mathcal{L}^2([0, a])$, then $\tilde{f} \in \mathcal{L}^2([-a, a])$ and equation (A.3) is applicable to this case. Considering how we defined \tilde{f} , we can conclude that

$$\begin{aligned} (\tilde{f}|e_{2n})_{[-a,a]} &= 0, \\ (\tilde{f}|e_{2n+1})_{[-a,a]} &= 2(f|e_{2n})_{[0,a]}, \end{aligned}$$

since e_{2n} is odd while e_{2n+1} is even. Then,

$$\tilde{f} \stackrel{[-a,a]}{=} 2 \sum_{n=0}^{+\infty} (f|e_{2n+1})_{[0,a]} e_{2n+1}, \quad (\text{A.4})$$

where $\stackrel{[-a,a]}{=}$ indicates that the equal sign is intended in the norm of $\mathcal{L}^2([-a, a])$.

Equation (A.4) can be written in the following form:

$$\left\| \tilde{f} - 2 \sum_{n=0}^k (f|e_{2n+1}) e_{2n+1} \right\|_{[-a,a]}^2 \xrightarrow{k \rightarrow \infty} 0.$$

Since \tilde{f} is even, we can rewrite this relation like:

$$\begin{aligned} \int_{-a}^a \left| \tilde{f}(x) - 2 \sum_{n=0}^k (f|e_{2n+1}) e_{2n+1}(x) \right|^2 dx &= \\ &= 2 \int_0^a \left| f(x) - 2 \sum_{n=0}^k (f|e_{2n+1}) e_{2n+1}(x) \right|^2 dx = \\ &= \left\| f - 2 \sum_{n=0}^k (f|e_{2n+1}) e_{2n+1} \right\|_{[0,a]}^2 \xrightarrow{k \rightarrow \infty} 0. \end{aligned}$$

The last relation indicates that

$$f \stackrel{[0,a]}{=} \sum_{n=0}^{+\infty} (f | \sqrt{2} e_{2n+1})_{[0,a]} \sqrt{2} e_{2n+1} \quad (\text{A.5})$$

for each $f \in \mathcal{L}^2([0, a])$: this is the same as proving that $\{\sqrt{2} e_{2n+1}\}_{n=0}^{+\infty}$ is a complete system for $\mathcal{L}^2([0, a])$. Since this set is equal (except for the sign) to equation (A.2) on page 108, the theorem is proved. \square

APPENDIX B

Solution of the Heat Equation Using Green's Functions

It is evident that equation (3.3.3a) on page 39 is similar to equation (3.2.6) on page 32: the only difference is the presence of boundary conditions $k_x(0, t) = 0, k(a, t) = 0$. In this appendix we solve equation (3.3.3a) by applying the same method used to obtain equation (3.2.7) (solution for a infinitely long rod).

In order to solve equation (3.3.3a) we substitute F in equation (3.2.7) with another function G which satisfies the required boundary conditions (these functions are called *Green's functions*). What we want to do is to prove that the function

$$G(x, \xi, t) = \frac{1}{D} \sum_{n=-\infty}^{+\infty} (-1)^n \left\{ F[x - (2a n + \xi), t] + F[x - (2a n - \xi), t] \right\}, \quad (\text{B.1})$$

is a solution in $[0, a]$ of equation

$$G_t(x, t) - D G_{xx}(x, t) = \delta(x - \xi) \delta(t) \quad (\text{B.2})$$

and satisfies boundary conditions (3.3.3b) and (3.3.3c).

First of all, if $\xi \in [0, a]$ then equation (B.1) is a solution for equation (B.2) over $[0, a]$ because in this range the addenda in equation (B.1) simplify to zero in the left part of the equation, except $F(x - \xi, t)$ (the $n = 0$ term). This term takes care of $\delta(x - \xi) \delta(t)$ in the right side of the equation. Then $G(x, \xi, t)$ is a solution of equation (B.2).

To study its properties at $x = 0$ and $x = a$ we expand the first terms of

the sum in $x = a$:

$$\begin{aligned}
 G(a, \xi, t) &= \\
 &= \frac{1}{D} \sum_{n=-\infty}^{+\infty} (-1)^n \left\{ F[(1+2n)a + \xi, t] + F[(1+2n)a - \xi, t] \right\} = \\
 &= \underbrace{\frac{1}{D} (F(a + \xi, t) + F(a - \xi, t))}_{n=0} - \underbrace{\frac{1}{D} (F(-a + \xi, t) - F(-a - \xi, t))}_{n=-1} + \\
 &- \underbrace{\frac{1}{D} (F(3a + \xi, t) - F(3a - \xi, t))}_{n=1} + \underbrace{\frac{1}{D} (F(-3a + \xi, t) + F(-3a - \xi, t))}_{n=-2} \cdots
 \end{aligned}$$

Since $F(x) = F(-x)$, we have that

$$\begin{aligned}
 G(a, \xi, t) &= \\
 &= \underbrace{\frac{1}{D} (F(a + \xi, t) + F(a - \xi, t))}_{n=0} - \underbrace{\frac{1}{D} (F(a - \xi, t) - F(a + \xi, t))}_{n=-1} + \\
 &- \underbrace{\frac{1}{D} (F(3a + \xi, t) - F(3a - \xi, t))}_{n=1} + \underbrace{\frac{1}{D} (F(3a - \xi, t) + F(3a + \xi, t))}_{n=-2} \cdots = \\
 &= 0
 \end{aligned}$$

The sum of each pair of terms in a single line (coming from $n = k$ and from $n = -k - 1$) is always zero, and then the series is zero at $x = a$. The reason why $G_x(0, t) = 0$ is the same and it is omitted. A plot of Green's function $G(x, \frac{1}{3}, t)$ is shown in **figure B.1** on the facing page.

Now we can substitute F with G in equation (3.3.3a) on page 39, obtaining

$$\theta(x, t) = \iint_{[0, a] \times \mathbb{R}} r(\xi, \tau) G(x, \xi, t - \tau) d\xi d\tau.$$

Boundary conditions $\theta_x(0, t) = \theta(a, t) = 0$ are satisfied because of the presence of the $G(x, \xi, t - \tau)$ term. From $k(x, t)$ we can get the solution to equation (3.3.1a) on page 39:

$$\begin{aligned}
 T(x, t) &= \frac{x-a}{Dk} p(t) + T_a(t) + \iint_{[0, a] \times \mathbb{R}} r(\xi, \tau) G(x, \xi, t - \tau) d\xi d\tau \\
 &= \frac{x-a}{Dk} p(t) + T_a(t) + \\
 &- \iint_{[0, a] \times \mathbb{R}} \left(\frac{a-x}{k} p'(t) + T_a'(t) \right) G(x, \xi, t - \tau) d\xi d\tau \quad (\text{B.3})
 \end{aligned}$$

This solution expresses the temperature $T(x, t)$ as a convolution between a function of the boundary conditions and G . The convolution has to be

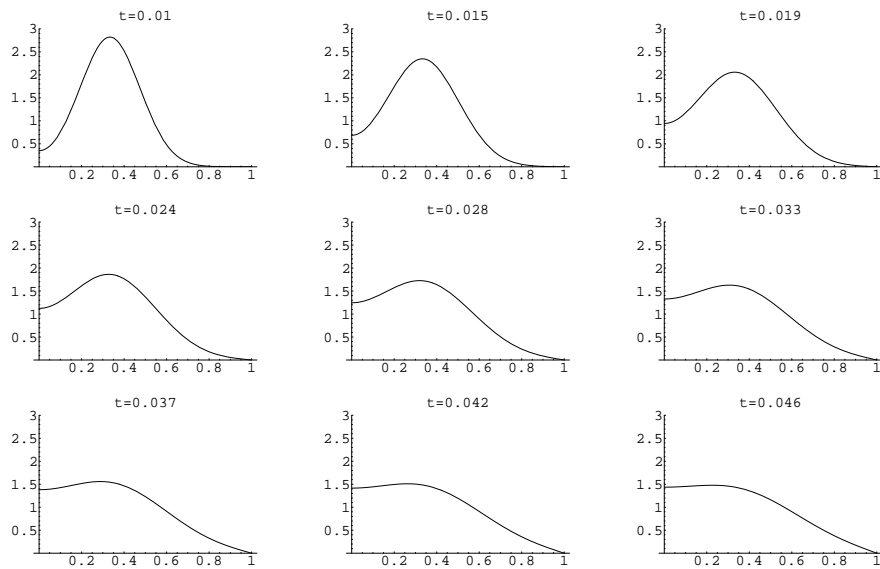


Figure B.1: Evolution of Green's function $G(x, \frac{1}{2}, t)$ with $a = 1$. Note that in $x = 0$ the function has zero slope at each time, while in $x = a$ it is equal to zero, and that the temperature peak at $t = 0.01$ is gradually trimmed off.

evaluated in the space of generalized functions, since G is expressed in terms of F , which reduces to a Dirac's delta for $t \downarrow 0$. This is the reason why the Green's functions are not simple to use in computer simulations.

APPENDIX C

Evolution Operators and Semigroups

In this appendix we discuss the role of evolution operators in justifying the Eigenfunction Expansion (EE) method. Please consult Richtmyer (1978); Showalter (1994) for a more comprehensive discussion of this topic.

§ C.1 The Problem

We consider a partial differential equation (PDE) as an equation in a Banach space \mathcal{B} , i.e. a complete normed linear space where the norm has not to be derived by an inner product.

We consider here linear equations of the following form:

$$\frac{du}{dt}(t) = C u(t), \quad (\text{C.1.1a})$$

$$u(0) = u_0, \quad (\text{C.1.1b})$$

(homogeneous equation) where C is a linear operator involving only space variables and $u_0 \in \mathcal{D}(C)$. If $C = D \nabla^2$ then equation (C.1.1a) reduces to the heat conduction equation without heat sources nor time-dependent boundary conditions (the $r(x, t)$ term in equation (3.3.3a) on page 39). We choose to consider this simpler form because the hypotheses can be easily extended; we shall discuss about this in section C.5 on page 123.

The time derivative is defined as

$$\frac{du}{dt} = \lim_{\Delta t \downarrow 0} \frac{1}{\Delta t} [u(t + \Delta t) - u(t)], \quad (\text{C.1.2})$$

where the limit is taken in the sense of the convergence in \mathcal{B} .

Definition C.1. A linear partial differential equation with boundary conditions like equation (C.1.1a) is said to be an *initial value problem*.

Boundary conditions can be taken in account by properly refining $\mathcal{D}(C)$. For example, in section 3.3.1 on page 38 we studied the one-dimensional heat

problem on $[0, a]$ by using the following operator:

$$\mathcal{D}(C) = \{u \in \mathcal{L}^2(\Omega) : u, u' \in \mathcal{C}_{\text{abs}}(\Omega), \\ u'' \in \mathcal{L}^2(\Omega), u_x(0) = u(a) = 0\}, \quad (\rightarrow 3.3.7)$$

$$C = \frac{1}{D} \nabla^2, \quad (\rightarrow 3.3.8)$$

We are concerned with the following problem: if we obtain a “general” solution $u(t) \in \mathcal{B}$ for the heat conduction problem, when does it happens that $u(t) \in \mathcal{D}(C)$? The question is very important, since if $u(t) \notin \mathcal{D}(C)$ then our solution does not satisfy the required boundary conditions and is therefore not acceptable.

By manipulating symbolically equation equation (C.1.1a), we could write the solution for equation (C.1.1a) on the preceding page in the following form:

$$u(t) = \exp(Ct) u(0) \quad (\text{C.1.3})$$

where $\exp(Ct)$ is a linear operator. If $u(0) \in \mathcal{D}(C)$, asking that $\exp(Ct) u(0) \in \mathcal{D}(C)$ is the same as requiring that $\mathcal{R}(\exp(Ct)) \subseteq \mathcal{D}(C)$. We shall develop the mathematical theory that tells when this requirement can be satisfied. At the moment, we limit ourselves to state the following definition, taken from Richtmyer (1978).

Definition C.2. C *strict solution* of equation (C.1.1a) on the facing page is a function $u(t) \in \mathcal{B}$ for all $t > 0$ such that

$$u(t) \in \mathcal{D}(C), \quad \text{for all } t \geq 0, \quad (\text{C.1.4})$$

$$\lim_{\Delta t \downarrow 0} \left\| \frac{u(t + \Delta t) - u(t)}{\Delta t} - Cu(t) \right\| = 0, \quad \text{for all } t \geq 0. \quad (\text{C.1.5})$$

§ C.2 Contraction Semigroups

To follow a more generic approach, let us rewrite $\exp(Ct)$ as a generic linear operator $S(t)$: we want to characterize it without dealing with its explicit form (at the moment). $S(t)$ is called the *evolution operator*: when applied to a function $u(t_0)$, $S(t)$ gives the evolution of $u(t_0)$ to time $t_0 + t$. With this physical meaning, the following definition should be obvious:

Definition C.3. C *continuous one-parameter semigroup*¹ on \mathcal{H} is a set

¹It is not a group, since the inverse is not always defined. In this context, the existence of an inverse $S(-t)$ would imply we can trace back the evolution of the physical system. When dealing with the heat equation this could lead to some ill-posed problems, as shown in Richtmyer (1978).

$\{S(t) : t > 0\}$ of linear operators on \mathcal{H} which satisfies

$$S(t_1 + t_2) = S(t_1)S(t_2), \quad t_1, t_2 > 0 \quad (\text{C.2.1a})$$

$$S(0) = I \quad (\text{C.2.1b})$$

$$S(\cdot)u \in \mathcal{C}([0, \infty], \mathcal{H}) \quad (\text{C.2.1c})$$

The third condition is required for the stability of the physical system under study.

Definition C.4. In this work, we refer to a *contraction semigroup* as a continuous one-parameter semigroup which satisfy

$$\|S(t)u\| \leq \|u\|, \quad u \in \mathcal{D}(S(t)), t > 0 \quad (\text{C.2.2})$$

There is a strong relation between contraction semigroups and Cauchy problems like equation (C.1.1a) on page 114. The following definition tries to establish a mathematical relation between these concepts.

Definition C.5. The *generator* of the contraction semigroup $\{S(t) : t > 0\}$ is the operator B given by

$$\mathcal{D}(B) = \left\{ u \in \mathcal{H} : \lim_{h \downarrow 0} \frac{1}{h} (S(h) - I)u = D^+(S(0)x) \text{ exists in } \mathcal{H} \right\}, \quad (\text{C.2.3a})$$

$$Bu = \lim_{h \downarrow 0} \frac{1}{h} (S(h) - I)u = D^+(S(0)x) \quad (\text{C.2.3b})$$

(D^+ is the right-derivative operator).

Example C.6. The definition seems to be quite complex, but its meaning is immediate to understand. Please recall that if f is a real function, then for small x

$$f(x) \approx f(0) + x f'(0) \quad \text{for small } x. \quad (\text{C.2.4})$$

In this context, the generator B for a contraction semigroup $\{S(t) : t > 0\}$ is such that

$$u(t) = S(t)u_0 \approx u_0 + tBu_0 \quad \text{for small } t. \quad (\text{C.2.5})$$

Thus, the generator can be used as an approximation for the evolution operator if t is small.

Example C.7. Generators are used extensively in quantum mechanics. There is a strong relation between heat conduction and quantum mechanics, since the Schrödinger equation

$$i\hbar \frac{d}{dt} \psi = H\psi \quad (\text{C.2.6})$$

has the same functional form of the heat equation. It is simple to show that in this context the time-evolution operator $U(t)$ has H (the Hamiltonian)

as generator. In this case $U(t)$ is a unitary group,² (a group of unitary operators) because the Born condition $\|\psi(t)\| = 1$ must hold for any t : this is satisfied only if $U(t)$ is unitary. In the heat-conduction case we shall see that the time-evolution operator $S(t)$ is a “true” contraction, so that $\|u(t)\|$ is a monotonically decreasing function if $t \rightarrow \infty$ (to understand why this happens, recall that in our physical problem $\|u\| = 0$ corresponds to the steady state).

The following theorems, taken from Showalter (1994), show the link between semigroup generators and Cauchy problems.

Theorem C.8. *If C is the generator of a contraction semigroup, then for each $u_0 \in \mathcal{D}(C)$ there is a unique solution $u \in \mathcal{C}^1([0, L], \mathcal{H})$ of equation (C.1.1a) on page 114 with $u(0) = u_0$.*

The meaning of this theorem is clearer if you invert it: if there is more than one solution for the Cauchy problem (a physical nonsense), then C cannot approximate a set of “good” evolution operators, since they would not satisfy those conditions given in definition C.3 on page 115 and definition C.4 on the facing page.

The following theorem generalizes the previous one to non-homogeneous Cauchy problems, which is exactly what we want: equation (3.3.3a) on page 39 is a non-homogeneous differential equation.

Theorem C.9. *If C is the generator of a contraction semigroup, then for each $u_0 \in \mathcal{D}(C)$ and each $f \in \mathcal{C}^1([0, \infty), \mathcal{H})$ there is a unique $u \in \mathcal{C}^1([0, \infty), \mathcal{H})$ such that $u(0) = u_0$, $u(t) \in \mathcal{D}(C)$ for $t \geq 0$, and*

$$\frac{d}{dt}u(t) + Cu(t) = f(t), \quad t \geq 0. \quad (\text{C.2.7})$$

The conclusion is: generators *are* important to establish the well-posedness of the physical problem.

How to check if C is the generator of a semigroup? That is, how can we know if, given a linear operator C , does exist a semigroup whose generator is exactly C ? The following definition Showalter (1994) is basilar for the next theorem.

Definition C.10. The operator $C \in L(\mathcal{D}(C), \mathcal{H})$ is said to be *accretive* if

$$\operatorname{Re}(Cx|x) \leq 0, \quad x \in \mathcal{D}(C). \quad (\text{C.2.8})$$

This definition is linked to the concept of contraction semigroups: please note that, if u is a solution for equation (C.1.1a) on page 114 and C is

²It is not only a semigroup, but also a group. The Schrödinger equation allows time-reversal operations, unlike the heat diffusion equation, thanks to its complex coefficients.

accretive, then

$$\begin{aligned} \frac{d}{dt} \|u(t)\|^2 &= 2 \operatorname{Re}(u'(t)|u(t)) = \\ &= 2 \operatorname{Re}(Cu(t)|u(t)) \leq 0, \quad t > 0, \end{aligned} \tag{C.2.9}$$

and thus $\|u(t)\|^2$ is a decreasing function, with $u(t) = S(t)u_0$. Then,

$$\|u(t)\| \leq \|u_0\|, \quad u_0 \in \mathcal{D}(C), t \geq 0. \tag{C.2.10}$$

In other words, $\|S(t)u_0\| \leq \|u_0\|$, which is the same condition we introduced in definition C.4 on page 116. This explains why accretive operators are useful when dealing with contraction semigroups.

Theorem C.11. *An operator $C \in L(\mathcal{D}(C), \mathcal{H})$ is the generator of a contraction semigroup on \mathcal{H} if and only if $\mathcal{D}(C)$ is dense in \mathcal{H} , C is accretive and $\lambda - C$ is surjective for some $\lambda > 0$.*

§ C.3 Well-posed Problems

C.3.1. The Definition. We need to define what we mean with “well-posed problem”. We follow the definition given in Richtmyer (1978).

Definition C.12. An initial-value problem is called *well posed* (in the sense of Hadamard) if it has the following properties:

1. The strict solutions are uniquely determined by their initial elements;
2. The set \mathcal{S} of all initial elements of strict solutions is dense in the Banach space \mathcal{B} .
3. For any finite interval $[0, t_0]$ there is a constant $K = K(t_0)$ such that every strict solution satisfies the inequality

$$\|u(t)\| \leq K \|u(0)\|, \quad \text{for } 0 \leq t \leq t_0. \tag{C.3.1}$$

The second point requires that even if a function $u(t) \in \mathcal{B}$ is not a valid initial condition, there must be a sequence $\{\tilde{u}_i\}_{i=1}^{\infty} \subset \mathcal{S}$ that converges to $u(t)$. Note that, since $u(0) \in \mathcal{D}(C)$ and $u(0) \in \mathcal{S}$, it follows that $\mathcal{S} \subseteq \mathcal{D}(C)$.

The third point has a simple physical interpretation: if there is a small error in the initial condition $u(0)$, the error in $u(t)$ must be constrained (through K). In other words, the solution has to be stable under variations of the initial condition.

C.3.2. Well-posedness of the Heat Equation. In this paragraph we prove that the diffusion problem leads to a well-posed problem. From equation (3.3.3a) on page 39, the diffusion operator can be written as

$$\begin{aligned} \mathcal{D}(A) &= \{u \in \mathcal{L}^2 : u, u' \in \mathcal{C}_{\text{abs}}, u'' \in \mathcal{L}^2, u_x(0) = u(L) = 0\}, \\ Au &= \frac{1}{D}u''. \end{aligned} \quad (\text{C.3.2})$$

Theorem C.13. *A is symmetric.*

Proof. If $u, v \in \mathcal{D}(A)$, then u and v are absolutely continuous functions: we can integrate $(Au|v)$ by parts. By noting that $[u'v]_0^L = [uv']_0^L = 0$ we have

$$\begin{aligned} (Au|v) &= \frac{1}{D} \int_0^L u'' v = \\ &= -\frac{1}{D} \int_0^L u' v' = \\ &= \frac{1}{D} \int_0^L u v'' = \\ &= (u|Av). \end{aligned} \quad \square$$

Corollary C.14. *A is essentially self-adjoint, and thus it is essentially closed.*

Proof. This is because A is symmetric and $\mathcal{R}(A \pm iI)$ is dense in $\mathcal{L}^2([0, L])$ (see Kirillov and Gvishiani (1982) for a proof of this last statement). \square

If A is essentially closed, there exist some linear operator \tilde{A} that is closed and such that $\tilde{A} > A$. The closeness of \tilde{A} is extremely important, since this lets us to exchange \tilde{A} with a limit or a series:

$$\tilde{A} \left(\lim_{n \rightarrow \infty} u_n \right) = \lim_{n \rightarrow \infty} \tilde{A}(u_n), \quad \tilde{A} \left(\sum_{n=0}^{\infty} u_n \right) = \sum_{n=0}^{\infty} \tilde{A}(u_n), \quad (\text{C.3.3})$$

if every limit and series used in the formulae do exist. Obviously \tilde{A} is unknown, but when evaluating $\tilde{A}u$ we can use the fact that $\tilde{A}u = Au$ if $u \in \mathcal{D}(A) \subset \mathcal{D}(\tilde{A})$. In order to use this trick, we shall use only functions that are in $\mathcal{D}(A)$: this is not difficult, since $\mathcal{D}(A)$ is a quite large set.

Theorem C.15. *A is accretive.*

Proof. If we take $u \in \mathcal{D}(A)$, we can evaluate $(Au|u)$ by integrating by parts, since u is absolutely continuous:

$$\begin{aligned} (Au|u) &= \frac{1}{D} \int_{[0,L]} u'' \bar{u} = \\ &= \frac{1}{D} \left([u' \bar{u}]_0^L - \int_{[0,L]} |u'|^2 \right) = \\ &= -\frac{1}{D} \|u'\|^2 \leq 0, \quad u \in \mathcal{D}(A) \end{aligned} \quad (\text{C.3.4})$$

(note that $[u'u]_0^L = 0$ because of boundary conditions). This shows that $(Au|u) \leq 0$. \square

This theorem has a physical interpretation. If A is accretive and $u(t)$ is a solution for the heat conduction equation, then $\|u(t)\|$ is a decreasing function, as we saw above. In fact, the steady-state solution of the heat equation is exactly $u = 0$ (remember the boundary conditions). This theorem explains why a generic solution $u(t)$ of our heat equation will go down to zero³

Theorem C.16. *If A is given by equation (C.3.2) on the page before, then equation (C.1.1a) on page 114 is well-posed.*

Proof. We prove this theorem by using definition C.12 on page 118:

1. From equation (C.11) on page 118 we can prove that A is the generator of some semigroup. It's obvious that the first two conditions about A are met. About $\lambda - A$ being surjective, we can note that if we let $\lambda = 1$ this assertion reduces to prove that

$$\frac{d}{dt}u(t) = Au + f(t), \quad (\text{C.3.5})$$

has at least one solution. But we found one solution in appendix B on page 111 using Green's functions. Then, from theorem C.9 on page 117 we know there exists exactly one solution for equation (C.1.1a) on page 114

2. $\mathcal{D}(A)$ is dense in $\mathcal{L}^2([0, L])$, since it contains the set defined in equation (A.2) on page 108, which is a basis for $\mathcal{L}^2([0, L])$. Thus, the second point in the definition is satisfied.
3. Since A is accretive, the third point in the definition is automatically satisfied (recall our discussion about the meaning of definition C.10 on page 117).

Thus, our problem is well-posed since it satisfies definition C.12. \square

§ C.4 Boundary Conditions

C.4.1. Exponential Operators. At this time, we know equation (C.1.1a) on page 114 is well-posed, but we do not know how to solve it. We anticipated the important role played by exponential operators; in this paragraph we prove some theorems about them. The following definition is taken from Richtmyer (1978).

³Our considerations do not prove this fact in a completely correct way. In fact, we proved that $\|u(t)\|$ is a monotonically decreasing function, but this does not mean that its limit is zero: only that a limit does exist. Other facts about A must be taken in account, but we prefer not to spend too much time about this issue.

Definition C.17. Let $C \in L(\mathcal{D}(C), \mathcal{H})$ be a bounded linear operator. The exponential operator $\exp(C)$ is defined in the following way:

$$\mathcal{D}(\exp(C)) = \left\{ u \in \mathcal{D}(C) : C^k u \in \mathcal{D}(C) \forall k \in \mathbb{N} \right\} \quad (\text{C.4.1a})$$

$$\exp(C) = \sum_{k=0}^{\infty} \frac{1}{k!} C^k \quad (\text{C.4.1b})$$

Theorem C.18. If C is a bounded operator, then the evolution operator for equation (C.1.1a) on page 114 is exactly $\exp(tC)$. That is, the solution $u(t)$ is given by

$$u(t) = \exp(tC)u_0 \quad (\text{C.4.2})$$

This would be a very useful theorem for heat conduction problems, but A is not bounded! We can try to use a smaller set for $\mathcal{D}(\exp(C))$:

Definition C.19. Let $C \in L(\mathcal{D}(C), \mathcal{H})$ be a linear operator. The exponential operator $\exp(C)$ is defined in the following way:

$$\mathcal{D}(\exp(C)) = \left\{ u \in \mathcal{D}(C) : \forall k \in \mathbb{N}, C^k u \in \mathcal{D}(C), \right. \\ \left. \sum_{k=0}^{\infty} \frac{1}{k!} C^k u \text{ converges in } \mathcal{H} \right\} \quad (\text{C.4.3a})$$

$$\exp(C) = \sum_{k=0}^{\infty} \frac{1}{k!} C^k \quad (\text{C.4.3b})$$

As Richtmyer (1978) proves, considering $\exp(tC)$ when C is not bounded gives only a restriction for the evolution operator $S(t)$. In mathematical notation, this means that $\exp(tC) \leq S(t)$.

This is not as bad as you could think, because if $u_0 \in \mathcal{D}(\exp(tC))$ then we know the solution for equation (C.1.1a) on page 114 is $\exp(tC)u_0$, even if C is not bounded. So, we must determine when does it happens that $u_0 \in \mathcal{D}(\exp(tC))$, and how can we calculate $\exp(tC)u_0$.

The answer to these questions gives the (semi-) definitive solution to our problems, thanks to the whole set of theorems cited till now. Just follow the reasoning: if we have some criterion to say that $u_0 \in \mathcal{D}(\exp(tC))$, then we know that $u_0 \in \mathcal{D}(S(t))$, and from this follows that

$$u(t) = \exp(tC)u_0 \quad (\text{C.4.4})$$

gives a strict solution for equation (C.1.1a) on page 114. This is an important result, since if $u(t)$ is a strict solution, then it takes care of the boundary conditions and of the initial condition as well, and this is exactly what we wanted. In the next paragraphs we shall give an answer to these question.

Theorem C.20. Let C be a linear operator in $L(\mathcal{D}(C), \mathcal{H})$. If u is an eigenfunction for C such that

$$Cu = \lambda u, \quad (\text{C.4.5})$$

with $\lambda \in \mathbb{C}$, then $u \in \mathcal{D}(\exp(tC))$ for all $t > 0$ and u is an eigenfunction for $\exp(tC)$ with eigenvalue equal to $\exp(t\lambda)$:

$$\exp(tC)u = \exp(t\lambda)u \quad (\text{C.4.6})$$

Proof. Let's apply the definition for $\exp(tC)$:

$$\begin{aligned} \exp(tC)u &= \sum_{k=0}^{\infty} \frac{1}{k!} (tC)^k u = \\ &= \sum_{k=0}^{\infty} \frac{(t\lambda)^k}{k!} u = \\ &= \exp(t\lambda)u. \quad \square \end{aligned}$$

Theorem C.21. Let C be a linear operator in $L(\mathcal{D}(C), \mathcal{H})$, and $\{e_n\}_{n=0}^{\infty}$ an orthonormal basis for the closure of $\mathcal{D}(C)$ such that for any n

$$Ce_n = \lambda_n e_n. \quad (\text{C.4.7})$$

Then $u \in \mathcal{D}(\exp(tC))$ if and only if

$$\sum_{n=0}^{\infty} |(u|e_n) \exp(t\lambda_n)|^2 \text{ converges.} \quad (\text{C.4.8})$$

Proof, \Rightarrow side. If $u \in \mathcal{D}(\exp(tC))$ then the following series converges to some $v \in \mathcal{H}$:

$$v = \sum_{k=0}^{\infty} \frac{1}{k!} (tC)^k u. \quad (\text{C.4.9})$$

Since $\{e_n\}_{n=0}^{\infty}$ is a basis for the closure of $\mathcal{D}(C)$, then

$$u = \sum_{n=0}^{\infty} (u|e_n) e_n. \quad (\text{C.4.10})$$

By substituting this expression in the series, we get

$$\begin{aligned} v &= \sum_{k=0}^{\infty} \sum_{n=0}^{\infty} \frac{(u|e_n)}{k!} C^k e_n = \\ &= \sum_{k=0}^{\infty} \sum_{n=0}^{\infty} \frac{(u|e_n) (t\lambda_n)^k}{k!} e_n = \\ &= \sum_{n=0}^{\infty} (u|e_n) \exp(t\lambda_n) e_n. \end{aligned} \quad (\text{C.4.11})$$

But the Fischer-Rietz theorem states the last series above converges if and only if

$$\sum_{n=0}^{\infty} |(u|e_n) \exp(t\lambda_n)|^2 \quad (\text{C.4.12})$$

converges, since $\{e_n\}$ is an orthonormal set. \square

Proof, \Leftarrow side. The proof is evident if you trace the \Rightarrow side proof bottom-up, since the Fisher-Rietz theorem is valid both in the \Leftarrow and in the \Rightarrow side. \square

C.4.2. The Diffusion Operator. We can choose to use the orthonormal basis from equation (A.2) on page 108, since it is a basis contained in $\mathcal{D}(A)$ and it is made by eigenfunctions of A : it is simple to show that

$$Ae_n = \lambda_n e_n \quad \text{with} \quad \lambda_n = -\left(n + \frac{1}{2}\right)^2 \frac{\pi^2}{a^2}. \quad (\text{C.4.13})$$

The following theorem is probably one of the most important ones in this chapter. It is a simple corollary of the previous theorems, and summarize what we said in the previous sections.

Theorem C.22. *Let C be a closed operator, $\{e_n\}_{n=0}^{\infty}$ be a orthonormal basis for \mathcal{H} made by eigenfunctions of C , and let the set $\{\lambda_n\}_{n=0}^{\infty}$ of eigenvalues being such that $\lambda_n \rightarrow -\infty$ if $n \rightarrow \infty$. Given a function $u_0 \in \mathcal{D}(\exp(tC))$ for $t > 0$ such that the series*

$$u_0 = \sum_{n=0}^{\infty} (u_0|e_n) e_n \quad (\text{C.4.14})$$

converges uniformly, then $u(t) = \exp(tC)u_0$ is given by the following series

$$u(t) = \sum_{n=0}^{\infty} \exp(t\lambda_n) (u_0|e_n) e_n \quad (\text{C.4.15})$$

which converges uniformly for any $t > 0$.

§ C.5 The Inhomogeneous Case

The last theorem in the previous section is a very important result, but it does not consider the presence of inhomogeneous terms in the Cauchy problem. Our work is to find solutions for equation (3.3.3a) on page 39, which contains the inhomogeneous term $r(x, t)$. We chose to ignore this term since it is quite simple to generalize our previous conclusions to the case of equation (3.3.3a) on page 39. Thus, we shall not provide the details of this generalization.

When considering the following equation:

$$\frac{d}{dt}u(t) = C u(t) + f(t) \quad (\text{C.5.1a})$$

$$u(0) = u_0 \quad (\text{C.5.1b})$$

for some $f \in \mathcal{H}$, we could try the following solution:

$$u(t) = \exp(tC) u_0 + \int_0^t \exp((t - \tau)C) f(\tau) d\tau, \quad (\text{C.5.2})$$

which we obtained with some symbolical manipulations. You can note how the $\exp(tC)$ and the $\exp((t - \tau)C)$ have the same form of the evolution operators we studied in the homogeneous case (remember that $\tau \in [0, t]$, so $t - \tau \geq 0$); we could write the solution in this way as well, showing the link with the homogeneous solution:

$$u(t) = S(t) u_0 + \int_0^t S(t - \tau) f(\tau) d\tau. \quad (\text{C.5.3})$$

The only detail to add is to study the $S(t - \tau)$ operator, and when does the integral exist; we choose not to show this here.

After having studied when our proposed solution is defined, it suffices to remember that theorem C.9 on page 117 can be used to characterize inhomogeneous problems exactly like we did with homogeneous problems. Thus, searching a strict solution⁴) for the inhomogeneous problem is conceptually similar to the homogeneous case.

⁴The meaning of “strict solution” in this context is almost the same as definition C.2 on page 115, provided we take care of the inhomogeneous term in the definition.

APPENDIX D

Scripts used with the Heat Program

In this appendix we will show a concrete use of `heat`¹ for studying a one-dimensional problem. The script reported here was used to generate the discrete points shown in figure figure 5.23 on page 85.

To use `heat`, the user must supply a text file containing a description of the physical problem to be solved. File `heat-fluct.heat` simulate the propagation of a sinusoidal oscillation of the radiative heat flux coming from the LFI antenna through the RL:

```
# File: heat-fluct.heat

# This is the period of the fluctuation (in seconds)
period = 60;

# This is the ending time (in seconds). It is eight
# times the fluctuation period.
end_time = 8 period;

# Heat conductivity (W/K/cm)
conductivity = 8.0e-4;

# Diffusivity constant (cm^2/s)
diffusivity = 0.049;

# Length of the rod (cm)
mass_length = 1.0;

# Time step used for integrating the diffusion equation
delta_time = period / 60.0;

# Time step to output the grid. It is three times delta_time
output_delta_time = 3 delta_time;

# Number of grid points
```

¹The program is freely available at http://www.geocities.com/zio_tom78/heat/.

```

grid_points = 50;

# Amplitude of the fluctuation at LFI side (W/cm^2)
fluct_amplitude = 0.001;

# This is the initial temperature (K)
initial_condition = 4.0;

# These are the plot limits (used only when generating a plot)
min_plot_temperature = 3.8;
max_plot_temperature = 4.2;

# This is the heat power provided by the radiometer (W/cm^2)
heat_source := fluct_amplitude Sin[2 Pi time / period];

# This is the HFI temperature (K)
boundary_temperature = 4;

```

The text file is made by comments (beginning with #) and variable definitions. Some of them are pre-defined variables (like `initial_condition`), but the user can define and use other variable names (like `period`, used to define `heat_source`). Please note the use of `:=` instead of `=` for defining a *dynamic variable* (like `heat_source`) whose value is not constant but depends on time or position. The program outputs a set of temperature samples for each time interval, going from `start_time` to `end_time` in steps of `delta_time`. Many output formats are implemented by means of GNU Libplot.

By using GNU Guile it is possible to create new output formats and even doing interactive data processing by writing Scheme scripts. The following program, `fluct-ampl.scm`, was used to interpolate the temperature samples and extract the fluctuation amplitude to be used in figure 5.23 on page 85:

```

; Scheme code to use with Heat 0.1.
; Copyright (c) 2002 Maurizio Tomasi
;
; Call heat with the following command line:
;
;   heat -s fluct-amplitude.scm [YOUR PARAMETERS HERE]
;
; This scheme code will analyze the first grid element supposing that
; its temperature fluctuates with a sinusoidal law. It discards the
; first half of the data, and calculates the amplitude of the
; fluctuation by using the remaining samples. The value of 1/PERIOD
; and the amplitude are written on stdout when the simulation ends.

(define half
  ;;; Return the number / 2. If number is odd, round it to the next
  ;;; lower integer.
  (lambda (n)
    (/ (if (odd? n) (- n 1) n) 2)))

```

```

(define tenth
  ;;; Return the number / 10. The result is rounded.
  (lambda (n)
    (inexact->exact (/ n 10))))

(define remove-first-half
  ;;; Return L without the first half of the list.
  (lambda (l)
    (list-tail l (half (length l)))))

(define remove-almost-all
  ;;; Return L without the first 9/10 of the list.
  (lambda (l)
    (let ((len (length l)))
      (list-tail l (- len (tenth len))))))

(define fluct-amplitude
  ;;; Calculate the amplitude of the fluctuation
  (lambda (l)
    (let ((half-list (remove-almost-all l)))
      (/ (- (apply max half-list) (apply min half-list)) 2))))

(define callback
  ;;; Called after having computed the new node temperatures
  (lambda () (set! temp-list
    (append temp-list
      (cons (get-grid-point-temperature 0) '())))))

(define end-callback
  ;;; Called when the simulation ends
  (lambda () (begin
    (display (/ 1.0 (get-var-value "period")))
    (display " ")
    (display (fluct-amplitude temp-list))
    (newline))))

(set-start-callback! start-callback)
(set-callback! callback)
(set-end-callback! end-callback)

(define max-amplitude #f)
(define temp-list '())

```

The purpose of this small program is to extract the maximum and minimum temperature (assuming that the temperature of each node fluctuates as a sinusoid), and then evaluate the halved difference between these values:

$$\Delta T = \frac{T_{\max} - T_{\min}}{2}. \quad (\text{D.1})$$

This is an approximation for the amplitude of the fluctuation. The program throws away the first half of the dataset in order not to consider transient effects.

If you understand the Scheme language, you can note how there are some functions used in this program (like `get-var-value`) that are not part of the standard Scheme Language. While GNU Guile interpret the standard Scheme code, `heat` is responsible for interpreting these extensions.

The Scheme program reported above is a “filter” which can be used with any physical problem that involves a fluctuation in the temperature. So, to apply the program to our `heat-fluct.heat` file we could execute

```
% heat -f null -s fluct-ampl.scm heat-fluct.heat
0.0166666666666667 0.768224946393095
```

The `-f null` option avoids the creation of an output file by `heat`, since `fluct-amplitude.scm` already outputs to the terminal the data we are looking for. The result is written as a frequency-amplitude pair, where the frequency is in Hertz and is simply $1/\text{period}$, and the amplitude is a pure number going from 0 to 1.

A similar program was used to evaluate the phase delay between the fluctuation at $x = a$ and at $x = 0$:

```
;;; Scheme code to use with Heat 0.1.
;;; Copyright (c) 2002 Maurizio Tomasi
;;;
;;; Call heat with the following command line:
;;;
;;;   heat -s fluct-phase.scm [YOUR PARAMETERS HERE]
;;;
;;; This scheme code will analyze the first grid element supposing
;;; that its temperature fluctuates with a sinusoidal law. It finds
;;; the first relative maximum and writes the time related to this
;;; sample to stdout.

(define half
  ;; Return the number / 2. If number is odd, round it to the next
  ;; lower integer.
  (lambda (n)
    (/ (if (odd? n) (- n 1) n) 2)))

(define remove-first-half
  ;; Return L without the first half of the list.
  (lambda (l)
    (list-tail l (half (length l)))))

(define is-x3-a-maximum
  ;; Return #t if y3 is a local maximum
  (lambda (y1 y2 y3 y4 y5)
    (and (>= y2 y1) (>= y3 y2) (<= y4 y3) (<= y5 y4)
         (or (> y2 y1) (> y3 y2) (> y4 y3) (> y5 y4)))))

(define get-maximum-pos
  ;; Evaluate the maximum of the parabola passing through
  ;; the points (-1, y1), (0, y2), (1, y3) and return the
  ;; abscissa of the maximum (always between -1 and 1).
```

```

(lambda (y1 y2 y3)
  (* 0.5 (/ (- y1 y3) (+ y1 (* -2 y2) y3))))))

(define fluct-phase
  ;; Calculate the phase shift of the fluctuation. Return the
  ;; position of the first local maximum (starting from 1), calculated
  ;; by means of a quadratic interpolation. If no maximum was found
  ;; or if the list has got less than five elements, return #f.
  ;; Examples:
  ;;
  ;; (fluct-phase '(1 2 3 4 5 4 3 2 1))
  ;; => 5.0
  ;; (fluct-phase '(1 2 3 4 5))
  ;; => #f
  ;; (fluct-phase '())
  ;; => #f
  (lambda (l)
    (let ((cur-pos 2))
      (letrec ((recurse-list
                (lambda (sublist)
                  (begin (set! cur-pos (+ cur-pos 1))
                        (if (< (length sublist) 5)
                            #f
                            (if (is-x3-a-maximum (car sublist)
                                                  (cadr sublist)
                                                  (caddr sublist)
                                                  (caddrdr sublist))
                                (car (cddddr sublist))
                                (+ cur-pos
                                   (get-maximum-pos (cadr sublist)
                                                  (caddr sublist)
                                                  (caddrdr sublist))
                                   (recurse-list (cdr sublist))))))))
                    (if (list? l)
                        (recurse-list l)
                        #f))))))

(define callback
  ;; Called after having computed the new node temperatures
  (lambda () (set! temp-list
                  (append temp-list
                          (cons (get-grid-point-temperature 0)
                                '())))))

(define end-callback
  ;; Called when the simulation ends
  (lambda ()
    (let* ((delta-time (get-var-value "delta_time"))
           (start-time (* (get-var-value "period") 1.25))
           (l (list-tail temp-list
                        (inexact->exact (/ start-time delta-time))))
           (display (/ 1.0 (get-var-value "period")))
           (display " "))
      ))

```

```
(display (* (get-var-value "delta_time")
(- (fluct-phase 1) 1)))
(newline)))

(set-callback! callback)
(set-end-callback! end-callback)

(define temp-list '())
```

The program finds a local maximum discarding the first period of the dataset, then it fits the curve with a parabola $y = at^2 + bt + c$ and returns the maximum t_{\max} of this parabola (having discarded the first period, this would be the second relative maximum in the dataset). Supposing that the temperature at $x = a$ fluctuates with a law $\sin(2\pi\nu t)$, then $t_{\max} - 1/\nu$ is the time of the first maximum.

APPENDIX E

Numerical Meshes with FElt

To test the 2-D numerical models we used FElt 3.05 (Gobat and Atkinson 1997), a Finite Analysis computer system which can simulate thermal diffusion in one and two dimensions. It's a free program which runs under UNIX systems and Windows; it can be found on the World Wide Web at <http://felt.sourceforge.net/>.

In this appendix we shall show how to use FElt to derive some results we got in this work.

§ E.1 The 2-D Model

We report here a simplified version of the 2-D model we used in section 5.1.2 on page 62. The model provided here uses only 42 nodes, and FElt shows significant numerical errors with this little number. To obtain the results shown in figure 5.11 on page 74, we used a model with 180 nodes.

```
problem description
title="Sudden temperature change (2-D model)"
nodes=42 elements=60 analysis=transient-thermal

/* We study thermal behaviour for t = 0 s ... 20 s
 * with steps of 0.05 seconds. */
analysis parameters
start=0 stop=20 step=0.05

/* 'alpha = 0.5' uses a Crank-Nicolson implicit scheme for integrating
 * the time-dependent heat equation. */
beta=0 gamma=0 alpha=0.5
mass-mode=lumped

/* These nodes are the most interesting:
 * . Node #12 is placed at (x = 0, y = -b/2), one of the four corners
 *   in the Eccosorb plane (the nearest to the LFI radiometer)
 * . Node #18 is placed at (x = 0, y = -b/4)
 * . Node #24 is placed at (x = 0, y = 0)
 * The 'nodes' directive dumps the temperature of these three nodes
```

```

* on stdout.
* */
nodes=[12, 18, 24]
dofs=[Tx]

nodes
1 x=0 y=-0.8 z=0 constraint=cons
2 x=0.2 y=-0.8 z=0 constraint=free
3 x=0.4 y=-0.8 z=0
4 x=0.6 y=-0.8 z=0
5 x=0.8 y=-0.8 z=0
6 x=1 y=-0.8 z=0
7 x=0 y=-0.7 z=0 constraint=cons
8 x=0.2 y=-0.7 z=0 constraint=free
9 x=0.4 y=-0.7 z=0
10 x=0.6 y=-0.7 z=0
11 x=0.8 y=-0.7 z=0
12 x=1 y=-0.7 z=0
13 x=0 y=-0.35 z=0 constraint=cons
14 x=0.2 y=-0.35 z=0 constraint=free
15 x=0.4 y=-0.35 z=0
16 x=0.6 y=-0.35 z=0
17 x=0.8 y=-0.35 z=0
18 x=1 y=-0.35 z=0
19 x=0 y=0 z=0 constraint=cons
20 x=0.2 y=0 z=0 constraint=free
21 x=0.4 y=0 z=0
22 x=0.6 y=0 z=0
23 x=0.8 y=0 z=0
24 x=1 y=0 z=0
25 x=0 y=0.35 z=0 constraint=cons
26 x=0.2 y=0.35 z=0 constraint=free
27 x=0.4 y=0.35 z=0
28 x=0.6 y=0.35 z=0
29 x=0.8 y=0.35 z=0
30 x=1 y=0.35 z=0
31 x=0 y=0.7 z=0 constraint=cons
32 x=0.2 y=0.7 z=0 constraint=free
33 x=0.4 y=0.7 z=0
34 x=0.6 y=0.7 z=0
35 x=0.8 y=0.7 z=0
36 x=1 y=0.7 z=0
37 x=0 y=0.8 z=0 constraint=cons
38 x=0.2 y=0.8 z=0 constraint=free
39 x=0.4 y=0.8 z=0
40 x=0.6 y=0.8 z=0
41 x=0.8 y=0.8 z=0
42 x=1 y=0.8 z=0

ctg elements
1 nodes=[7,1,2] material=aluminium 2 nodes=[8,2,3]
3 nodes=[9,3,4] 4 nodes=[10,4,5]
5 nodes=[11,5,6] 6 nodes=[7,2,8]
7 nodes=[8,3,9] 8 nodes=[9,4,10]

```

```
9 nodes=[10,5,11] 10 nodes=[11,6,12]
11 nodes=[13,7,8] material=eccosorb 12 nodes=[14,8,9]
13 nodes=[15,9,10] 14 nodes=[16,10,11]
15 nodes=[17,11,12] 16 nodes=[13,8,14]
17 nodes=[14,9,15] 18 nodes=[15,10,16]
19 nodes=[16,11,17] 20 nodes=[17,12,18]
21 nodes=[19,13,14] 22 nodes=[20,14,15]
23 nodes=[21,15,16] 24 nodes=[22,16,17]
25 nodes=[23,17,18] 26 nodes=[19,14,20]
27 nodes=[20,15,21] 28 nodes=[21,16,22]
29 nodes=[22,17,23] 30 nodes=[23,18,24]
31 nodes=[25,19,20] 32 nodes=[26,20,21]
33 nodes=[27,21,22] 34 nodes=[28,22,23]
35 nodes=[29,23,24] 36 nodes=[25,20,26]
37 nodes=[26,21,27] 38 nodes=[27,22,28]
39 nodes=[28,23,29] 40 nodes=[29,24,30]
41 nodes=[31,25,26] 42 nodes=[32,26,27]
43 nodes=[33,27,28] 44 nodes=[34,28,29]
45 nodes=[35,29,30] 46 nodes=[31,26,32]
47 nodes=[32,27,33] 48 nodes=[33,28,34]
49 nodes=[34,29,35] 50 nodes=[35,30,36]
51 nodes=[37,31,32] material=aluminium 52 nodes=[38,32,33]
53 nodes=[39,33,34] 54 nodes=[40,34,35]
55 nodes=[41,35,36] 56 nodes=[37,32,38]
57 nodes=[38,33,39] 58 nodes=[39,34,40]
59 nodes=[40,35,41] 60 nodes=[41,36,42]
```

```
/* Properties of the materials. */
material properties
aluminium t=1.414 rho=2.71 Kx=0.12 Ky=0.12 C=0.000388
eccosorb t=1.414 rho=1.7 Kx=0.0008 Ky=0.0008 C=0.0096
```

```
constraints
cons Tx=4.5 Ty=u Tz=u Rx=u Ry=u Rz=u ITx=4
free Tx=u Ty=u Tz=u Rx=u Ry=u Rz=u ITx=4
```

```
end
```

Mathematical Symbols

$(v w)$	Inner product between v and w .
$\ v\ $	Norm of $v \in \mathcal{H}$.
A	The diffusion operator ($D \nabla^2$).
c	Specific heat of a solid. [c] = erg/K/g
C	Linear operator.
\mathbb{C}	Field of complex numbers.
$\mathcal{C}(X)$	Set of continuous functions $f : X \rightarrow \mathbb{C} (\mathbb{R})$.
$\mathcal{C}_{\text{abs}}(X)$	Set of absolutely continuous functions $f : X \rightarrow \mathbb{C} (\mathbb{R})$.
$\mathcal{C}^n(X)$	Subset of $\mathcal{C}(X)$ containing functions derivable up to n times over X whose n -th derivative is continuous on X .
$\mathcal{C}^\infty(X)$	Set of infinitely-derivable functions $f : X \rightarrow \mathbb{C} (\mathbb{R})$.
D	Thermal diffusivity of a solid. [D] = cm ² /s
$\mathcal{D}(C)$	Domain of linear operator C .
\mathcal{H}	Hilbert space.
\mathcal{I}	Set of all possible initial conditions in a PDE.
k	Thermal conductivity of a solid. [k] = erg/s/cm/K
$L(\mathcal{H}_1, \mathcal{H}_2)$	Set of linear operators of the form $C : \mathcal{H}_1 \rightarrow \mathcal{H}_2$.
$\mathcal{L}^n(\mathcal{H})$	Banach space of functions $f : \mathcal{H} \rightarrow \mathbb{C}$ such that $ f ^n$ is summable.
\mathbb{R}	Field of real numbers.
\mathbb{R}^\pm	Set of positive/negative real numbers, including zero.
\mathbb{R}_0^\pm	Set of positive/negative real numbers, excluding zero.
ρ	Mass density. [ρ] = g/cm ³
$\mathcal{R}(C)$	Range of linear operator C .
T	Temperature. [T] = K
$V \{e_n\}$	The Hilbert space generated by $\{e_n\}$.

Acronyms used in the text

CMB Cosmic Microwave Background

COBE Cosmic Background Explorer

DFT Discrete Fourier Transform

EE Eigenfunction Expansion

ESA European Space Agency

HEMT High Electron Mobility Transistor

HFI High Frequency Instrument

JPL Jet Propulsion Laboratories

LFI Low Frequency Instrument

MAP Microwave Anisotropy Probe

NASA National Aeronautics and Space Administration

OMT OrthoMode Transducer

PDE Partial Differential Equation

RL Reference Load

SC Sorption Cooler

Bibliography

- Maria Cristina Abbati and Renzo Cirelli. *Metodi matematici per la fisica: operatori lineari negli spazi di Hilbert*. Città Studi Edizioni, 1997.
- C. L. Bennett, A. J. Banday, K. M. Górski, G. Hinshaw, P. Jackson, P. Keegstra, A. Kogut, G. F. Smoot, D. T. Wilkinson, and E. L. Wright. Four-year COBE DMR cosmic microwave background observations: Maps and basic results. *Astrophysical Journal*, 464:L1–L4, June 1996.
- M. Bersanelli, M. Bensadoun, G. de Amici, S. Levin, M. Limon, G. F. Smoot, and W. Vinje. Absolute measurement of the cosmic microwave background at 2 GHz. *The Astrophysical Journal*, 424:517–529, April 1994. URL http://adsabs.harvard.edu/cgi-bin/nph-bib_query?bibcode=1994ApJ...424..517B&db_key=AST.
- Marco Bersanelli, Davide Maino, and Aniello Mennella. Anisotropies in the cosmic microwave background. To appear in “Il Nuovo Cimento”, 2002.
- T. W. Bradshaw. 4 K cooler block diagram. Technical report, Rutherford Appleton Laboratory, aug 1999. TD-PHDB0-990804-RAL.
- Martin A. Bucher and David N. Spergel. Inflation in a low-density universe. *Scientific American*, 280:62–69, January 1999.
- P. de Bernardis, P. A. R. Ade, R. Artusa, J. J. Bock, A. Boscaleri, B. P. Crill, G. De Troia, P. C. Farese, M. Giacometti, V. V. Hristov, A. Iacoangeli, A. E. Lange, A. T. Lee, S. Masi, L. Martinis, P. V. Mason, P. D. Mauskopf, F. Melchiorri, L. Miglio, T. Montroy, C. B. Netterfield, E. Pascale, F. Piacentini, P. L. Richards, J. E. Ruhl, and F. Scaramuzzi. Mapping the CMB sky: The BOOMERanG experiment. *New Astronomy Review*, 43:289–296, July 1999. URL http://adsabs.harvard.edu/cgi-bin/nph-bib_query?bibcode=1999NewAR...43..289D&db_key=AST.
- D. J. Fixsen, E. S. Cheng, J. M. Gales, J. C. Mather, R. A. Shafer, and E. L. Wright. The cosmic microwave background spectrum from the full COBE FIRAS data set. *Astrophysical Journal*, 473:576, December 1996.

- URL http://adsabs.harvard.edu/cgi-bin/nph-bib_query?bibcode=1996ApJ...473..576F&db_key=AST.
- George Gamow. Expanding universe and the origin of elements. *Physical Review*, 70:572–573, October 1946.
- Jason I. Gobat and Darren C. Atkinson. *The FELT System: User's Guide and Reference Manual*. University of California, San Diego, 1997. URL <http://felt.sourceforge.net/>. Version 3.02.
- Karl E. Gustafson. *Introduction to Partial Differential Equations and Hilbert Space Methods*. John Wiley and Sons, 1980.
- N. W. Halverson, W. L. Holzapfel, J. Kovac, E. M. Leitch, C. Pryke, and J. E. Carlstrom. Detection of polarization in the cosmic microwave background using DASI. *Astrophysical Journal*, 2002.
- Wayne Hu and Scott Dodelson. Cosmic microwave background anisotropies. *Annual Reviews of Astronomy and Astrophysics*, 2002. URL <http://background.uchicago.edu/~whu/araa/araa.html>.
- Wayne Hu, Naoshi Sugiyama, and Joseph Silk. The physics of microwave background anisotropies. *Nature*, 386(6):37–43, March 1997. URL http://adsabs.harvard.edu/cgi-bin/nph-bib_query?bibcode=1997Natur.386...37H&db_key=AST.
- Sadik Kakaç and Yaman Yener. *Heat Conduction*. Hemisphere Publishing Corporation, second edition, 1985.
- A.A. Kirillov and A.D. Gvishiani. *Theorems and Problems in Functional Analysis*. Springer-Verlag, 1982.
- D. Maino, C. Burigana, M. Maltoni, B. D. Wandelt, K. M. Górski, M. Malaspina, M. Bersanelli, N. Mandolesi, A. J. Banday, and E. Hivon. The Planck-LFI instrument: Analysis of the 1/f noise and implications for the scanning strategy. *Astronomy & Astrophysics Supplement*, 140:383–391, December 1999. URL http://cdsads.u-strasbg.fr/cgi-bin/nph-bib_query?bibcode=1999A%26AS..140..383M&db_key=AST.
- E. D. Marquardt, J. P. Le, and Ray Radebaugh. Cryogenic Material Properties Database. In "11th International Cryocooler Conference", jun 2002.
- Aniello Mennella, Marco Bersanelli, Carlo Burigana, Davide Maino, Nazzeno Mandolesi, Gianluca Morgante, and Giuseppe Stanghellini. Planck: Systematic effects induced by periodic fluctuations of arbitrary shape. *Astronomy & Astrophysics*, 384(2):736–742, March 2002.

- Aniello Mennella, Marco Bersanelli, Roberto Ferretti, Gianluca Morgante, Mauro Prina, Carlo Burigana, and Davide Maino. Effect of sorption cooler temperature variations on LFI front-end. Technical Note PL-LFI-PST-TN-005, IASF-CNR (ex. IFC), TESRE-CNR, UNIMI, LABEN, JPL, OAT, October 2001.
- Arno Penzias and Robert Woodrow Wilson. A measurement of excess antenna temperature at 4080 mc/s. *Astrophysical Journal*, 142:419–421, July 1965. URL http://adsabs.harvard.edu/cgi-bin/nph-bib_query?bibcode=1965ApJ...142..419P&db_key=AST.
- William H. Press, Brian P. Flannery, Saul A. Teukolsky, and William T. Vetterling. *Numerical Recipes in C: The Art of Scientific Computing*. Cambridge University Press, 1992. URL www.nr.com.
- Jeffrey Rauch. *Partial Differential Equations*, chapter 5.7. Springer-Verlag, 1991.
- R.D. Richtmyer. *Principles of Advanced Mathematical Physics*, volume 1. Springer-Verlag, 1978.
- Michael Rowan-Robinson. *Cosmology*. Clarendon Press, Oxford, third edition, 1996.
- Douglas Scott, Joseph Silk, and Martin White. From microwave anisotropies to cosmology. *Science*, 268(12):829–835, May 1995.
- Michael Seiffert, Aniello Mennella, Carlo Burigana, Nazzareno Mandolesi, Marco Bersanelli, Peter Meinhold, and Phil Lubin. $1/f$ noise and other systematic effects in the PLANCK LFI radiometers. *Astronomy & Astrophysics*, 391(3):1185–1197, September 2002.
- R. E. Showalter. *Hilbert Space Methods for Partial Differential Equations*, volume 1 of *Monographs*, chapter IV. Electronic Journal of Differential Equations, 1994. It can be found on the WWW at ejde.math.swt.edu/Monographs/01.
- G. F. Smoot, M. V. Gorenstein, and R. A. Muller. Detection of anisotropy in the cosmic blackbody radiation. *Physical Review Letters*, 39:898–901, October 1977. URL http://adsabs.harvard.edu/cgi-bin/nph-bib_query?bibcode=1977PhRvL..39..898S&db_key=AST.
- Karl Storck. *Heat Transfer in Glass Forming and Fluid Temperature-Control Systems*. PhD thesis, Applied Thermodynamics and Fluid Mechanics Department of Mechanical Engineering, Linköping University (Sweden), 1998. URL <http://www.mvs.ikp.liu.se/staff/karl/PhD.pdf>.

John C. Strikwerda. *Finite difference schemes and partial differential equations*. Wadsworth & Brooks/Cole Advanced Books & Software, 1989.

The COBE Homepage. WWW Page. URL http://space.gsfc.nasa.gov/astro/cobe/cobe_home.html.

The MAP Homepage. WWW Page. URL <http://map.gsfc.nasa.gov/>.

Luca Valenziano and Luca Terenzi. Analysis of the 4KRL fluctuation damping. IASF Technical Note (draft), June 2002.

Steven Weinberg. *The First Three Minutes. A Modern View of the Origin of the Universe*. Bantam Books, 1977.